國 立 交 通 大 學

光電工程研究所

博士論文

光通訊系統中的全光訊號處理

All-Optical Signal Processing in Optical
Communication Systems

研 究 生：魏 嘉 建

指 導 教 授：陳 智 弘 老師

中 華 民 國 九 十 七 年 十 一 月

光通訊系統中的全光訊號處理

All-Optical Signal Processing in Optical Communication Systems

研 究 生： 魏嘉建   Student : Chia-Chien Wei

指導教授： 陳智弘 老師   Advisor : Associate Prof. Jyehong Chen

國 立 交 通 大 學

光 電 工 程 研 究 所

博 士 論 文

A Disseration
Submitted to Institute of Electro-Optical Engineering
College of Electrical and Computer Engineering
National Chiao Tung University
In Partial Fulfillment of the Requirements
For the Degree of Philosophy
In
Institute of Electro-Optical Engineering
October 2008
Hsinchu, Taiwan, Republic of China

中 華 民 國 九 十 七 年 十 一 月

摘要

光通訊系統中的全光訊號處理

研究生： 魏嘉建　　　　　　　　　指導教授：　陳智弘 老師

本論文將介紹及分析數種新穎的全光訊號處理技術，包含了全光的波長轉換、全光的開關移鍵到差分相位移鍵的格式轉換、全光的差分相位移鍵的再生。

為了提升在半導體光放大器中的交叉極化調變之波長轉換頻寬，我們提出了一種稱作差分交叉極化調變的方法，它與傳統的交叉極化調變的不同僅在於一段額外的雙折射延遲線。在差分交叉極化調變的分析部份，包括訊號的數值模擬以及小訊號模型的推導，兩者都能和實驗結果互相對應。其中數值模擬清楚地顯示出波長轉換的效能提昇，而小訊號模型則提供了更多對差分交叉極化調變直觀且深入的理解。

在全光調變格轉換中，我們使用光子晶體光纖中的交叉相位調變，來達成 40 Gb/s 的開關移鍵到差分相位移鍵的訊號格式轉換。因為我們所使用的光子晶體光纖具有高度的線性雙折射特性，並且其雙折射光軸在整段光纖中是固定的，將受感應光的偏振態控制在相對雙折射光軸 45° 輸入光纖時，只要受感應光與調變光的波長差超過約 6 nm 就能明顯降低該全光調變格式轉換效率受調變光偏振態的影響程度，並且偏振態與波長差對於格式轉換的影響有理論的定量分析。由於該格式轉換基於以調變光光強度調變受感應光相位，當我們需要的相位變化不足、或調變光強度雜訊引起相位雜訊，都會影響差分

相位移鍵的訊號性能，該問題的造成的損耗也有理論的分析。

關於差分相位移鍵的訊號再生，因為差分相位移鍵訊號是將訊號載在光相位上，其訊號表現會同時受到振幅及相位雜訊影響。因此，除了振幅的再生，差分相位移鍵的再生必須要保留原有相位，甚至要降低相位雜訊。我們提出了一個新的概念：相位雜訊平均器，來降低差分相位移鍵的系統中的相位雜訊。它能夠有效地增加相鄰位元間相位雜訊的相關性，並因此減少了系統的差分相位雜訊。考慮各種不同特性的相位雜訊，我們發現多次的相位雜訊平均皆能使差分相位雜訊收斂，而且無關於系統傳輸長度。最後，對於不同的差分相位移鍵的再生，我們也理論分析了它們的差異。

ABSTRACT

Title of dissertation:	ALL-OPTICAL SIGNAL PROCESSING IN OPTICAL COMMUNICATION SYSTEMS
	Chia-Chien Wei, Doctor of Philosophy, 2008
Dissertation directed by:	Associate Professor Jason (Jyehong) Chen Department of Photonics National Chiao Tung University, Taiwan

In this dissertation, new approaches for all-optical wavelength conversion, all-optical on-off keying (OOK) to differential phase-shift keying (DPSK) format conversion and all-optical DPSK regeneration are proposed and analyzed theoretically.

In order to improve the wavelength conversion bandwidth of cross polarization modulation (XPoM) in a semiconductor optical amplifier (SOA), a novel conversion scheme named differential cross-polarization conversion (DXPoM) is proposed, and it is realized by simply adding an extra birefringence delay line in the conventional XPoM. In this part, both the large-signal simulation and small-signal model of DXPoM are developed, and they successfully predict results that agree with experimental outcomes. The large-signal simulation of DXPoM evidently shows the performance improvement and match well with experimental results. The small-signal model gives more comprehensible and intuitive physical insight of DXPoM.

For format conversion, using the cross-phase modulation (XPM) effect in a nonlinear photonic crystal fiber (PCF), the conversion of OOK-to-DPSK is achieved at 40 Gb/s for the first time. Because the PCF has high linear birefringence, and its birefringent axes remain for entire length, launching the probe at 45° relative to the birefringence axes of

the PCF and having the pump-probe detuning (PPD) greater than ~ 6 nm can realize polarization-insensitive XPM-based conversion. The polarization- and PPD-dependent nonlinear phase shift is investigated theoretically. It indicates improper nonlinear strength could generate insufficient phase shift ($< \pi$) in XPM-based conversion, and the amplitude noise (AN) of an OOK pump will also be converted into the phase noise (PN) of the converted DPSK signal, the penalties induced by these issues are discussed analytically as well.

Because the DPSK format carries information on the phase domain, it is influenced by both AN and PN. Therefore, except amplitude regeneration, the regeneration of DPSK signals has to preserve phase information or eliminate PN. A novel all-optical phase noise averager (PNA) is proposed to reduce residual PN in the DPSK transmission system with phase-preserving amplitude regenerators. It can increase the correlation between the PNs of neighboring bits and greatly reduce the differential PN in the transmission system. Considering various PN, the multiple PN averaging effect is investigated, and the effective PN is convergent regardless of the transmission distance. Furthermore, theoretical bit error rates of the DPSK format with various regeneration schemes is presented for comparison.

誌 謝

Table of Contents

List of Tables

List of Figures

List of Abbreviations

AMI	alternate-mark inversion
AN	amplitude noise
ASE	amplified spontaneous emission
BER	bit error rate
BPSK	binary phase-shift keying
CW	continuous wave
DB	duobinary
DCF	dispersion compensating fiber
DI	delay interferometer
DPSK	differential phase-shift keying
DQPSK	differential quadrature phase-shift keying
DXPoM	differential cross-polarization modulation
EAM	electro-absorption modulator
EDFA	Erbium doped fiber amplifier
ER	extinction ratio
FWHM	full width at half maximum
FWM	four wave mixing
GVD	group-velocity dispersion
HNLF	highly nonlinear fiber
IFWM	intra-channel four wave mixing
iid	independent identically distributed
IN	intensity noise
ISPM	isolated pulse self-phase modulation
IXPM	intra-channel cross-phase modulation
LN-MZM	$LiNbO_3$ Mach-Zehnder modulator
MAN	metropolitan area network
MPS	minimum phase system
MZI	Mach-Zehnder interferometer
NF	noise figure
NLS	nonlinear Schrödinger
NOLM	nonlinear optical loop mirror
NRZ	non-return-to-zero
OADM	optical add-drop multiplexer
OOK	on-off keying
OSA	optical spectral analyzer
OSNR	optical signal-to-noise ratio
OXC	optical cross-connect
PC	polarization controller
PCF	photonics crystal fiber
pdf	probability density functions
PLL	phase-lock loop
PM	polarization maintained

PN	phase noise
PNA	phase noise averager
PPAR	phase-preserving amplitude regenerator
PPD	pump-probe detuning
PRBS	pseudo random binary sequence
PS	polarization scrambler
PSA	phase-sensitive amplifier
QAM	quadrature-amplitude modulation
RMS	root mean square
RZ	return-to-zero
SBS	stimulated Brillouin scattering
SNR	signal-to-noise ratio
SOA	semiconductor optical amplifier
SOP	state of polarization
SPM	self-phase modulation
SSMF	standard single mode fiber
STD	standard deviation
TE	transverse electronic
TIA	transimpedance amplifier
TM	transverse magnetic
TMM	transfer matrix method
WDM	wavelength division multiplexing
XGM	cross-gain modulation
XPM	cross-phase modulation
XPoM	cross-polarization modulation
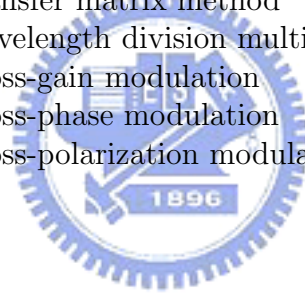
Chapter 1

Introduction

1.1 All-optical signal processing

Due to the advancement of optical communications since 1980s [1], the main function of public communications networks has been modified from voice-only telephony to the data transfer created by internet applications. In fact, while the huge growing requirement of communication bandwidth drives the evolution of optical communication networks at an accelerating rate, the new era for communication networks has come and moved this world toward a global village [2].

Owing to the requirement of network capacity, the line bit rate and the channel number of wavelength division multiplexing (WDM) systems are increasing. Furthermore, the need to enhance network efficiency is also driving traditional point-to-point WDM networks towards meshed flexible WDM networks [3], as shown in Fig. 1.1. Accordingly, the capacity and speed of signal processing in optical networks are increasing dramatically. If the processing is carried out in electrical domain, expensive high-speed electronic components, such as electrical amplifiers, optical modulators and photodetectors, must be provided. In order to lower the cost of optical networks, the number of optoelectronic interfaces has to be minimized. Consequently, all-optical signal processing which can realize transparent optical networks without using O/E/O conversion are required in future cost-effective networks. Various all-optical signal processing have been investigated, such as packet switching [4], logic gates [5], demultiplexing [6][7], wavelength conversion

[8]-[11], format conversion [12]-[14] and regeneration [15]-[20].

To enable a flexible meshed network topology, the functionality and design of optical cross-connects (OXC) and optical add-drop multiplexer (OADM) are key issues. The basic functionalities of these new network elements are switching and routing, which provide the connectivity between the channels on the input ports and those on the output ports [21][22]. Actually, switching and routing in WDM networks can be realized through controlling and converting signal wavelength. Furthermore, the number of wavelength in WDM networks which corresponds to the number of independent wavelength addresses is generally not enough to support all the nodes of a huge network. While two channels with the same wavelength might be routed to the same output port, the blocking probability would rise due to time-slot contention. Wavelength conversion can also overcome this limitation. Therefore, all-optical wavelength converters can increase the flexibility and reduce blocking probability of networks, and have been treated as key components in WDM systems.

In long-distance fiber transmission, optical noise from in-line optical amplifiers and other active optical devices and fiber impairments, such as dispersion and nonlinear effects, can degrade signal performance significantly in transmission. Actually, even in a small-size network, multiple filtering in OXC or OADM can also degrade optical signals. All-optical signal regenerators could be inserted to regenerate optical signals and improve the quality of optical signals, and therefore, they can increase transmission distance and relax the limit of multiple filtering and launch power [17]. Generally speaking, regeneration can be only 1R (re-amplifying), 2R (re-amplifying + re-shaping) or 3R (re-amplifying + re-shaping + re-timing). Among them, the basic function, re-amplifying, can be simply accomplished by optical amplifiers. Hence, how to realize all-optical signal re-shaping is

WDM transmission

WDM transmission with add/drop

WDM rings with node addressing

Mesh networks with full connectivity

Interconnected multi-ring topology

Technology evolution
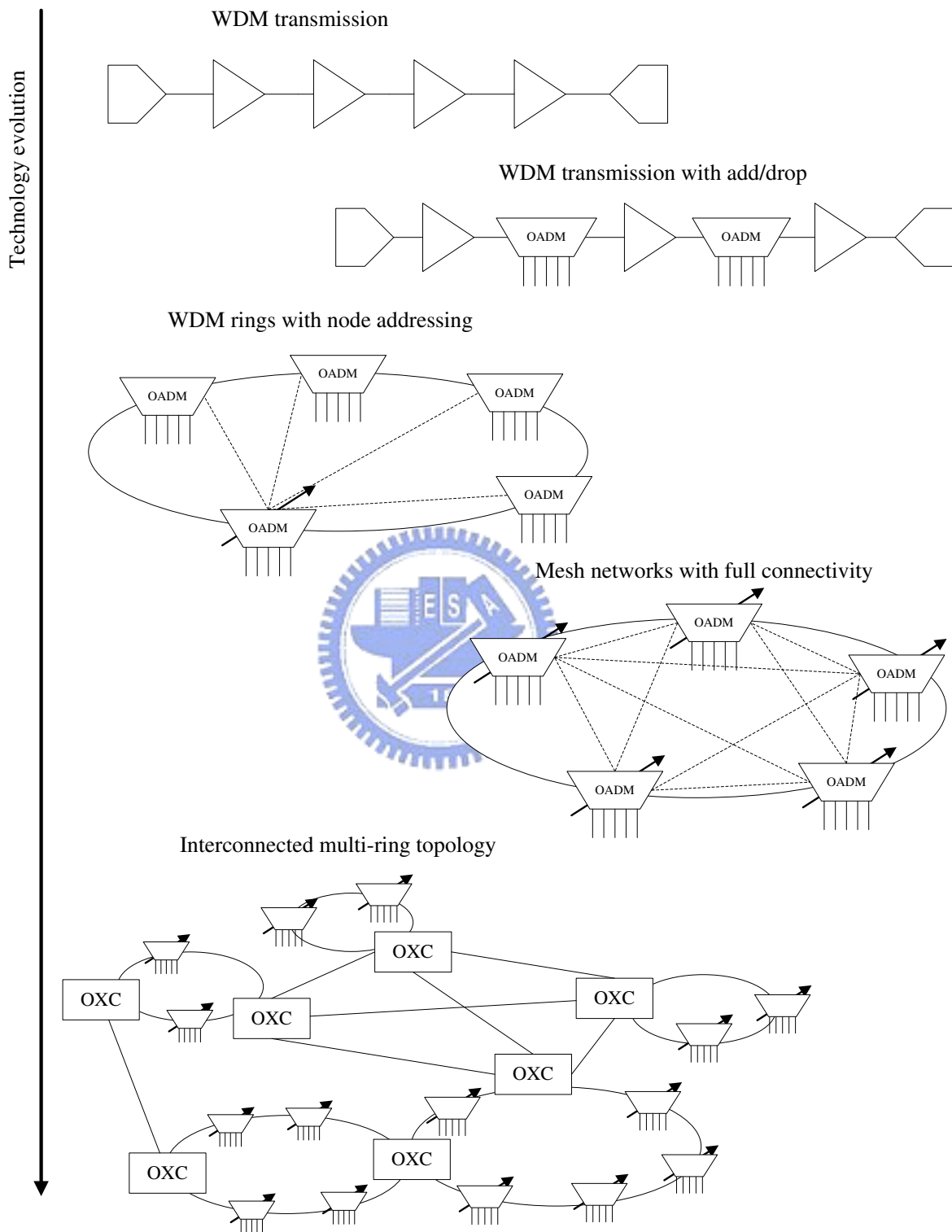
Figure 1.1: The evolution of WDM networks

3

the first thing in transparent regenerators.

Recently, advanced modulation formats have attracted much attention due to their various advantages [23], such as better spectral efficiency, chromatic dispersion tolerance, nonlinear tolerance, and sensitivity to achieve error free, compared with traditional on-off keying (OOK). However, to obtain these advantages, one has to pay the price of a more complex and expensive transmitter or receiver. Considering both cost and system requirement, the most suitable modulation format varies in different network architectures, and therefore, all-optical format converters at the node between different networks could connect different modulation formats transparently [12]. Otherwise, an optical network might carry mixed-format signals, and cannot achieve the optimal performance [24].

In the dissertation research, the all-optical wavelength conversion, format conversion and regeneration are covered. To increase the cascadability of wavelength conversion, the modified approach of wavelength conversion is proposed to improve conversion speed. Because the advanced format of differential phase-shift keying (DPSK) carries information on the optical phase domain, a novel method is proposed to manage the phase of DPSK signals. Moreover, a polarization-insensitive OOK-to-DPSK conversion was carried out in a birefringent fiber to avoid mixed-format transmission. In the following sections, the dissertation works with regard to these three parts are introduced further.

1.2 Speed enhancement of semiconductor optical amplifier-based wavelength conversion

All-optical wavelength converters based on semiconductor optical amplifiers (SOA) are promising due to their compact and potentially inexpensive properties. Several SOA-based wavelength converters have been proposed, such as cross-gain modulation (XGM)

4

[8], cross-phase modulation (XPM) [8], cross-polarization modulation (XPoM) [9][10], and four wave mixing (FWM) [11]. Each scheme has its own advantages and disadvantages. For example, FWM has low conversion efficiency, and XGM, due to the limitation of carrier's recovery time, has lower conversion speed and higher frequency chirping. Among all these parameters, conversion speed is considered to be one of the most important factor. This is because insufficient speed response causes larger timing jitter and thus limits cascadability [25].

XPoM is operated on the interferometric principle similar to the Mach-Zehnder interferometer (MZI), given that it exploits the varied phase difference between the transverse electronic (TE) and transverse magnetic (TM) modes of the CW beam induced by the signal beam as the probe beam passes through an SOA. Therefore, similar to XPM which also bases on MZI, XPoM has several advantages, such as pulse reshaping and unrestrained conversion logics [10]. Nonetheless, XPoM is a more economic conversion scheme because only one SOA is needed compared with XPM which typically needs two SOAs. Furthermore, adding an extra delay line to one arm of either XPM or XPoM scheme [26][27] can realize high speed wavelength conversion of return-to-zero (RZ) format, and this kind of modified scheme is unrestricted by the relaxation tail of carrier depletion and recovery in SOAs. Actually, it has been proposed that the similar XPM scheme can also improve the conversion speed of non-return-to-zero (NRZ) format [28]. By adding an extra birefringence delay line in the conventional XPoM, a novel conversion scheme is proposed to improve the speed performance, named differential cross-polarization modulation (DXPoM).

To investigate DXPoM, both the large-signal model and small-signal model of DXPoM are developed and successfully predict results that agree with experimental outcomes.

The large-signal model, based on time dependent transfer matrix method (TMM) [9], of DXPoM evidently shows the improvements of rise time, timing jitter and extinction ratio (ER). The small-signal model, based on frequency domain Fourier transform approach, gives more comprehensible physical insight of DXPoM. From the small-signal model, analytic expressions are elaborated to show that the modulation bandwidths of XPoM and XGM are identical and limited by the carrier's recovery time. From the transfer function of DXPoM, the relations between the modulation bandwidth, the delay time, the operating points, the parameters of an SOA and the conversion logics, are clearly described in both frequency and time domains.

1.3   All-optical OOK-to-Binary phase-shift keying conversion

In DPSK format, an optical pulse appears in each bit slot with the binary data encoded as either a zero or π phase shift between adjacent bits. This format emerged as an alternative to OOK format, especially for long-haul transmission [29]. The most obvious advantage of DPSK format with balanced detection over OOK is that its optical signal-to-noise ratio (OSNR) required to reach a given bit error rate (BER) is approximately 3 dB lower, which implies that the maximum transmission distance could be approximated double if a linear system is considered. However, DPSK format requires more complex transmitter and receiver. Accordingly, DPSK and OOK formats are suitable for networks with different sizes. While the size of networks is large and the transmission distance is long, such as long-hual backbone networks, the DPSK format could be the better one. Oppositely, OOK format should be adopted in a network with smaller size, such as metropolitan area networks (MAN). However, without format conversion in the gateway nodes between networks with different modulation formats, OOK and DPSK formats may

be mixed in a WDM system, and it has been found that the phase information of DPSK signals would be seriously distorted by OOK signals through the inter-channel XPM effect [24]. As a result, an OOK-to-DPSK modulation format converter is needed in the nodes to avoid mixed-format transmission.

Intuitively, converting intensity-modulated format to phase-modulated format, such as OOK to binary phase-shift keying (BPSK), can be achieved by using power-dependent XPM effect in a nonlinear medium, such as highly nonlinear fiber (HNLF) and an SOA. While the space of OOK signals do not induce nonlinear phase shift to another probe beam, the mark with specific power is supposed to generate π phase shift to encode binary data on the phase of the probe beam. However, to avoid error propagation at the receiver side while BPSK signals are demodulated by a delay interferometer (DI), the binary data have to be precoded in advance. Basically, this precoding is not a problem, and it can be simply done before generating OOK signals. Therefore, the issue about precoding or how to convert BPSK to DPSK will not be discussed in this dissertation. Moreover, although SOAs could realize polarization insensitive format conversion [13], DPSK signals would be degraded by the XGM effect and slow response time of SOAs, which can be avoided by using ultra-fast ($\sim$fs) χ^3 effect in HNLF [14]. Nevertheless, this fiber-based format converter is polarization sensitive. Recently, a novel photonics crystal fiber (PCF) has been discovered that its birefringent axes remain fixed over the entire length, and this characteristic can perform polarization-independent [7] or polarization-insensitive [30] XPM effect. Using the similar approach, a polarization-insensitive 40 Gb/s RZ-OOK-to-RZ-BPSK format conversion can be realized in a highly nonlinear PCF, and the experimental and theoretical results are shown in this dissertation. The theoretical part also analyzes the penalty of DPSK signals induced by insufficient phase shift, which

originates from improper nonlinear strength or polarization mismatching. Furthermore, as using amplitude-to-phase conversion, the amplitude noise (AN) of OOK signals will also be transferred to the phase noise (PN) of converted DPSK signals. How the OSNR of OOK signals influence the performance of DPSK signals will be carried out theoretically.

1.4   All-optical phase noise suppression of DPSK signals

Compared with OOK signals, besides ∼3-dB lower OSNR required, DPSK signals are also less sensitive to nonlinear effects due to lower peak power and the same power of each pulse, particularly those of self-phase modulation (SPM) and inter-channel XPM [31], improved dispersion tolerance and high spectral efficiency [32]. However, without considering timing jitter, unlike OOK systems that are limited only by AN, DPSK systems are affected by both AN and PN. The PN in DPSK systems will be converted to AN in the receiver through a DI. Furthermore, the PN contains linear PN and nonlinear PN. In dispersion-managed systems, AN and linear PN are generated mainly from the amplified spontaneous emission (ASE) noise of optical amplifiers. The nonlinear PN is translated from AN through the fiber Kerr effect, often called the Gordon-Mollenauer effect [33], and dispersion-induced pattern effects through XPM in WDM systems [34].

Either PN or AN must be prevented from being accumulated to expand the reach of DPSK systems. Unfortunately, most of the all-optical regeneration schemes for OOK format [15]-[17] do not fit the DPSK format, because the phase information is distorted by these regenerators. Theoretically, a phase-sensitive amplifier (PSA) can simultaneously reduce both AN and PN, and the regeneration was experimentally demonstrated by pumping a PSA with an original undistorted DPSK signal [18]. Even so, the coherent pump beam required to achieve a regenerative PSA is difficult to realize in the real world,

owing to the requirement of optical-carrier phase-locking between the pump beam and the signal beam. Additionally, several phase-preserving amplitude regeneration approaches for DPSK format have been proposed [19][20]. The reduction of AN is such that the nonlinear PN caused by the Gordon-Mollenauer effect will be reduced [20], and therefore, the transmission distance will be extended due to the reduction of both AN and nonlinear PN. Nevertheless, these regenerators can constrain only some of the nonlinear PN and preserve the original linear PN, and the accumulated PN still distorts DPSK signals and limits the transmission distance.

In this dissertation, a novel all-optical phase noise averager (PNA) based on a PSA is proposed. This PNA can average the PN of one bit with that of its neighboring bit coherently and an extra phase-locking pump beam is not required. These PNAs can increase the correlation between neighboring PNs, effectively diminish differential PN, and greatly extend the reach of DPSK signals. The most important and appealing feature of the proposed PNA is that, when cascaded, the chain of PNAs results in the convergent variance of PN. Particularly, in amplitude-managed linear systems with repeated PNAs, the total differential PN is always less than that before the first averager and is irrelevant to the number of spans.

Recently, a nonlinear optical loop mirror (NOLM) with an SOA [35][36] has been found to yield PN suppression of DPSK signals. Later, this PN suppression has been shown to be achieved by increasing the correlation between neighboring PNs, similar to PN averaging [37]. In this approach, the residual AN after PN averaging could be simply neglected, and it is easier to be analyzed. Hence, to further investigate the efficacy of PN averaging based on the other approach [37], the theoretical analysis of sensitivity improvement by PN averaging is also carried out.

1.5 Organization of the dissertation

In chapter 1, the introduction of all-optical signal processing and the subjects covered in the dissertation are included. In chapter 2, after introducing the concept of XPoM and DXPoM, large-signal simulation, experimental realization and theoretical small-signal analysis are given. In chapter 3, the properties of OOK and DPSK formats are discussed in advance. The concept, theory and experiment of polarization-insensitive OOK-to-DPSK conversion are provided, and then, the impairment due to OOK-to-DPSK conversion is analyzed. In chapter 4, the concept and realization of a PNA are given, as well as the effects of PN averaging on various kinds of PN. Additionally, the PN averaging is examined by the theoretical analysis of error probability. Finally, the conclusions are give in chapter 5.

Chapter 2

Differential cross-polarization modulation in an SOA

2.1 Cross-polarization modulation in an SOA

2.1.1 Concept of XPoM

Figure 2.1 illustrates the conept of XPoM. When a signal pump beam at wavelength λ_{pump} is fed into an SOA, the signal light will modulate the carrier density of the SOA. In addition, a continuous wave (CW) beam (called the probe) which is placed at the desired output wavelength λ_{probe} is transmitted into the SOA simultaneously. Owing to the asymmetric waveguide geometry, the confinement factors, effective guide refractive indices and carrier distribution of an SOA are not identical at TE and TM orientations, and these differences correlate monotonously with the input signal power through the SOA. When the pump power changes, the nonlinear polarization rotation of the probe beam is induced through carrier density modulation. Moreover, this polarization modulation can be converted into intensity modulation by a polarizer after the SOA, and the ER and the conversion logic of the converted signal can be selected by properly controlling the polarizer in the XPoM scheme. However, the conversion speed of XPoM is limited by the carrier's response.

2.1.2 Concept of DXPoM

Figure 2.2 presents the configuration of DXPoM. As in a typical XPoM, properly controlling the states of polarization (SOP) of λ_{pump} and λ_{probe} allows the injected pump light

11
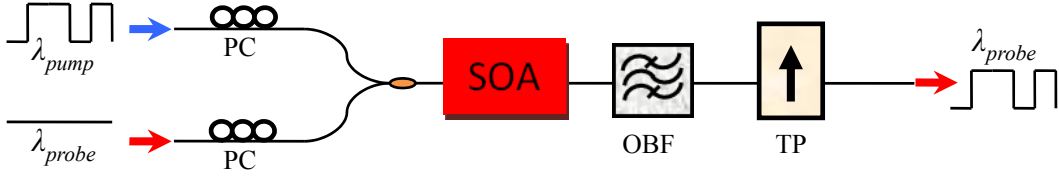
Figure 2.1: Concept of an XPoM wavelength converter. (PC: polarization controller, OBF: optical bandpass filter, and TP: tunable polarizer)

to introduce additional birefringence in the SOA, resulting in a change in the difference between the refractive indices of the TE and TM modes of the probe beam. At the polarizer, these two orthogonal modes are partially combined coherently. Namely, the XPoM exploits the phase difference between the TE and TM modes, when the probe beam passes through the SOA, to rotate the polarization state. This phase difference, controlled by the signal power, determines the output power of the CW beam after it has passed through a polarizer. While an extra birefringent delay line is added in front of the polarizer in the DXPoM, the conversion speed of the traditional XPoM could be improved. A simplified and intuitive example illustrated in Fig. 2.3 can help to imagine why this extra delay line improves the conversion speed. Figure 2.3 shows two sinusoidal waves with the same angular frequency, Ω, but different amplitudes, ϕ_a and ϕ_b. The difference between these two waves is also a sinusoidal wave with frequency, Ω, and amplitude, ϕ_c. If the time offset, Δt, as presented in Fig. 2.3, is applied, then the differential amplitude becomes $\phi_c^2 = \phi_a^2 + \phi_b^2 - 2\phi_a\phi_b \cos(\Omega \Delta t)$. For $\Omega < \pi/\Delta t$, the differential amplitude increases with frequency. Namely, properly selecting Δt increases the differential amplitudes at some high frequencies. Accordingly, adding an extra delay between the TE and TM modes may amplify some high-frequency components of the phase difference in DXPoM, to compensate the insufficient frequency response associated with the long lifetime of the carriers

12

in an SOA. As a result, the SOP of the output CW beam after the delay line is rotated more rapidly as the signal power varies. In other words, DXPoM has a higher conversion speed and a better performance, compared with XPoM.
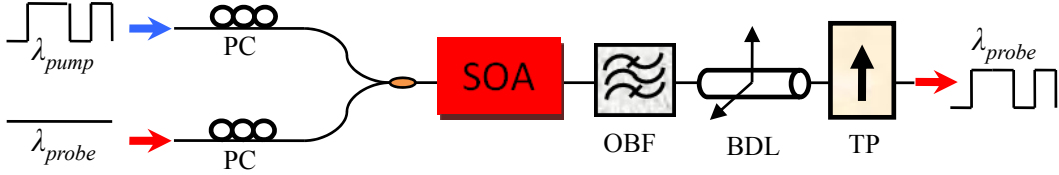
Figure 2.2: Concept of a DXPoM wavelength converter. (PC: polarization controller, OBF: optical bandpass filter, BDL: birefringent delay line, and TP: tunable polarizer)
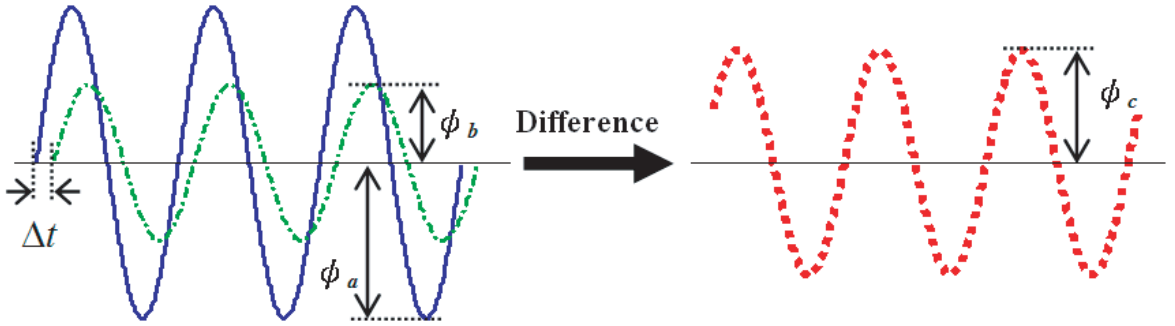
Figure 2.3: Illustration of a differential sinusoidal wave

2.2 Large-signal model

2.2.1 Simulation model of SOA-based wavelength converters

An SOA is generally treated as a two-level system, which is an approach suitable for gaseous and solid state amplifiers. It can be extended for SOAs, if the active region is modeled as a collection of non-interacting two-level systems with transition energies extending over the whole range of the conduction and valence bands. By assuming the

input signal pulse width to be much larger than the intraband relaxation time which governs the dynamics of the induced polarization, the considerable simplification which neglects the intraband processes could be held. In general, the condition for simplification is typically held when signal pulse width is larger than 1 ps. In this approximation, the rate equation of the carrier density in an SOA, N, which responds to the optical power, P, are described by [38],

$$\frac{\partial N}{\partial t} = \frac{I}{qV} - \frac{N}{\tau_s} - \sum_i \sum_k \frac{g_k P_{ik}}{\hbar \omega_i A_{\text{eff}}} , \tag{2.1}$$

where $i = 1, 2$ represent the pump and the probe beam, respectively; $k = e, m$ represent TE and TM component; I is the injection current; q is the elementary charge, V is the active volume; g is the material gain; $\hbar$ is the reduced Planck constant; ω_i is the optical angular frequency; A_{eff} is the effective area of the waveguide, and τ_s is the lifetime of the carriers governed by spontaneous emission and nonradiative recombination. In large-signal model, τ_s is dependent on the carrier density,

$$\tau_s = \frac{1}{c_1 + c_2 N + c_3 N^2} , \tag{2.2}$$

where c_1, c_2 and c_3 are the coefficients of nonradiative recombination rate, radiative recombination rate and Auger recombination rate, respectively. Moreover, the rate equation of slow-varying optical envelope, $A_{ik} = \sqrt{P_{ik}} \exp(j\phi_{ik})$, is given by,

$$\frac{\partial A_{ik}}{\partial z} + \frac{1}{v_g} \frac{\partial A_{ik}}{\partial t} = \frac{1}{2} \Gamma_k (1 - j\alpha_H) g_k A_{ik} - \frac{1}{2} \alpha_w A_{ik} , \tag{2.3}$$

where ϕ is the phase of optical field; v_g is the group velocity; Γ is the confinement factor; α_w is the waveguide loss, and α_H is the linewidth enhancement factor. To consider two orthogonal polarization component interacting indirectly by the carriers, the polarization dependent material gain can be modeled as [39],

$$g_k = \frac{\sigma_{gk}(\eta_k N - N_0)}{1 + \epsilon S_k} , \tag{2.4}$$

14

where σ_g is the differential gain coefficient; N_0 is the carrier density at transparency; ϵ is the gain compression factor; S_k is the total photon density in k mode,

$$S_k = \sum_i \frac{P_{ik}}{v_g \hbar \omega_i A_{\text{eff}}} ,$$

and η_k is the modified imbalance factor used to describe the asymmetry of optical transitions between TE and TM modes, when extra strain is built into the active layer of an SOA in order to make an SOA polarization insensitive. This factor is accounted for by an imbalance factor f [9],

$$\begin{aligned}
\eta_e &= \frac{2}{3}\left(\frac{1+2f}{1+f}\right) , \\
\eta_m &= \frac{2}{3}\left(\frac{2+f}{1+f}\right) .
\end{aligned} \tag{2.5}$$

If extra strain is not applied, then both f and η_k are unity, and the optical transition is almost isotropic.

Based on Eqs. (2.1) and (2.3), the large signal model is performed by the time-dependent TMM [40][41]. The basis of the TMM is to divide a laser structure longitudinally into a number of sections where the structural and material parameters are assumed to be homogeneous throughout each section. However, the parameters may vary between sections to allow longitudinal inhomogeneities, such as those produced by longitudinal spatial hole burning and nonlinear gain, to be incorporated into the model. Each of the sections is characterized by a transfer matrix which modifies the forward and backward traveling waves as they propagate though the section. The use of the TMM here is different from that in the steady-state model where the objective is to obtain the overall transfer matrix for the structure from which the oscillation characteristics are determined. In this application, the parameters of the individual section are renovated in time by updating the traveling-wave amplitudes as passing through a section.

15

In general, the transfer matrix, $\mathbf{T}_l$ of the lth section expresses the following relationship:

$$\begin{bmatrix} A_{f,l+1} \\ A_{b,l+1} \end{bmatrix} = \mathbf{T}_l \begin{bmatrix} A_{f,l} \\ A_{b,l} \end{bmatrix}, \tag{2.6}$$

where A_f and A_b are the forward and backward fields, as shown in Fig. 2.4. However, Eq. (2.6) implies steady-state operation, and to develop a time-dependent implementation of TMM, the transfer matrix should be expressed as $\mathbf{T}_l(t)$. Moreover, if the input fields are $A_{f,l}(t)$ and $A_{b,l+1}(t)$, the output fields of the section should be $A_{f,l+1}(t + \Delta t)$ and $A_{b,l}(t + \Delta t)$, where Δt is the transit time of each section. Assuming that $\mathbf{T}_l(t)$ remains unchanged over the interval, $t \sim t + \Delta t$, Eq. (2.6) can be written as,

$$\begin{bmatrix} A_{f,l+1}(t + \Delta t) \\ A_{b,l+1}(t) \end{bmatrix} = \begin{bmatrix} \mathbf{T}_{l11}(t) & \mathbf{T}_{l12}(t) \\ \mathbf{T}_{l21}(t) & \mathbf{T}_{l22}(t) \end{bmatrix} \begin{bmatrix} A_{f,l}(t) \\ A_{b,l}(t + \Delta t) \end{bmatrix}. \tag{2.7}$$

Rearranging Eq. (2.7) produces the expression for the updated fields in terms of the past fields and the transfer matrix elements, it becomes,

$$\begin{bmatrix} A_{f,l+1}(t + \Delta t) \\ A_{b,l}(t + \Delta t) \end{bmatrix} = \begin{bmatrix} \mathbf{T}_{l11}(t) - \dfrac{\mathbf{T}_{l12}(t)\mathbf{T}_{l21}(t)}{\mathbf{T}_{l22}(t)} & \dfrac{\mathbf{T}_{l12}(t)}{\mathbf{T}_{l22}(t)} \\ -\dfrac{\mathbf{T}_{l21}(t)}{\mathbf{T}_{l22}(t)} & \dfrac{1}{\mathbf{T}_{l22}(t)} \end{bmatrix} \begin{bmatrix} A_{f,l}(t) \\ A_{b,l+1}(t) \end{bmatrix}. \tag{2.8}$$
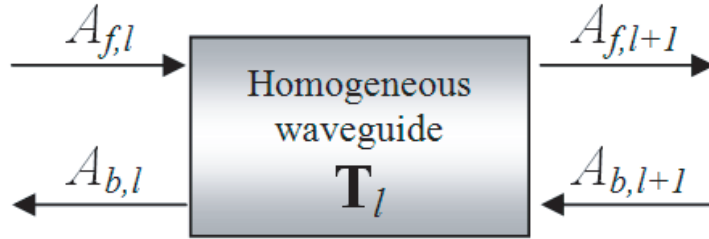
Figure 2.4: Schematic transfer matrix

2.2.2 Simulation results of DXPoM

The parameters used in the simulation are summarized in Table 2.1. The OOK pump signal is simulated by super Gaussian pulses with the order of 3, and the pattern is the pseudo random binary sequence (PRBS) of $2^7 - 1$. The input powers of the pump and probe beams are 2 and 5 dBm, respectively.

Using time-dependent TMM and the rate equations, the simulation results are shown in Figs. 2.5-2.9. Figs. 2.5-2.7 compare the simulated eye diagrams of 10 Gb/s wavelength conversion employing XPoM, DXPoM with TM delay, and DXPoM with TE delay, respectively. In Fig. 2.6, the extra delay added on the TM mode was 13 ps, and in Fig. 2.7, the extra delay added on the TE mode was also 13 ps. These figures illustrate that DX-PoM with TM delay performs much better than the other schemes. The ER is better, the timing jitter is lower and the rise time is markedly improved. However, if the extra delay is added on the TE mode, the conversion performs is even worse than that of XPoM. Because the power gain at the TE mode is 1 dB higher than that at the TM mode in the simulation model, the TE mode induces larger phase changes than the TM mode, as shown in Fig. 2.8. Fig. 2.9 compares the phase difference between the TE and TM modes corresponding to Figs. 2.5-2.7. Due to the asymmetric shape of the phase variation, the phase difference introduced by adding TM delay shows a square-wave type of sharp transition and flatness. Conversely, the phase difference by adding TE delay show continuously slow rising and falling bit patterns. Due to the interferometric principles of XPoM, the phase difference between the TE and TM modes principally controls the output power of the CW beam after the polarizer. Therefore, a square wave style phase difference translates into a square wave style intensity pattern. Furthermore, the slow and irregular rising and falling differential phase bit patterns cause a larger timing jitter

Table 2.1: Device parameters

Symbol	Description	Value	Unit
Γ_e	Confinement factor in TE mode	0.2	
Γ_m	Confinement factor in TM mode	0.15	
L	SOA length	5×10^{-4}	m
c_1	Nonradiative recombination rate constant	1×10^8	s^{-1}
c_2	Radiative recombination rate constant	2.5×10^{-17}	m^3s^{-1}
c_3	Auger recombination rate constant	9.4×10^{-41}	m^6s^{-1}
σ_{ge}	Differential gain coefficient in TE mode	2×10^{-20}	m^2
σ_{gm}	Differential gain coefficient in TM mode	2×10^{-20}	m^2
N_0	Carrier density at transparency	1.1×10^{24}	m^{-3}
v_g	Group velocity	7.5×10^7	$\text{m}\,\text{s}^{-1}$
ϵ	Gain compression factor	1.3×10^{-23}	m^3
α_H	Linewidth enhancement factor	5	
α_w	Waveguide loss	1.5×10^4	m^{-1}
f	Imbalance factor	0.5	

and eye closure. This roughly explains why the TM delay outperforms the TE delay.
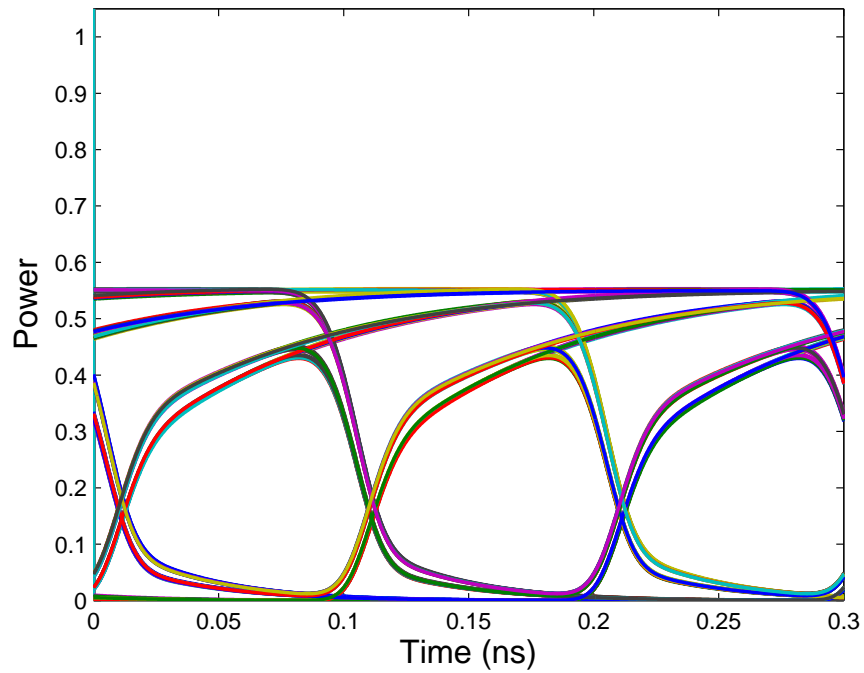
Figure 2.5: Simulated eye-diagram of converted signal based on XPoM
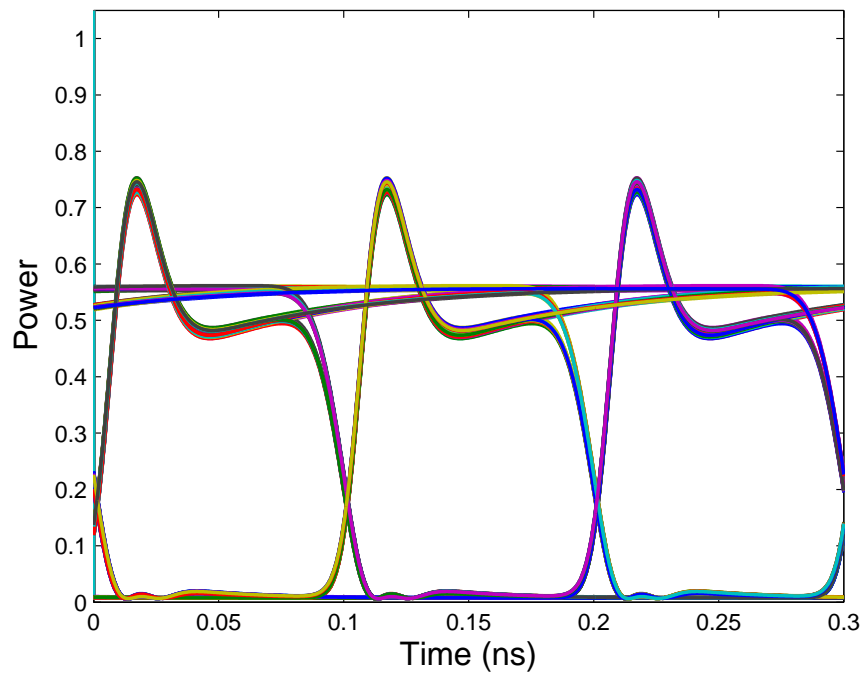
Figure 2.6: Simulated eye-diagram of converted signal based on DXPoM with TM delay
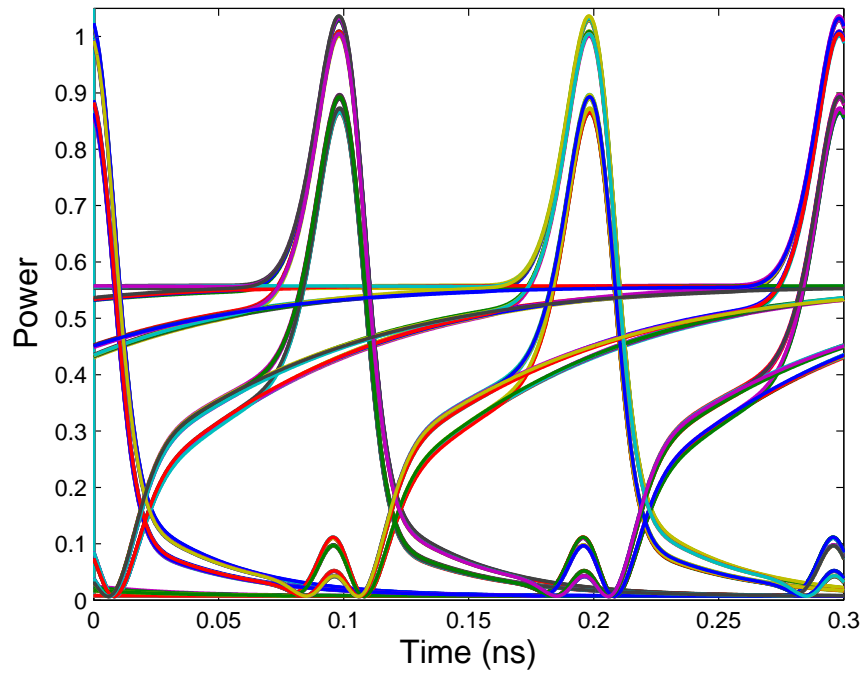
Figure 2.7: Simulated eye-diagram of converted signal based on DXPoM with TE delay
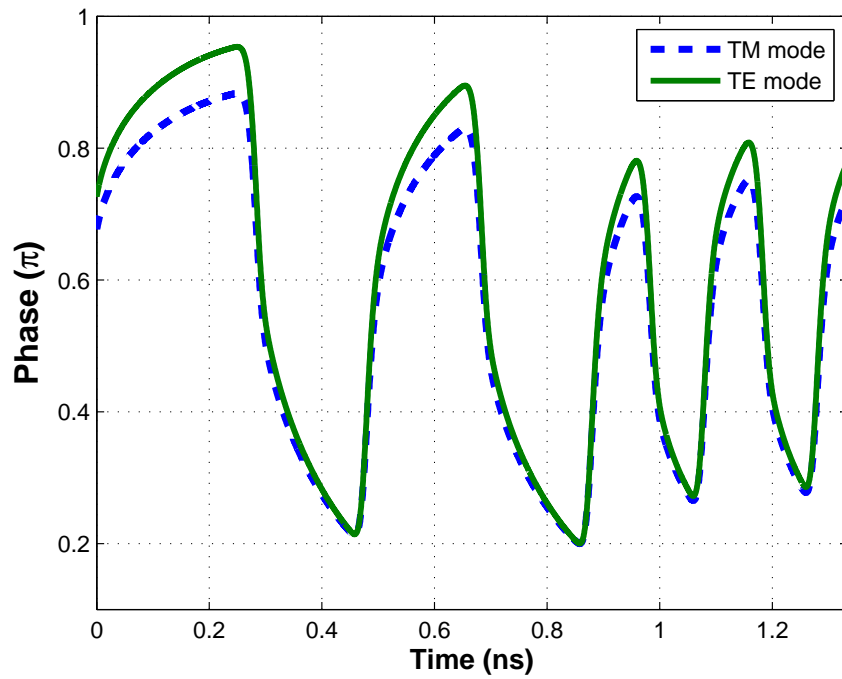
Figure 2.8: The output phase of TM and TE modes
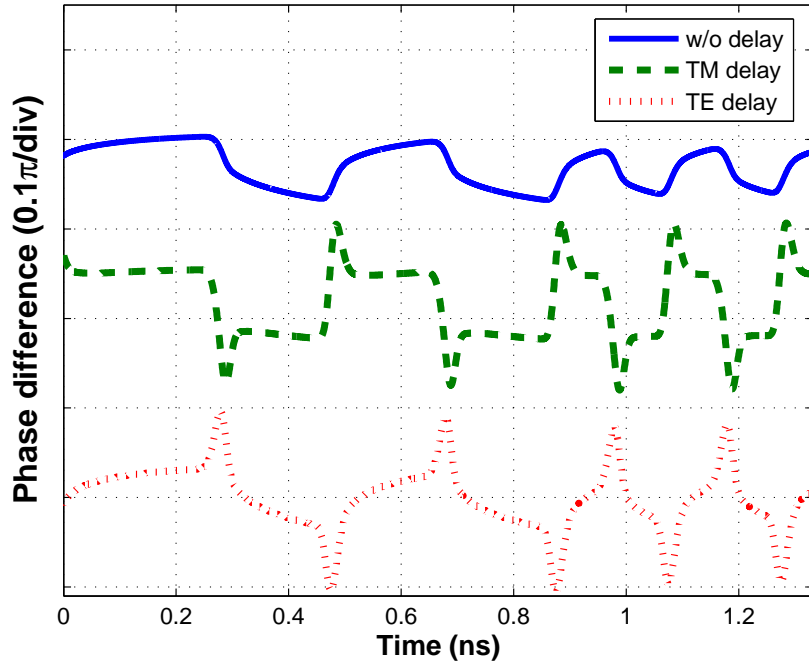
Figure 2.9: The phase difference between TM and TE modes
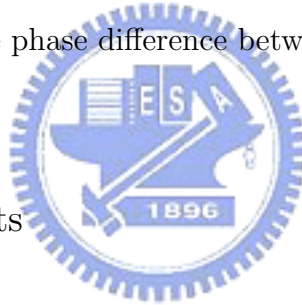
2.3 Experimental results

Fig. 2.10 shows the experimental setup of a DXPoM wavelength converter. A DFB signal pump laser at 1554.9 nm was intensity modulated at 10 Gb/s with a PRBS length of $2^7 - 1$. A tunable CW probe laser at 1548.5 nm was combined with the signal and injected into the SOA. The bias current of the SOA (JDSU CQF872) was set at 300mA. The average power of the DFB and the tunable laser was 1.5 dBm and 5.5 dBm, respectively. After the SOA, the signal pump beam was filtered out by an optical bandpass filter. The combination of the polarization controller (PC) and the Panda polarization maintained (PM) fiber acted as a tunable birefringence delay line. The maximum differential delay introduced by the PM fiber was approximative 14 ps, which was optimized by using PM fibers of different lengths. Proper control of PC3 allowed the relative delay

21

between the TE and TM modes to be adjusted, and this produced a desired DXPoM function. The TE and TM modes were then coherently combined at the polarization beam splitter. Figs. 2.11(a) and (b) display the 10 Gb/s eye diagrams of the measured XPoM and DXPoM, respectively. Comparing Figs. 2.11(a) and (b) revealed that the rise time was improved by more than 300%, from 74 ps to 23 ps, the extinction ratio showed a 9% enhancement, from 11 dB to 12 dB, and the root mean square (RMS) timing jitter decreased by 50%, from 5.4 ps to 2.7 ps. In the configuration of Figs. 2.11(a) and (b), PC4 was adjusted to form a destructive interference between the TE and TM modes when only the CW beam was present, thus non-inverted conversion was obtained. As a comparison, Fig. 2.11(c) shows the eye diagram of XGM with the CW beam of -7 dBm and the signal beam of 2.3 dBm. This demonstrated that the used SOA can not support 10 Gb/s XGM due to the constraint of the carrier's slow recovery time. Fig. 2.12 shows the bit error rate measurement results of source (back-to-back), XPoM and DXPoM. According to this figure, the DXPoM scheme improved the sensitivity by more than 7 dB compared with XPoM. Furthermore, the wavelength conversion itself had a conversion penalty of roughly 1.5 dB compared with the back to back result. The power penalty was contributed mainly by the ASE noise of the SOA by lowering the OSNR. The experiment confirms that the DXPoM is feasible and the performance of the converted signal is improved significantly. However, because the remote pump signal could be arbitrarily polarized after transmitting through fibers, PC1 in Fig. 2.10 has to be an automatic PC to optimize the wavelength converter in practice.
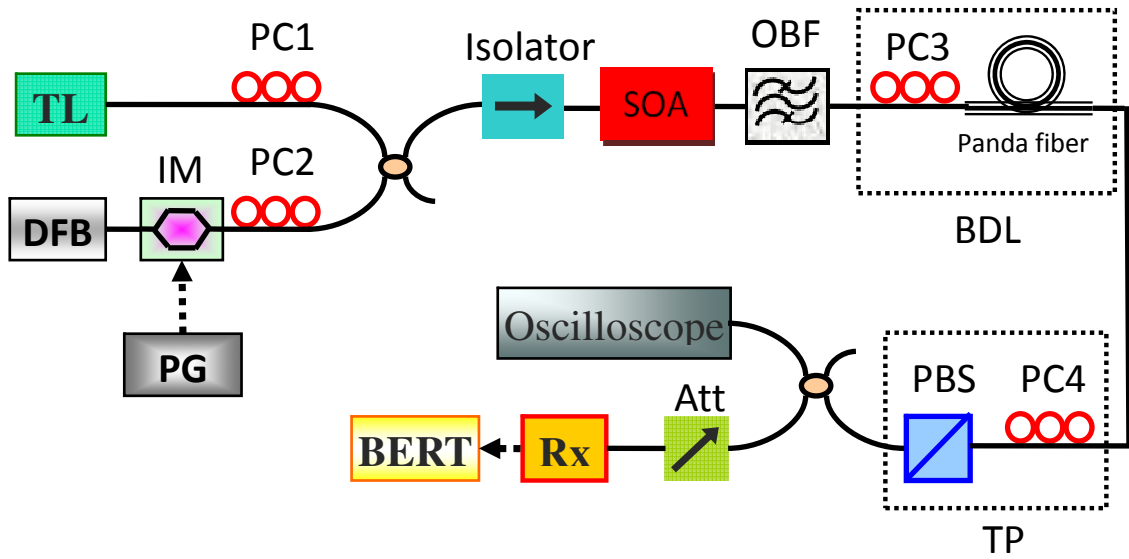
Figure 2.10: Experimental Setup of DXPoM. (TL: tunable laser; IM: intensity modulator; PG: pattern generator; PC: polarization controller; OBF: optical bandpass filter; BDL: birefringent delay line; PBS: polarization beam splitter; TP: tunalbe polarizer; Att: optical attenuator; BERT: bit error rate tester)
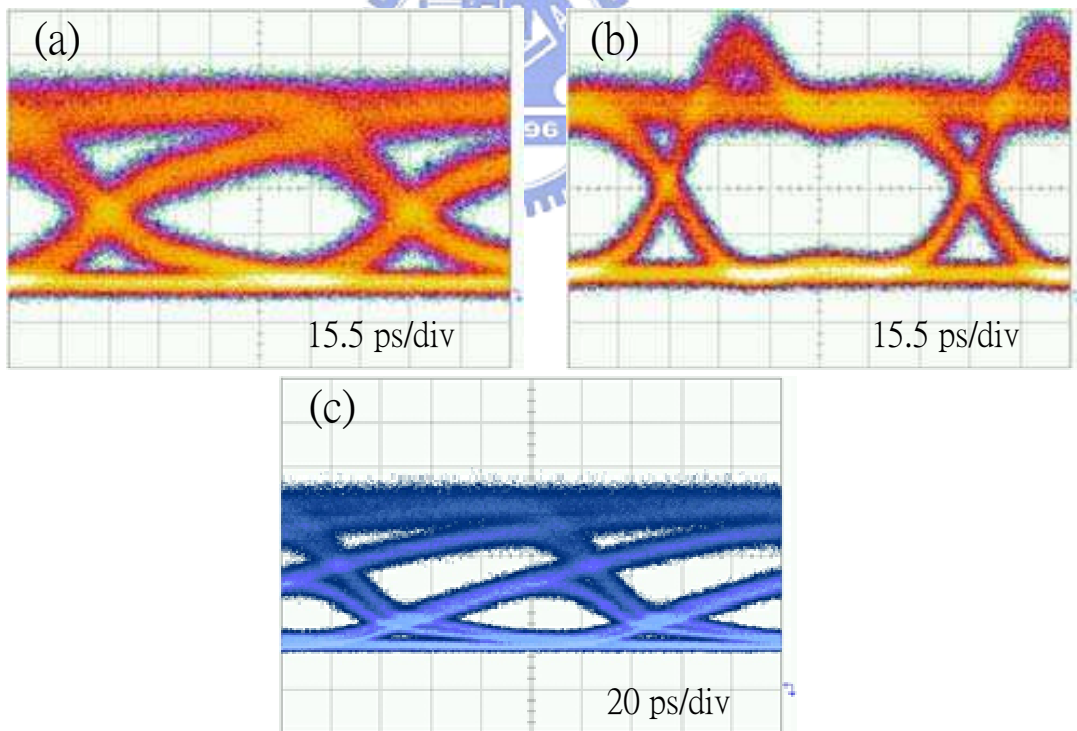
Figure 2.11: Measured eye-diagrams of 10 Gb/s converted signal based on (a) XPoM, (b) DXPoM, and (c) XGM
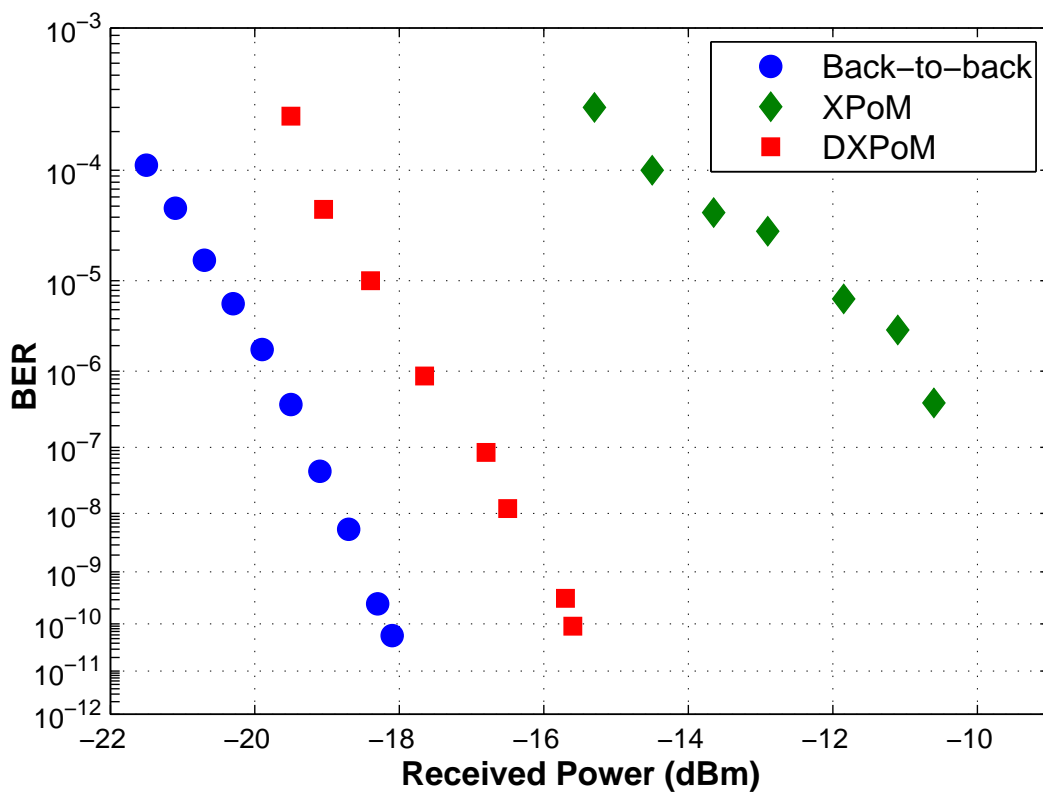
Figure 2.12: BER curves of wavelength conversion at 10 Gb/s

2.4 Small-signal model

Since the time-consuming large-signal simulations and experiments with some invariable parameters are difficult to look into the connections between the conversion performance and other parameters, based on frequency domain Fourier transform approach, the small-signal model was developed to obtain more comprehensible and intuitive physical insight of DXPoM.

2.4.1 Small-signal model of XPoM

Concerning the small-signal model of an SOA [42], the spontaneous carrier lifetime of Eq. (2.2) can be treated as a constant and symbolized by τ_{s0}, owing to nearly constant carrier density. Furthermore, by simplifying Eqs. (2.1), (2.3) and (2.4), the basic prop-

agation functions of the optical fields in different polarization modes in an SOA can be described as,

$$\frac{\mathrm{d}N}{\mathrm{d}t} = \frac{I}{qV} - \frac{N}{\tau_{s0}} - \sum_i \sum_k \left[\sigma_{gk}(\eta_k N - N_0) \frac{P_{ik}}{\hbar \omega_i A_{\text{eff}}} \right], \tag{2.9}$$

$$\frac{\mathrm{d}P_{ik}}{\mathrm{d}z} = \Gamma_k \sigma_{gk}(\eta_k N - N_0) P_{ik}, \tag{2.10}$$

where the retarded time frame, $t - z/v_g \to t$, is adopted, and the waveguide loss and the gain compression effect described by ϵ are neglected. By defining the integrated carrier density as,

$$\mathfrak{N}(t,z) = \int_0^z N(t,z')\,\mathrm{d}z', \tag{2.11}$$

the solution of Eq. (2.10) is,

$$P_{ik}(t,z) = P_{ik}(t,0) \exp[\Gamma_k \sigma_{gk}(\eta_k \mathfrak{N} - N_0 z)], \tag{2.12}$$

and the phase of the probe beam is,

$$\phi_{2k} = -\frac{\alpha_H}{2}\Gamma_k \sigma_{gk}(\eta_k \mathfrak{N} - N_0 z). \tag{2.13}$$

Using Eq. (2.10) and integrating both sides of Eq. (2.9) with respect to z yield,

$$\frac{\mathrm{d}\mathfrak{N}}{\mathrm{d}t} = -\frac{\mathfrak{N} - \mathfrak{N}_0}{\tau_{s0}} - \sum_i \sum_k \frac{P_{ik}(t,z) - P_{ik}(t,0)}{\Gamma_k \hbar \omega_i A_{\text{eff}}},$$

or,

$$\frac{\mathrm{d}\mathfrak{N}}{\mathrm{d}t} = -\frac{\mathfrak{N} - \mathfrak{N}_0}{\tau_{s0}} - \sum_i \sum_k \frac{P_{ik}(t,0)}{\Gamma_k \hbar \omega_i A_{\text{eff}}} \left\{ \exp[\Gamma_k \sigma_{gk}(\eta_k \mathfrak{N} - N_0 z)] - 1 \right\}, \tag{2.14}$$

where

$$\mathfrak{N}_0 = \frac{Iz\tau_{s0}}{qV}.$$

While the input pump signal is modulated harmonically, the input powers can be represented as,

$$P_{1k}(t,0) = \overline{P}_{0,1k} + \Delta P_{0,1k} e^{j\Omega t} + \text{c.c.},$$

$$P_{2k}(t,0) = \overline{P}_{0,2k}, \tag{2.15}$$

25
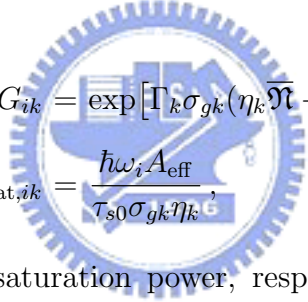
because $P_{2k}(t,0)$ is the CW probe. Assuming $\Delta P_{0,1k} \ll \overline{P}_{0,1k}$, the integrated carrier density, the output probe power, and the output probe phase can be written as,

$$\mathfrak{N}(t,L) = \overline{\mathfrak{N}} + \Delta\mathfrak{N}e^{j\Omega t} + \text{c.c.},$$

$$P_{2k}(t,L) = \overline{P}_{2k} + \Delta P_{2k}e^{j\Omega t} + \text{c.c.}, \tag{2.16}$$

$$\phi_{2k}(t,L) = \overline{\phi}_{2k} + \Delta\phi_{2k}e^{j\Omega t} + \text{c.c.},$$

where L is the length of the SOA. Using Eq. (2.14) and considering only the first-order terms, the small-signal response of the integrated carrier density can be written as,

$$\Delta\mathfrak{N} = -\frac{\displaystyle\sum_k \frac{G_{1k}-1}{\Gamma_k\sigma_{gk}\eta_k P_{\text{sat},1k}}\Delta P_{0,1k}}{j\Omega\tau_{s0} + 1 + \displaystyle\sum_i\sum_k \frac{G_{ik}\overline{P}_{0,ik}}{P_{\text{sat},ik}}}, \tag{2.17}$$

where

$$G_{ik} = \exp\left[\Gamma_k\sigma_{gk}(\eta_k\overline{\mathfrak{N}} - N_0 L)\right],$$

$$P_{\text{sat},ik} = \frac{\hbar\omega_i A_{\text{eff}}}{\tau_{s0}\sigma_{gk}\eta_k},$$

are the bias gain and the saturation power, respectively. Similarly, the small-signal response of the intensity and phase of the probe beam are,

$$\Delta P_{2k} = G_{2k}\overline{P}_{0,2k}\Gamma_k\sigma_{gk}\eta_k\Delta\mathfrak{N}, \tag{2.18}$$

$$\Delta\phi_{2k} = -\frac{\alpha_H}{2}\Gamma_k\sigma_{gk}\eta_k\Delta\mathfrak{N}. \tag{2.19}$$

Since the TE and TM modes of the probe beam interfere at the tunable polarizer which consists of a PC and a polarizer, the relation between the fields before and after the tunable polarizer has to be derived in advance. Using Jone's matrix, the field after the tunable polarizer can derived by,

$$\begin{bmatrix} E_{out} \\ 0 \end{bmatrix} = \underbrace{\begin{bmatrix} 1 & 0 \\ 0 & 0 \end{bmatrix}}_{\text{polarizer}}\underbrace{\begin{bmatrix} e^{j\pi/2} & 0 \\ 0 & e^{-j\pi/2} \end{bmatrix}\begin{bmatrix} \cos\theta_1 & \sin\theta_1 \\ -\sin\theta_1 & \cos\theta_1 \end{bmatrix}}_{\text{half-wave plate}}$$

$$\times \begin{bmatrix} e^{j\pi/4} & 0 \\ 0 & e^{-j\pi/4} \end{bmatrix} \begin{bmatrix} \cos\theta_2 & \sin\theta_2 \\ -\sin\theta_2 & \cos\theta_2 \end{bmatrix} \begin{bmatrix} E_x \\ E_y \end{bmatrix} , \qquad (2.20)$$

$$\underbrace{\phantom{\begin{bmatrix} e^{j\pi/4} & 0 \\ 0 & e^{-j\pi/4} \end{bmatrix} \begin{bmatrix} \cos\theta_2 & \sin\theta_2 \\ -\sin\theta_2 & \cos\theta_2 \end{bmatrix}}}_{\text{quarter-wave plate}}$$

where E_x and E_y are the input field at orthogonal modes, and θ_1 and θ_2 are the angles of the half-wave and quarter-wave plates, respectively. Accordingly, the output field is,

$$E_{out} = e^{j\frac{3\pi}{4}} \left[(\cos\theta_1 \cos\theta_2 + j\sin\theta_1 \sin\theta_2)E_x \right.$$

$$\left. + (\cos\theta_1 \sin\theta_2 - j\sin\theta_1 \cos\theta_2)E_y \right] . \qquad (2.21)$$

Owing to

$$|(\cos\theta_1 \cos\theta_2 + j\sin\theta_1 \sin\theta_2)|^2 + |(\cos\theta_1 \sin\theta_2 - j\sin\theta_1 \cos\theta_2)|^2 = 1 ,$$

Eq. (2.21) can be simplified by defining,

$$(\cos\theta_1 \cos\theta_2 + j\sin\theta_1 \sin\theta_2)E_x = \cos\theta \cdot e^{j\vartheta_x} |E_x| ,$$

$$(\cos\theta_1 \sin\theta_2 - j\sin\theta_1 \cos\theta_2)E_y = -\sin\theta \cdot e^{j\vartheta_y} |E_y| . \qquad (2.22)$$

Since θ and $\vartheta_y - \vartheta_x$ are the functions of two variables, θ_1 and θ_2, they could be adjusted independently. If E_x and E_y correspond to the TE and TM modes of the probe beam, the power of the probe beam after the tunable polarizer can be represented as,

$$P_{TP}(t, L) = \frac{1}{2} \left| \cos\theta \sqrt{P_{2e}(t, L)} - \sin\theta \sqrt{P_{2m}(t, L)} \cdot e^{j(\vartheta + \Delta\phi)} \right|^2 , \qquad (2.23)$$

where $\vartheta_y - \vartheta_x = \vartheta + \Delta\phi$, and $\Delta\phi = \Delta\phi_{2m} - \Delta\phi_{2e}$ is the phase difference between TE and TM modes. In order to obtain maximum ER after the interference, θ needs to be chosen to make sure that the TE ad TM modes beyond the polarizer have equal DC intensity, i.e., $\cos^2\theta \cdot \overline{P}_{2e} = \sin^2\theta \cdot \overline{P}_{2m} = P_\theta$, and the selection of ϑ is to ensure that $P_{TP}^2(t, L)$ has a minimum zero level. For example, $\vartheta + \Delta\phi_{\text{off}} = 0$ should be applied for the non-inverting

operation, where $\Delta\phi_{\text{off}}$ is the phase difference when the input pump signal is logical zero. Thus, under this condition, the small-signal response of XPoM, ΔP_{TP}, given by Eq. (2.23) could be written as,

$$\Delta P_{TP} = \frac{1}{2}(1 - \cos\vartheta)\left(\cos^2\theta \cdot \Delta P_{2e} + \sin^2\theta \cdot \Delta P_{2m}\right) + P_\theta \sin\vartheta \cdot \Delta\phi. \qquad (2.24)$$

The first and second terms of the right hand side of Eq. (2.24) are associated with XGM and XPM effects, respectively. From Eq. (2.19), if there is no polarization dependent gain, i.e. $\Delta\phi_{2m} = \Delta\phi_{2e}$, the remaining contribution of Eq. (2.24) is only the XGM effect. By defining the lifetimes of stimulated recombination due to the pump and probe beams as,

$$\frac{1}{\tau_{\text{stim},i}} \equiv \sum_k \frac{G_{ik}\overline{P}_{0,1k}}{\tau_{s0}P_{\text{sat},ik}}, \qquad (2.25)$$

Eqs. (2.17)-(2.19), (2.24) and (2.25) yield,

$$\Delta P_{TP} = \frac{[\chi(1 + r_{me}) - (1 - r_{me})]\dfrac{\alpha_H \sin\vartheta}{2\tau_{s0}}\displaystyle\sum_k\left[\dfrac{\Gamma_e\sigma_{ge}\eta_e P_\theta}{\Gamma_k\sigma_{gk}\eta_k P_{\text{sat},1k}}(G_{1k} - 1)\Delta P_{0,1k}\right]}{j\Omega + \dfrac{1}{\tau_{s0}} + \dfrac{1}{\tau_{\text{stim},1}} + \dfrac{1}{\tau_{\text{stim},2}}}, \qquad (2.26)$$

where

$$\chi = -\frac{1}{\alpha_H}\tan\frac{\vartheta}{2},$$

$$r_{me} = \frac{\Gamma_m\sigma_{gm}\eta_m}{\Gamma_e\sigma_{ge}\eta_e},$$

are the factors associated to the operating point and the polarization dependence of an SOA. Restated, the first and second terms in the first bracket of Eq. (2.26) represent the contributions from XGM and XPM effects, respectively. Moreover, the ratio of XGM to XPM parts contributing to the output small-signal response can be written as $\chi(1 + r_{me})/(1 - r_{me})$. $\chi < 0$ implies that the XPM and XGM effects have the same logic. However, XPM effect dominates the XPoM generally. Therefore, $\chi > 0$ and

$\chi < 0$ represent that XPoM works with non-inverted and inverted conversion scheme, respectively.

Furthermore, from Eqs. (2.17) and (2.18), the small-signal response of XGM is,

$$\sum_k \Delta P_{2k} = \frac{-\dfrac{1}{\tau_{s0}} \displaystyle\sum_k \sum_{k'} \dfrac{\Gamma_k \sigma_{gk} \eta_k \overline{P}_{2k}}{\Gamma_{k'} \sigma_{gk'} \eta_{k'} P_{\text{sat},1k'}} \left(G_{1k'} - 1\right) \Delta P_{0,1k'}}{j\Omega + \dfrac{1}{\tau_{s0}} + \dfrac{1}{\tau_{\text{stim},1}} + \dfrac{1}{\tau_{\text{stim},2}}} . \tag{2.27}$$

It is evident from Eqs. (2.26) and (2.27) that the modulation bandwidths of XPoM and XGM are the same and both are limited by the carrier's recovery time.

2.4.2 Small-signal model of DXPoM

In this section, the analytical small-signal response of DXPoM is carried out to explain the relations between conversion performance and various operating parameters. If the delay time, Δt, is added on TM modes, the intensity and phase responses of TM mode described in Eqs. (2.18) and (2.19) would become:

$$\Delta P_{2k} = G_{2k} \overline{P}_{0,2k} \Gamma_k \sigma_{gk} \eta_k \Delta \mathfrak{N} \cdot e^{-j\Omega \Delta t}, \tag{2.28}$$

$$\Delta \phi_{2k} = -\frac{\alpha_H}{2} \Gamma_k \sigma_{gk} \eta_k \Delta \mathfrak{N} \cdot e^{-j\Omega \Delta t}. \tag{2.29}$$

Using Eqs. (2.24), (2.28) and (2.29), the small-signal response of DXPoM is,

$$\Delta P_{TP} = \frac{\chi \left(1 + r_{me} e^{-j\Omega \Delta t}\right) - \left(1 - r_{me} e^{-j\Omega \Delta t}\right)}{j\Omega + \dfrac{1}{\tau_{s0}} + \dfrac{1}{\tau_{\text{stim},1}} + \dfrac{1}{\tau_{\text{stim},2}}}$$
$$\times \frac{\alpha_H \sin \vartheta}{2\tau_{s0}} \sum_k \left[\frac{\Gamma_e \sigma_{ge} \eta_e P_\theta}{\Gamma_k \sigma_{gk} \eta_k P_{\text{sat},1k}} \left(G_{1k} - 1\right) \Delta P_{0,1k} \right]. \tag{2.30}$$

It is clear that the modulation bandwidth is determined by the first part in Eq. (2.30). Therefore, by dividing this part by $(\chi - 1)\tau_T$, it can be difined as a transfer function, $T(\Omega)$,

$$T(\Omega) = \frac{1 - \gamma_\chi e^{-j\Omega \Delta t}}{1 + j\Omega \tau_T}, \tag{2.31}$$

where

$$\frac{1}{\tau_T} = \frac{1}{\tau_{s0}} + \frac{1}{\tau_{\text{stim},1}} + \frac{1}{\tau_{\text{stim},2}} \, ,$$

$$\gamma_\chi = r_{me} \frac{1 + \chi}{1 - \chi} \, .$$

Unfortunately, in Eq. (2.31), the analytical expression of 3-dB bandwidth cannot be obtained after the time delay, Δt, is applied. Therefore, as shown in Fig. 2.13, several numerical examples are given to illustrate the substantial improvement of the conversion bandwidth. With $\tau_T = 5 \times 10^{-11}\,\text{s}$ and $\gamma_\chi = 0.8$, the 3-dB bandwidths of XPoM and DXPoM under 2.5, 5, 10, 20, and 40 ps delay are 5.5, 7.0, 69.9, 67.3, 38.4, and 41.3 GHz, respectively. With proper delay, the conversion bandwidth can be improved by more than 1000%.

When Δt is smaller than zero, the TM mode will get ahead of the TE mode and the DXPoM is operated with TE delay. By defining $T(\Omega) = |T(\Omega)| \exp(j\Theta(\Omega))$, the group delay of the transfer function is $-\mathrm{d}\Theta/\mathrm{d}\Omega$. With the same operating parameters, the conversion bandwidth and the group delay of the TE and TM delay are shown in Fig. 2.14. Although the amplitude responses of DXPoM with TM and TE delay are identical, the TE delay has the largest phase variation, which will induce to the worst timing delay disparity and will cause the biggest converted signal distortion compared with XPoM or DXPoM with TM delay. Actually, the same conclusions are reached in large-signal simulation as well, as shown in Figs. 2.6 and 2.7. Compared with XPoM, DXPoM with TM delay has better conversion bandwidth and lower timing jitter due to flatter delay response. In order to portray the effects of phase response to the signal distortion, the PRBS input signal spectrum is directly multiplied by the transfer functions shown in Fig. 2.14 and the results of XPoM, DXPoM with TM delay and DXPoM with TE delay are illustrated in Figs. 2.15(a)-(c), respectively, after inverse Fourier transform
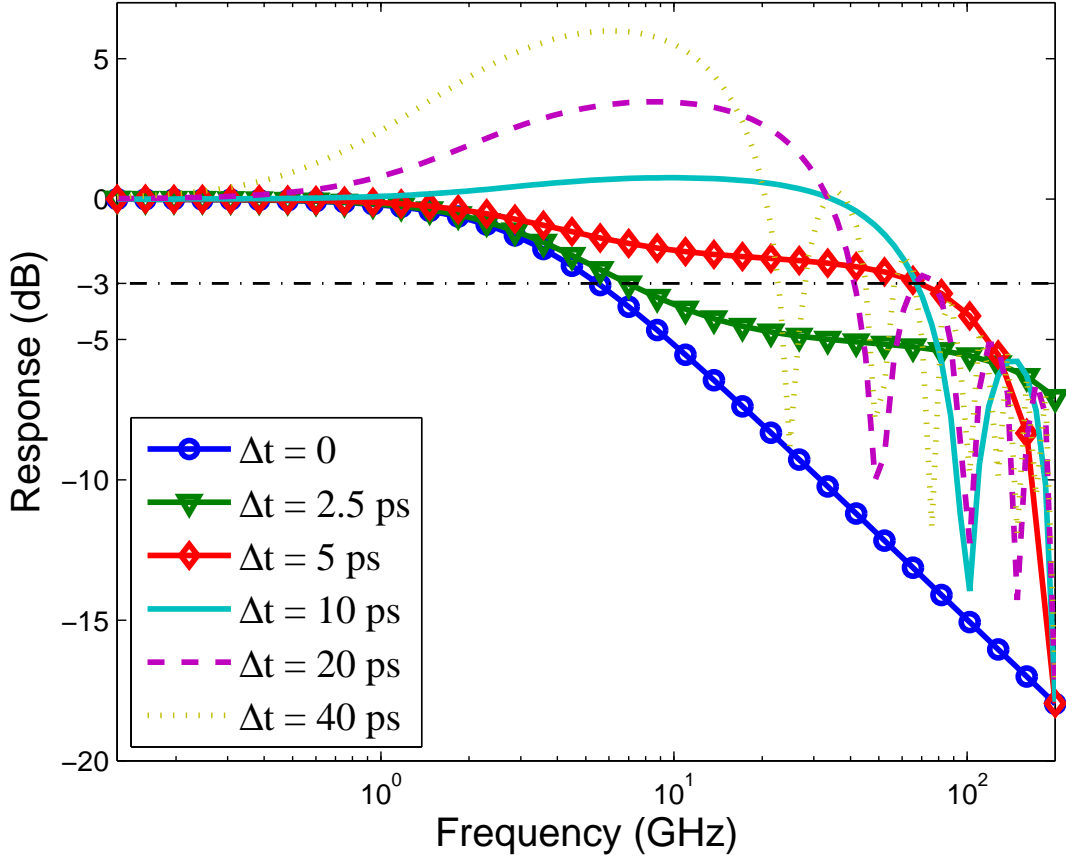
Figure 2.13: Frequency response of XPoM and DPoM with different delay time

back to time domain. One can clearly see the eye closure with TE delay due to the worse

phase response.

Furthermore, normalizing Ω and Δt by τ_T, Eq. (2.31) can be re-written as,

$$T'(\Omega') = \frac{1}{1 - \gamma_\chi} \times \frac{1 - \gamma_\chi e^{-j\Omega'\Delta t'}}{1 + j\Omega'}, \qquad (2.32)$$

where T', Ω' and $\Delta t'$ are the normalized transfer function, angular frequency and delay

time, respectively. Thus, γ_χ is the only variable which will affect the conversion bandwidth

under different normalized delay times. Figure 2.16 illustrates the relationships between

normalized 3 dB conversion bandwidth and time delay under different γ_χ. The maximum

bandwidth improvement is obtained with a shorter normalized delay time as γ_χ closer to

1. If γ_χ is lesser than zero, such as -1 in Fig. 2.16, the XGM effect will be the dominating
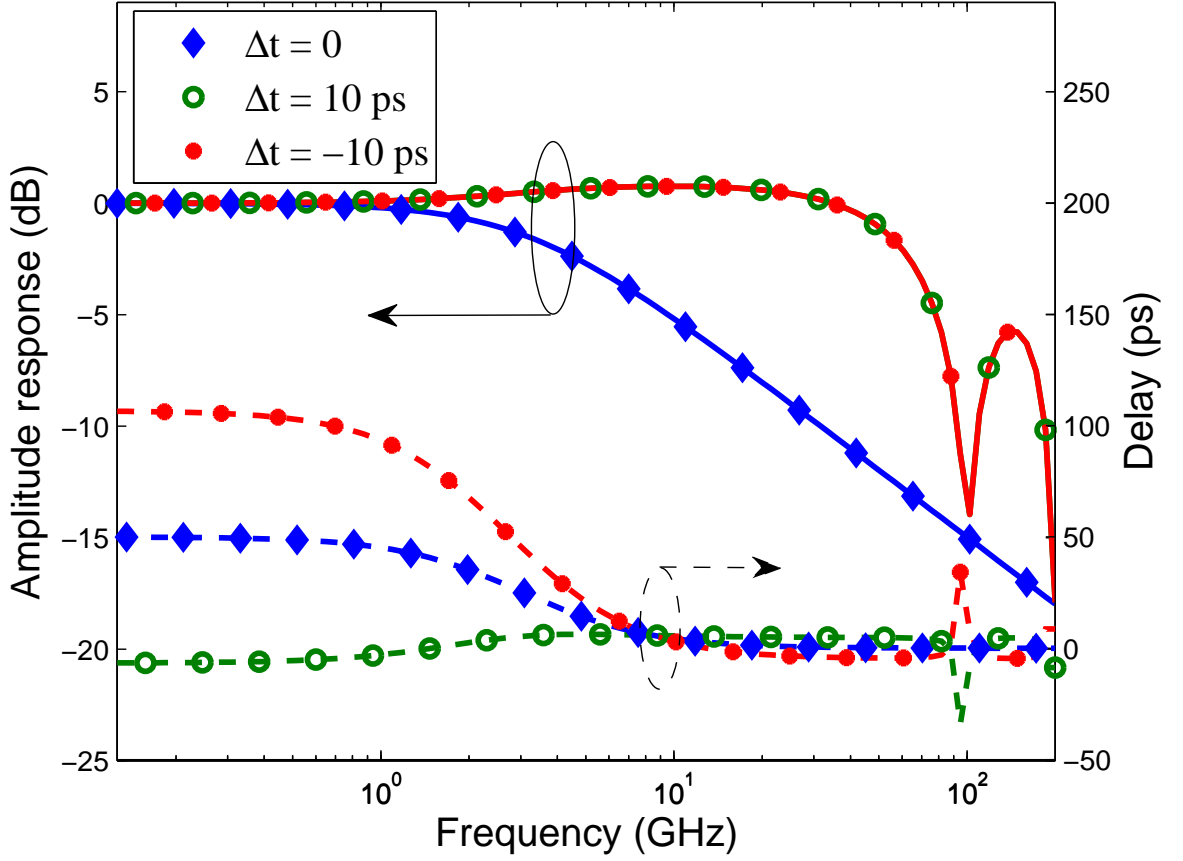
Figure 2.14: Amplitude (solid curves) and delay (dashed curves) responses of XPoM, DXPoM with TM delay and DXPoM with TE delay

factor of the bandwidth, and the bandwidth will be decreased with any extra birefringence delay.

Accordingly, the conversion performance is determined by not only the bandwidth of amplitude response but also the flatness of group delay from phase response. In other words, for a transfer function, the flat and large pass band and the linear phase response corresponding to $|T'(\Omega')|$ and $\Theta'(\Omega')$, respectively, are required. For example, the DX-PoM with TM and TE delay have the same bandwidth improvement but they perform differently due to the unlike group delays. Therefore, the delay response with $\Delta t'$ corresponding to the largest modulation bandwidth in Fig. 2.16 is worth discussing. Setting
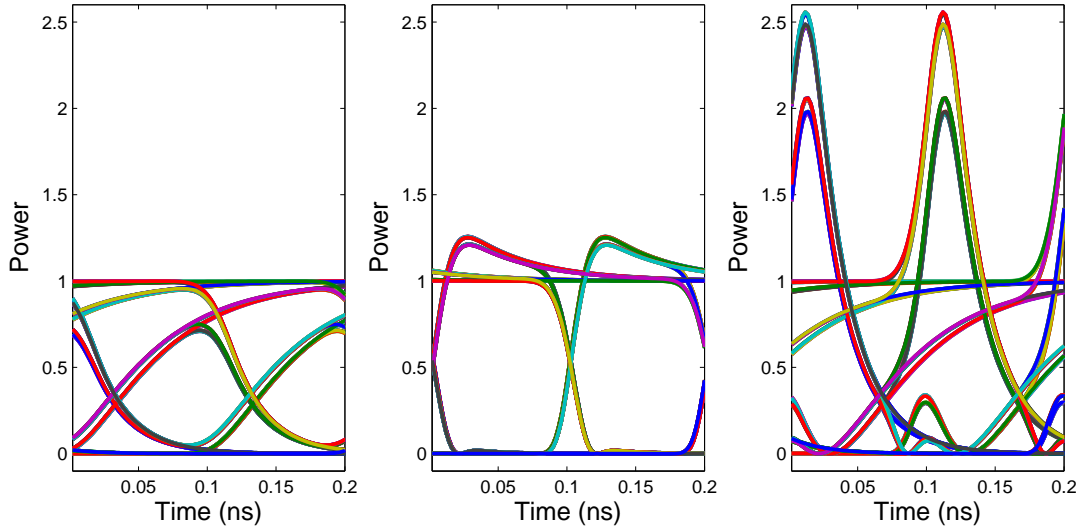
Figure 2.15: Simulated eye-diagrams derived from the transfer functions of small-signal model based on (a) XPoM, (b) DXPoM with TM delay, and (c) DXPoM with TE delay

$s = j\Omega'$ in the normalized transfer function in Eq. (2.32), the transfer function becomes,

$$H(s) = \frac{1}{1 - \gamma_\chi} \times \frac{1 - \gamma_\chi e^{-s\Delta t'}}{1 + s} . \tag{2.33}$$

Then, $T'(\Omega')$ can be derived by evaluating $H(s)$ on the imaginary axis in the complex s plane. The poles and zeros of Eq. (2.33) are $p_H = -1, -\infty + j2n\pi/\Delta t'$ and $z_H = \ln\gamma_\chi/\Delta t' + j2n\pi/\Delta t'$, respectively, where n are all integrals. When all poles of a causal system are in the left half of the s plane, this system is stable. If all zeros are also in the left half of the s plane simultaneously, this system is said to be a minimum phase system (MPS) [43]. An important property of MPS is that $\Theta'(\Omega')$ can be got by applying Hilbert transform to $\ln|T'(\Omega')|$. If $\Delta t'$ is positive and γ_χ lies in between 0 and 1 which correspond to the condition of DXPoM with TM delay, the whole zeros of Eq. (2.33) are in the left half of the s plane. Namely, DXPoM with TM delay is an MPS and its amplitude and phase responses are not independent. It has been shown that a constant logarithmic amplitude response implies linear phase response as they are a Hilbert transform pair [43]. From Fig. 2.13, when Δt is enlarged to get a larger bandwidth gradually, the pass band
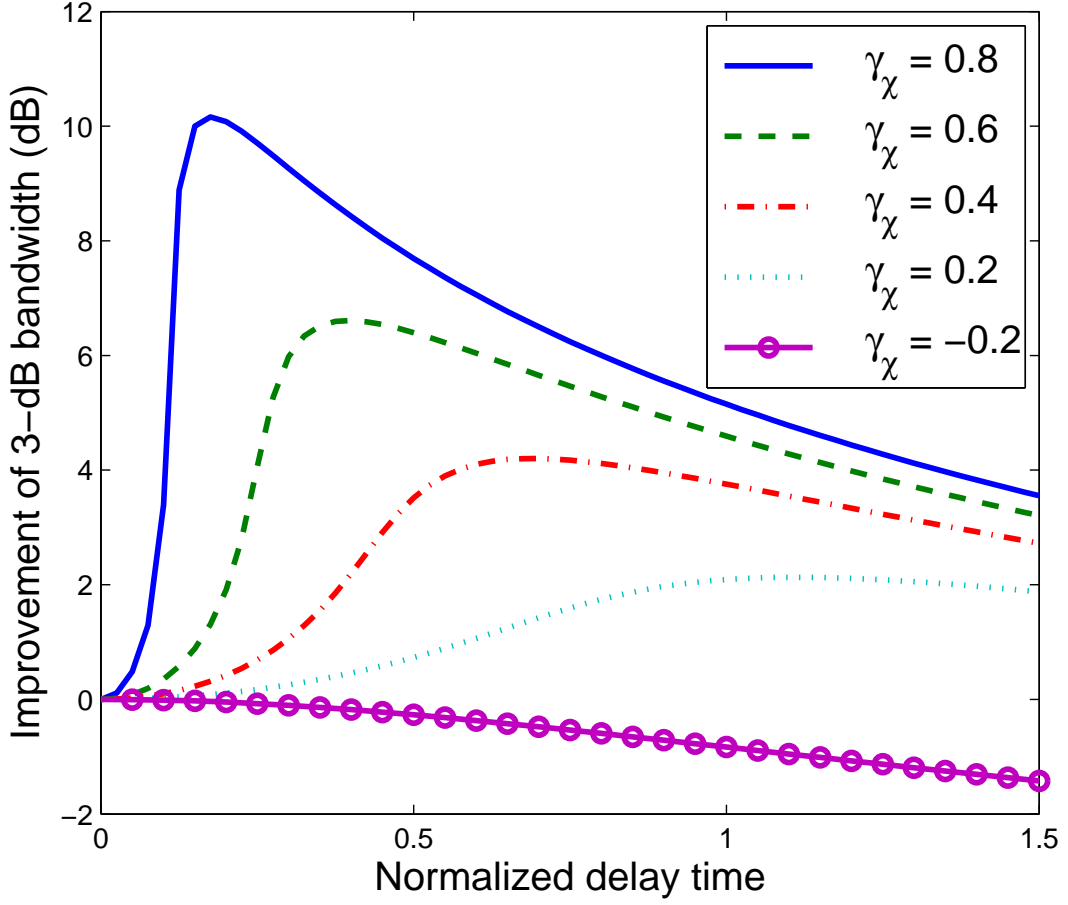
Figure 2.16: Improvement of 3-dB bandwidth with different γ_χ

is getting flatter until the largest bandwidth is approximately achieved. Consequently, relying on the properties of MPS and Hilbert transform, when Δt is selected to get the largest bandwidth, the delay response is almost constant in the pass band and the best performance of DXPoM with TM delay is obtained simultaneously. Using second-order approximation and forcing $|T'(\Omega')| = 1$, yield the optimum delay,

$$\Delta t'_{opt} = \frac{1 - \gamma_\chi}{\sqrt{\gamma_\chi}}, \tag{2.34}$$

which corresponds to simultaneous a flat amplitude response and a linear phase response. Figure 2.17 plots the amplitude and delay responses with delays of $\Delta t'_{opt}$, $0.95 \times \Delta t'_{opt}$ and $1.05 \times \Delta t'_{opt}$. The dotted curves in Fig. 2.17 represent the second-order approxima-

tions of the amplitude responses. The good match at low frequency indicates that this approximation can be applied to determine the optimum delay. Furthermore, a nearly constant delay response and the flattest amplitude response are achieved simultaneously by applying $\Delta t'_{opt}$.
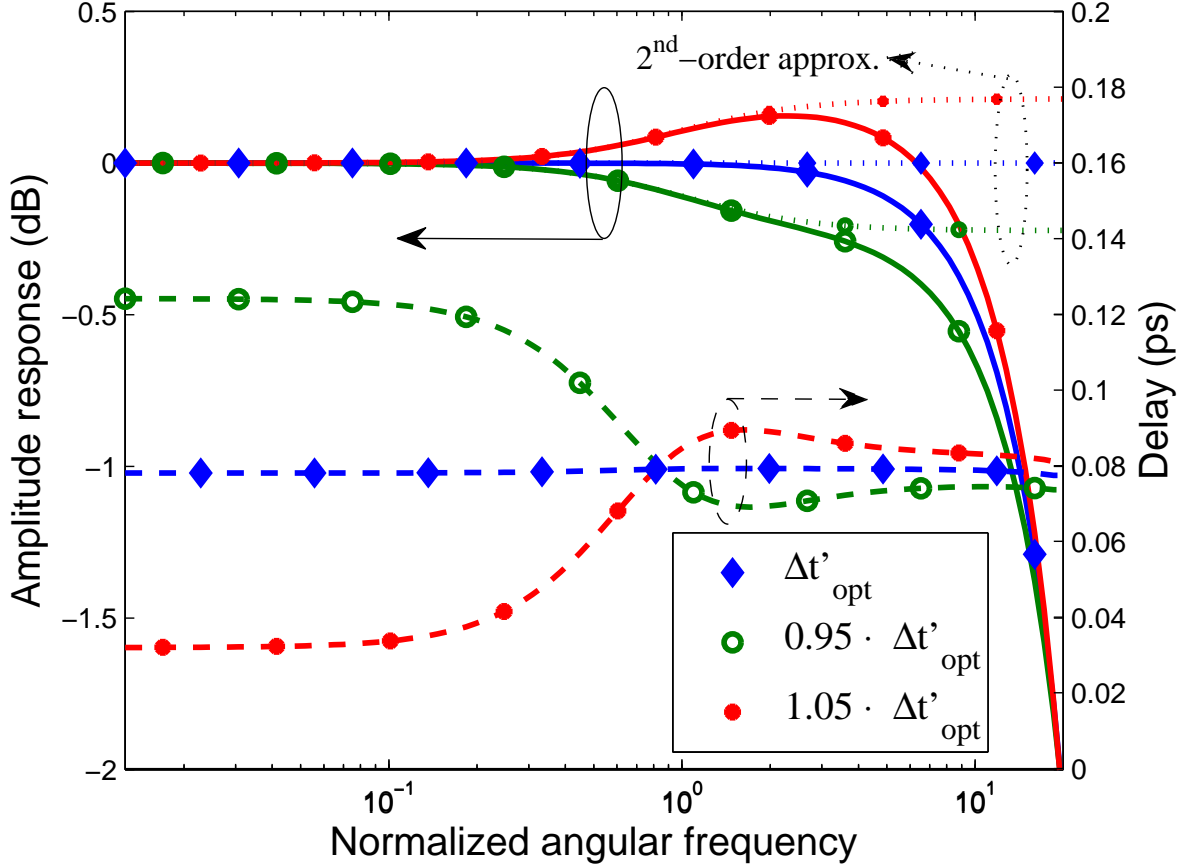
Figure 2.17: Amplitude (solid curves) and delay (dashed curves) responses with delays of $\Delta t'_{opt}$, $0.95 \times \Delta t'_{opt}$ and $1.05 \times \Delta t'_{opt}$

The information concerning the time domain can be obtained from the impulse response, which is the inverse Fourier transform of the frequency response of the small-signal model. Taking inverse Fourier transform of Eq. (2.32), the impulse response is,

$$h(t') = \mathfrak{F}^{-1}\left\{T'(\Omega')\right\} = \frac{\sqrt{2\pi}}{1 - \gamma_\chi}\left[e^{-t'}u_s(t') - \gamma_\chi \cdot e^{-(t'-\Delta t')}u_s(t' - \Delta t')\right], \quad (2.35)$$

where $u_s(t) = \int_{-\infty}^{t} \delta(x)\,\mathrm{d}x$ is the unit step function and t' is the normalized time frame.

Figure 2.18 illustrates several impulse responses with different γ_χ and $\Delta t'$. Fig. 2.18(a) is XPoM without an extra delay, and Fig. 2.18(b) is DXPoM with the TM delay of 0.35. It's obvious that Fig. 2.18(b) has narrower impulse response due to the extra delay canceling the relaxation tail. However, increasing the extra delay may enlarge the response time, as shown in Fig. 2.18(c), which is still better than Fig. 2.18(a). This also explains the change of the bandwidths in Fig. 2.13. While γ_χ is closer to 1, as shown in Fig. 2.18(d), smaller time delay is needed to reach the maximum bandwidth which comes to the same conclusion as in Fig. 2.16. Furthermore, with negative γ_χ as in Fig. 2.18(e), the impulse response is distorted by the extra time delay and causes the bandwidth decrease as depicted in Fig. 2.16. Lastly, Fig. 2.18(f) plots the the case with TE delay. Although the TE delay and the TM delay perform the same bandwidth, as shown in Fig. 2.14, due to distinct phase performance, the impulse responses of Figs. 2.18(b) and (f) are so different that the TE delay couldn't improve the conversion performances.
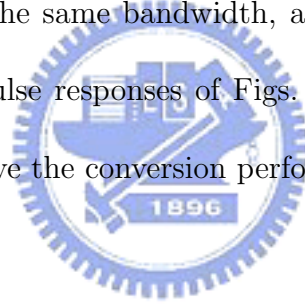
2.4.3 Discussion

From the small-signal model, the optimized delay is a constant, if the operation conditions are fixed, such as the injection current, the injection powers, the SOP of both the pump and probe beams, and the tunable polarizer. Namely, once the operation conditions are selected to maximize the conversion bandwidth, the desired delay is irrelative to the bit rate of incoming signals. However, the remote pump beam could be arbitrarily polarized after transmitting through fibers, and the SOP could vary significantly in time periods of about 1 ms [44]. Therefore, a polarization stabilizer is required to realize and optimize DXPoM in practice. Actually, both XPoM and DXPoM need the automatic polarization controlling.

(a)

$\gamma_{\chi} = 0.6, \quad \Delta t' = 0$

(b)

$\gamma_{\chi} = 0.6, \quad \Delta t' = 0.35$

(c)

$\gamma_{\chi} = 0.6, \quad \Delta t' = 0.7$

(d)

$\gamma_{\chi} = 0.8, \quad \Delta t' = 0.15$

(e)

$\gamma_{\chi} = -0.4, \quad \Delta t' = 0.35$

(f)

$\gamma_{\chi} = 0.6, \quad \Delta t' = -0.35$
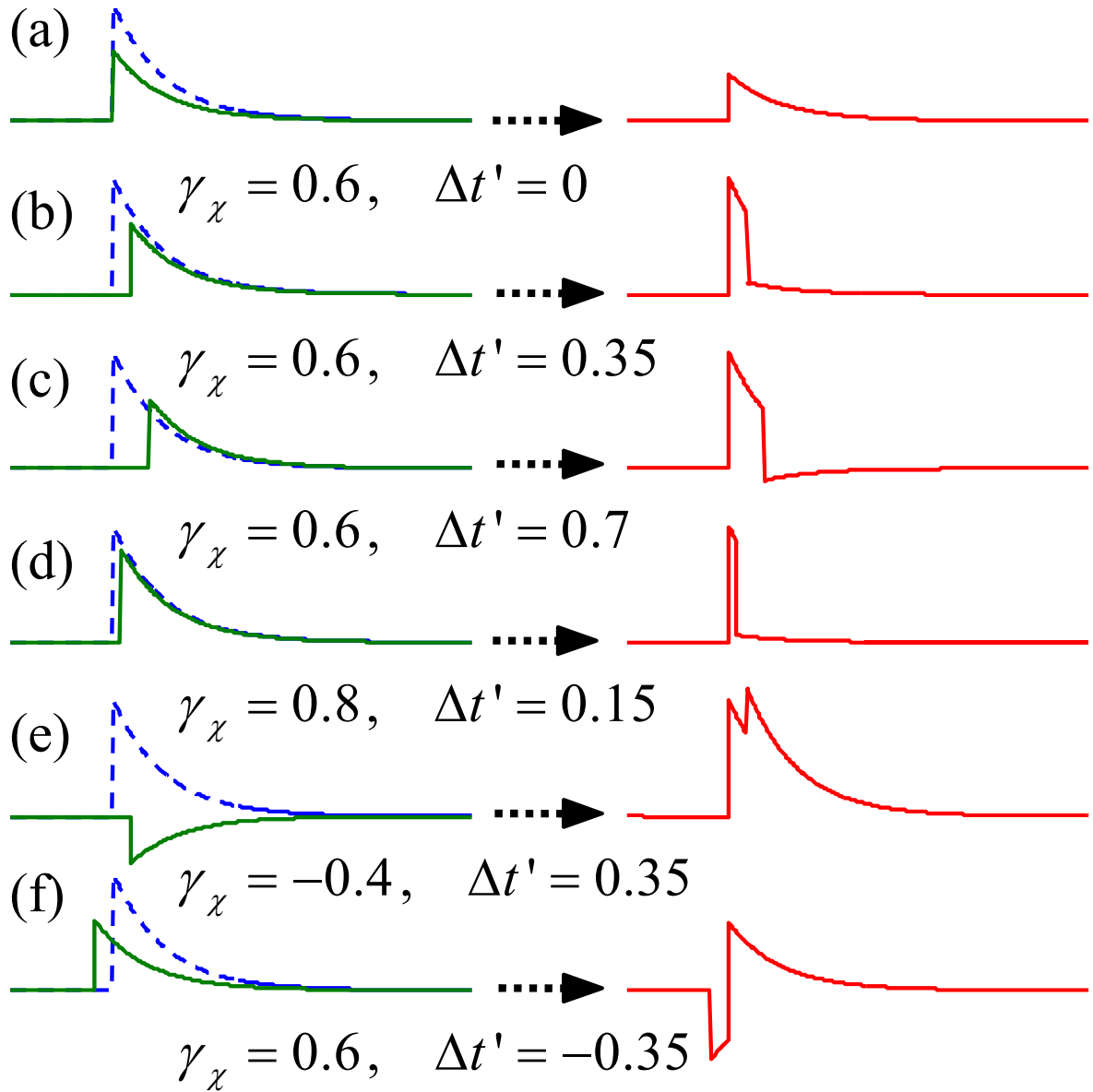
Figure 2.18: Impulse responses of small-signal model in different conditions

Chapter 3

All-optical OOK-to-PSK conversion

3.1 Introduction to the OOK and DPSK formats

Considering both transmitter and receiver, the OOK format, which carries binary data by turning on and off the optical power, is the simplest format to be carried out. At the transmitter side, besides using an external modulator, such as a LiNbO$_3$ Mach-Zehnder modulator (LN-MZM) or an electro-absorption modulator (EAM), even a direct modulation laser can be adopted to generate OOK signals economically. On the receiver side, only an optical detector with suitable bandwidth is needed. However, as transmission distance increases and channel spacings in WDM systems decrease, the conventional OOK format is not suitable for all the application anymore. Accordingly, various modulation formats which show different benefits, such as higher dispersion tolerance, lower sensitivity, higher nonlinear tolerance, and higher spectral efficiency, have been proposed [23]. Actually, the coherently detected BPSK format had attracted a lot of attention before the successful introduction of Erbium doped fiber amplifiers (EDFA). To avoid the requirement of phase-lock loops (PLL) in coherent BPSK receivers, the DPSK format carries information by differential phase between two neighboring pulses. The transmitter of DPSK signals is almost identical to that of BPSK signals, but the self interference of DPSK signals by a DI makes its receiver to be implemented much easier. Figure 3.1(a) shows the transmitter of the DPSK format. To avoid error propagation at the receiver, an electrical precoder is required. At the receiver, shown by Fig. 3.1(b), the DPSK signal interferes with its delay

version through a DI, and therefore, the phase modulated signal is converted to two intensity modulated signals, alternate-mark inversion (AMI) and duobinary (DB), which can be detected by optical detectors. While balanced detectors are used, $\sim$ 3-dB sensitivity improvement can be obtained, compared with the OOK format. This improvement could be observed from the constellation diagrams of the OOK and DPSK formats. Considering the same average power, the peak power of the DPSK format is lower than that of the OOK format, but the distance between two symbols of the DPSK format is $\sqrt{2}$ times of that of the OOK format, as shown in Fig. 3.2.
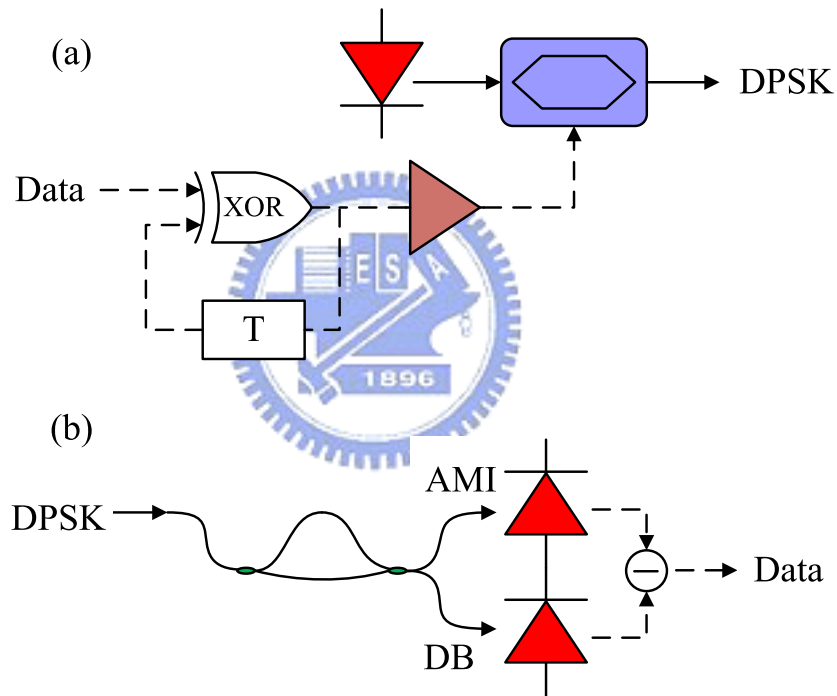
Figure 3.1: (a) The transmitter and (b) receiver of the DPSK format
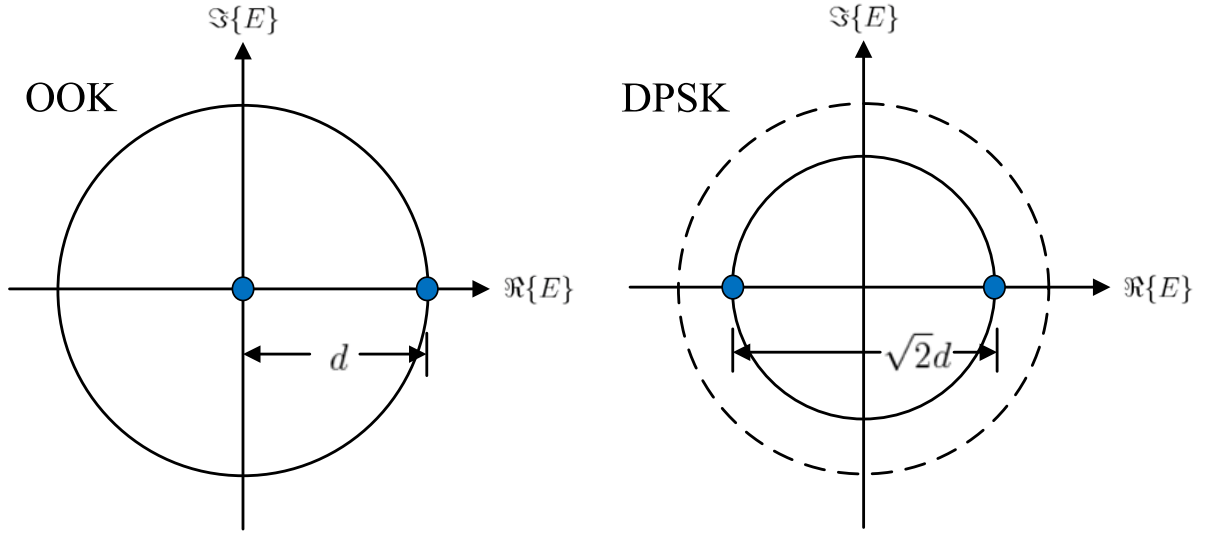
Figure 3.2: Constellation diagrams of the OOK and DPSK formats

3.2 Polarization-insensitive OOK-to-DPSK conversion

3.2.1 Concept of XPM-based format conversion

It is straightforward that the XPM effect in a nonlinear medium can convert the amplitude information of an OOK pump beam to the phase of another probe beam all-optically. As shown in Fig. 3.3, while the space of the OOK signal only induces negligible nonlinear phase shift to the probe beam, the mark with specific power is supposed to generate π phase shift to encode binary data on the phase of the probe beam. Actually, this converted phase-modulated signal is not really a DPSK signal, because its received binary data after being demodulated by a DI are not the same to the original OOK signal. That is, similar to Fig. 3.1(a), the binary data of the OOK signal have to be precoded to realize OOK-to-DPSK conversion, and this is doable in electrical domain before generating OOK signals. Therefore, the issue about precoding will not be addressed in this chapter. Moreover, all the phase-modulated signals converted from OOK signals in this chapter will be treated as DPSK signals and be evaluated by using self interference in a DI in

40

both theoretical discussion and experimental realization. As to the BER measurement in the experiment, the precoder does not matter, since the differential code of PRBS is still the original PRBS.
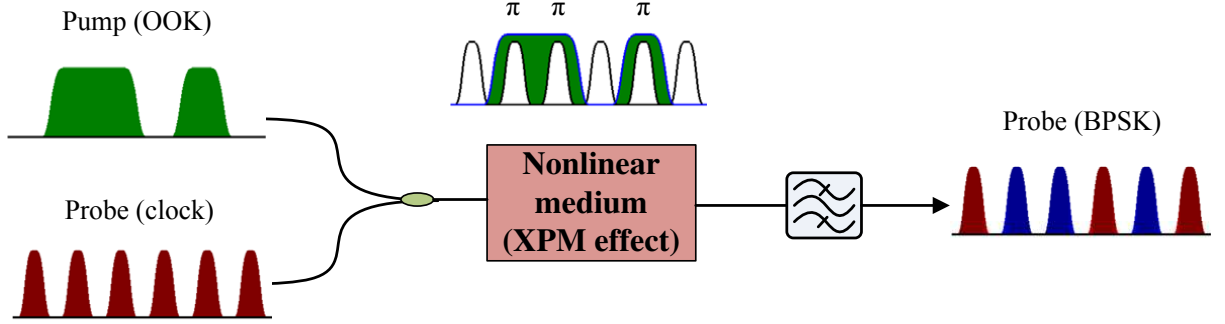
Figure 3.3: Schematic OOK-to-BPSK format conversion

3.2.2 XPM effect in a birefringent fiber

Although a compact SOA is an attractive nonlinear medium due to its high nonlinearity and polarization insensitivity, its slow response ($\sim 10^2$ ps) and residual amplitude modulation make high-speed format conversion difficult to be implemented. In contrast, the XPM effect in an HNLF is much faster ($\sim$ fs), but unfortunately, it is polarization sensitive [45]. Recently, novel PCF has been shown to have not only high birefringence, but also fixed birefringent axes over the entire fiber [7]. While the pump power is launched equally to both birefringent axes of PCF, the pump-induced XPM effect could be independent on the state of polarization (SOP) of another probe beam [7]. However, in an OOK-to-BPSK format converter, the SOP of the pump beam is not fixed, and only the SOP of local probe beam is controllable. Although polarization-independent XPM effect cannot be achieved by only controlling the SOP of the probe beam, launching the probe at 45° relative to the birefringent axes can make the XPM effect less sensitive to the uncontrollable SOP of the pump.

41

To investigate this polarization-insensitive XPM effect, by assuming $\chi_{xxyy}^{(3)} = \chi_{xyxy}^{(3)} = \chi_{xyyx}^{(3)} = \chi_{xxxx}^{(3)}/3$, the third order nonlinear effect in a linearly birefringent fiber can be described by the nonlinear Schrödinger (NLS) equations [45],

$$
\begin{aligned}
&\frac{\partial A_{ix}}{\partial z} + \frac{1}{v_{gix}}\frac{\partial A_{ix}}{\partial t} + j\frac{\beta_i''}{2}\frac{\partial^2 A_{ix}}{\partial t^2} + \frac{\alpha_i}{2}A_{ix} \\
&= j\gamma\left(|A_{ix}|^2 + 2|A_{jx}|^2 + \frac{2}{3}|A_{iy}|^2 + \frac{2}{3}|A_{jy}|^2\right)A_{ix} + \frac{j\gamma}{3}A_{ix}^* A_{iy}^2 e^{-j2\Delta\beta_i z} \\
&\quad + \frac{j2\gamma}{3}A_{jx}^* A_{jy}A_{iy}e^{-j(\Delta\beta_i + \Delta\beta_j)z} + \frac{j2\gamma}{3}A_{jx}A_{jy}^* A_{iy}e^{-j(\Delta\beta_i - \Delta\beta_j)z} ,
\end{aligned} \tag{3.1}
$$

$$
\begin{aligned}
&\frac{\partial A_{iy}}{\partial z} + \frac{1}{v_{gix}}\frac{\partial A_{iy}}{\partial t} + j\frac{\beta_i''}{2}\frac{\partial^2 A_{iy}}{\partial t^2} + \frac{\alpha_i}{2}A_{iy} \\
&= j\gamma\left(|A_{iy}|^2 + 2|A_{jy}|^2 + \frac{2}{3}|A_{ix}|^2 + \frac{2}{3}|A_{jx}|^2\right)A_{iy} + \frac{j\gamma}{3}A_{iy}^* A_{ix}^2 e^{+j2\Delta\beta_i z} \\
&\quad + \frac{j2\gamma}{3}A_{jy}^* A_{jx}A_{ix}e^{+j(\Delta\beta_i + \Delta\beta_j)z} + \frac{j2\gamma}{3}A_{jy}A_{jx}^* A_{ix}e^{+j(\Delta\beta_i - \Delta\beta_j)z} ,
\end{aligned} \tag{3.2}
$$

where the subscripts $i = 1$, 2 and $j = 1$, 2 such that $i \neq j$ indicate the pump (i or $j = 1$) or probe (i or $j = 2$); the subscripts x and y represent two birefringent axes of a fiber; A is the electrical field; v_g is the group velocity; β'' is the group-velocity dispersion (GVD) parameter; α is the fiber loss; γ is the nonlinear coefficient, and $\Delta\beta = \beta_x - \beta_y$ is the wave-vector mismatch due to linear birefringence. To avoid unnecessary chirping, the pulse width of the OOK is normally wider than that of the probe beam. Moreover, while the probe beam is a clock pulse train, its launch power has to be low to reduce the SPM effect. Therefore, the nonlinear effects induced by the probe beam and the rising (or falling) edges of the pump beam can be neglected. To further simplify the NLS equations, the last tree terms of Eqs. (3.1)-(3.2) can be assumed to be negligible, due to their fast oscillating exponential terms. To fulfill this assumption, not only large birefringence of the fiber, but also enough pump-probe detuning (PPD, $|\lambda_1 - \lambda_2|$) are required. In other words, these conditions can make $|\Delta\beta_1 + \Delta\beta_2|L \gg 2\pi$ and $|\Delta\beta_1 - \Delta\beta_2|L \gg 2\pi$, where L is the fiber length. After neglecting the loss and dispersion of the fiber, and using the

retarded time frame, the NLS equations of the probe could be simplified as,

$$\frac{\mathrm{d}A_{2x}}{\mathrm{d}z} = j2\gamma\Big(|A_{1x}|^2 + \frac{1}{3}|A_{1y}|^2\Big)A_{2x}\,, \tag{3.3}$$

$$\frac{\mathrm{d}A_{2y}}{\mathrm{d}z} = j2\gamma\Big(|A_{1y}|^2 + \frac{1}{3}|A_{1x}|^2\Big)A_{2y}\,. \tag{3.4}$$

While $A_1(z=0) = \sqrt{P_1\cos^2\psi_1}\,e^{j\theta_{1x}}\hat{\mathbf{x}} + \sqrt{P_1\sin^2\psi_1}\,e^{j\theta_{1y}}\hat{\mathbf{y}}$, where P_1 is the launched pump power, and ψ_1 ($\in [0, \pi/2]$) and θ_1 determine the SOP of the launched pump beam, the solutions to Eqs. (3.3)-(3.4) are,

$$A_{2x}(L) = A_{2x}(0)\exp\Big[j2\gamma P_1\Big(\frac{2\cos^2\psi_1+1}{3}\Big)L\Big]\,, \tag{3.5}$$

$$A_{2y}(L) = A_{2y}(0)\exp\Big[j2\gamma P_1\Big(\frac{2\sin^2\psi_1+1}{3}\Big)L\Big]\,. \tag{3.6}$$

Owing to $\cos^2\psi_1 + \sin^2\psi_1 = 1$, the phase shifts of A_{2x} and A_{2y} could be the same ($\psi_1 = \pi/4$) or extremely different ($\psi_1 = 0$ or π). Since ψ_1 is uncontrollable, as the probe is launched at one axis (i.e. $A_{2x}(0)$ or $A_{2y}(0) = 0$), the worse scenario will happen and the nonlinear phase shift can change from maximum to minimum according to ψ_1. In contrast, by setting $|A_{2x}(0)| = |A_{2y}(0)|$, half the probe beam will have larger phase shift, when the other half has lower phase shift. Hence, the phase shift variation caused by variable SOP of the pump could be reduced by launching the probe at 45° relative to the birefringent axes.

3.2.3 PPD-dependent XPM effect

From the earlier work [46], the first and second exponential terms of Eqs. (3.1)-(3.2) could be neglected without considering PPD for the commercial PCF (NL·1550·NEG·1 by Crystal Fibre A/S) with tens of meters. However, the last terms of Eq. (3.1)-(3.2) would seriously dependent on PPD, and $\Delta\beta_1 - \Delta\beta_2$ of the commercial PCF can be fitted

empirically as [46],

$$\Delta B = \Delta\beta_1 - \Delta\beta_2 = 1.02 \times 10^{-3} \times (\frac{1}{\lambda_1} - \frac{1}{\lambda_2}) + 7.04 \times 10^2 \times \ln\frac{\lambda_1}{\lambda_2}, \qquad (3.7)$$

where λ is in meter. Accordingly, the NLS equations can be written as,

$$\frac{dA_{1x}}{dz} = j\gamma\left(|A_{1x}|^2 + \frac{2}{3}|A_{1y}|^2\right)A_{1x}, \qquad (3.8)$$

$$\frac{dA_{1y}}{dz} = j\gamma\left(|A_{1y}|^2 + \frac{2}{3}|A_{1x}|^2\right)A_{1y}, \qquad (3.9)$$

$$\frac{dA_{2x}}{dz} = j\gamma\left(2|A_{1x}|^2 + \frac{2}{3}|A_{1y}|^2\right)A_{2x} + j\frac{2\gamma}{3}A_{1x}A_{1y}^*A_{2y}e^{-j\Delta B z}, \qquad (3.10)$$

$$\frac{dA_{2y}}{dz} = j\gamma\left(2|A_{1y}|^2 + \frac{2}{3}|A_{1x}|^2\right)A_{2y} + j\frac{2\gamma}{3}A_{1y}A_{1x}^*A_{2x}e^{+j\Delta B z}, \qquad (3.11)$$

where the nonlinear effects induced by the weak probe are neglected. Inserting the solution of Eqs. (3.8)-(3.9),

$$A_{1x}(z) = \sqrt{P_1\cos^2\psi_1}\exp\left[j\gamma P_1\left(\frac{2+\cos^2\psi_1}{3}\right)z + j\theta_{1x}\right],$$

$$A_{1y}(z) = \sqrt{P_1\sin^2\psi_1}\exp\left[j\gamma P_1\left(\frac{2+\sin^2\psi_1}{3}\right)z + j\theta_{1y}\right],$$

into Eqs. (3.10)-(3.11), they become,

$$\frac{dA_{2x}}{dz} = j\frac{2\gamma P_1}{3}\left(1 + 2\cos^2\psi_1\right)A_{2x} \qquad (3.12)$$

$$+ j\frac{\gamma P_1}{3}\sin(2\psi_1)\exp\left[+j\left(\frac{\gamma P_1}{3}\cos(2\psi_1) - \Delta B\right)z + j\Delta\theta_1\right]A_{2y},$$

$$\frac{dA_{2y}}{dz} = j\frac{2\gamma P_1}{3}\left(1 + 2\sin^2\psi_1\right)A_{2y} \qquad (3.13)$$

$$+ j\frac{\gamma P_1}{3}\sin(2\psi_1)\exp\left[-j\left(\frac{\gamma P_1}{3}\cos(2\psi_1) - \Delta B\right)z - j\Delta\theta_1\right]A_{2x},$$

where $\Delta\theta_1 = \theta_{1x} - \theta_{1y}$.

Let $x = A_{2x}\exp(-jkz/2)$, $y = A_{2y}\exp(+jkz/2)$ and $k = \gamma P_1\cos(2\psi_1)/3 - \Delta B$. Then, Eqs. (3.12)-(3.13) can be rewritten as,

$$\frac{dx}{dz} = \Gamma_1 x + j\delta y, \qquad (3.14)$$

$$\frac{dy}{dz} = \Gamma_2 y + j\delta^* x, \qquad (3.15)$$

44

where $\Gamma_1 = j2\gamma P_1(1 + 2\cos^2\psi_1)/3 - jk/2$, $\Gamma_2 = j2\gamma P_1(1 + 2\sin^2\psi_1)/3 + jk/2$ and $\delta = \gamma P_1 \sin(2\psi_1)e^{j\Delta\theta_1}/3$. By differentiating Eq. (3.14) and inserting Eq. (3.15), it becomes a second order homogeneous differential equation, and the solutions are,

$$x = \left(a_x \cos\left(\frac{\hat{k}}{2}z\right) + jb_x \sin\left(\frac{\hat{k}}{2}z\right) \right) \exp\left(j\frac{4\gamma P_1}{3}z \right) , \qquad (3.16)$$

$$y = \left(a_y \cos\left(\frac{\hat{k}}{2}z\right) + jb_y \sin\left(\frac{\hat{k}}{2}z\right) \right) \exp\left(j\frac{4\gamma P_1}{3}z \right) , \qquad (3.17)$$

where

$$\hat{k} = \sqrt{\frac{4}{9}\gamma^2 P_1^2 \sin^2(2\psi_1) + \left[\frac{4}{3}\gamma P_1 \cos(2\psi_1) - k\right]^2} ,$$

$$a_x = A_{2x}(0) = \sqrt{P_2 \cos^2\psi_2}\, e^{j\theta_{2x}} ,$$

$$a_y = A_{2y}(0) = \sqrt{P_2 \sin^2\psi_2}\, e^{j\theta_{2y}} ,$$

$$\hat{k}b_x = \left(\frac{4}{3}\gamma P_1 \cos(2\psi_1) - k\right) a_x + 2\delta a_y ,$$

$$\hat{k}b_y = -\left(\frac{4}{3}\gamma P_1 \cos(2\psi_1) - k\right) a_y + 2\delta^* a_x .$$

From Eqs. (3.16)-(3.17), it is obvious that the XPM-induced phase shifts of two orthogonal fields are not the same normally. Considering differential signals after balanced detection, the track corresponding to adjacent pulses being in-phase is not affected by insufficient phase shift, but the other track is proportional to $|E(t)E(t-T)|\cos\Delta\varphi$, where $E(t)$ is optical field; T is the bit period, and $\Delta\varphi$ is the differential phase between $E(t)$ and $E(t-T)$. Accordingly, when the phase shift induced by the space of the OOK pump is zero, the effective XPM-induced phase shift can be evaluated as,

$$\varphi_{\text{eff}} = \cos^{-1}\left(\frac{|A_{2x}(0)A_{2x}(L)|\cos\varphi_{2x} + |A_{2y}(0)A_{2y}(L)|\cos\varphi_{2y}}{P_2} \right) , \qquad (3.18)$$

where $\varphi_{2x} = \arg\{A_{2x}(L)/A_{2x}(0)\}$ and $\varphi_{2y} = \arg\{A_{2y}(L)/A_{2y}(0)\}$ are the nonlinear phase shifts of two orthogonal fields. φ_{eff} is the function of ψ_1, ψ_2, $\Delta\theta$ and ΔB, and ΔB is relative to fiber birefringence and PPD. When the OOK pump is arbitrarily polarized

and ψ_1 and $\Delta\theta$ are randomly selected, to focus on optimizing the controllable SOP of the probe, $|\Delta B|L \gg 2\pi$ is assumed by setting large PPD and birefringence. Namely, the effective phase shift of Eqs. (3.5) and (3.6) becomes,

$$\tilde{\varphi}_{\text{eff}} = \cos^{-1}\left(\cos^2\psi_2 \cos\left(\frac{2\gamma P_1 L(1 + 2\cos^2\psi_1)}{3}\right)\right. \tag{3.19}$$
$$\left. + \sin^2\psi_2 \cos\left(\frac{2\gamma P_1 L(1 + 2\sin^2\psi_1)}{3}\right)\right),$$

To simulate a polarization scrambled pump beam, the SOP which cover all the Poincaré sphere, as shown in Fig. 3.4(a), are considered to be the SOP of the pump. Using all these SOP and Eq. (3.19), Fig. 3.4(b) shows $\tilde{\varphi}_{\text{eff}}$ with $2\gamma P_1 L = \pi$ as the function of ψ_2, where the multiple curves correspond to all possible SOP. Although launching the probe at the birefringent axis may achieve the desired phase shift of π, it shows the largest phase variation and the lowest possible phase shift of $\pi/3$. Comparatively, by launching the probe at 45° respective to the axes, although its maximum phase shift is sacrificed, the variation is the smallest and its minimum phase shift is the largest. In order to minimize the phase variation and maximize the minimum phase shift, which can impair signal performance most, $\psi_2 = 45°$ is refereed as the best scenario and $\psi_2 = 0$ (or 90°) is the worst scenario.

Therefore, for the desired polarization-insensitive case, $a_x = \sqrt{P_2/2}\, e^{j\theta_{2x}}$ and $a_y = \sqrt{P_2/2}\, e^{j\theta_{2y}}$, where P_2 is the probe power, the converted DPSK signal is,

$$\frac{A_{2x}(L)}{a_x} = \left(\cos\left(\frac{\hat{k}L}{2}\right) + j\tilde{b}_x \sin\left(\frac{\hat{k}L}{2}\right)\right) \exp\left(j\frac{4\gamma P_1 L}{3} + j\frac{kL}{2}\right), \tag{3.20}$$

$$\frac{A_{2y}(L)}{a_y} = \left(\cos\left(\frac{\hat{k}L}{2}\right) + j\tilde{b}_y \sin\left(\frac{\hat{k}L}{2}\right)\right) \exp\left(j\frac{4\gamma P_1 L}{3} - j\frac{kL}{2}\right), \tag{3.21}$$

where

$$\tilde{b}_x = \frac{1}{\hat{k}}\left(\frac{4\gamma P_1}{3}\cos(2\psi_1) - k + 2\tilde{\delta}\right),$$
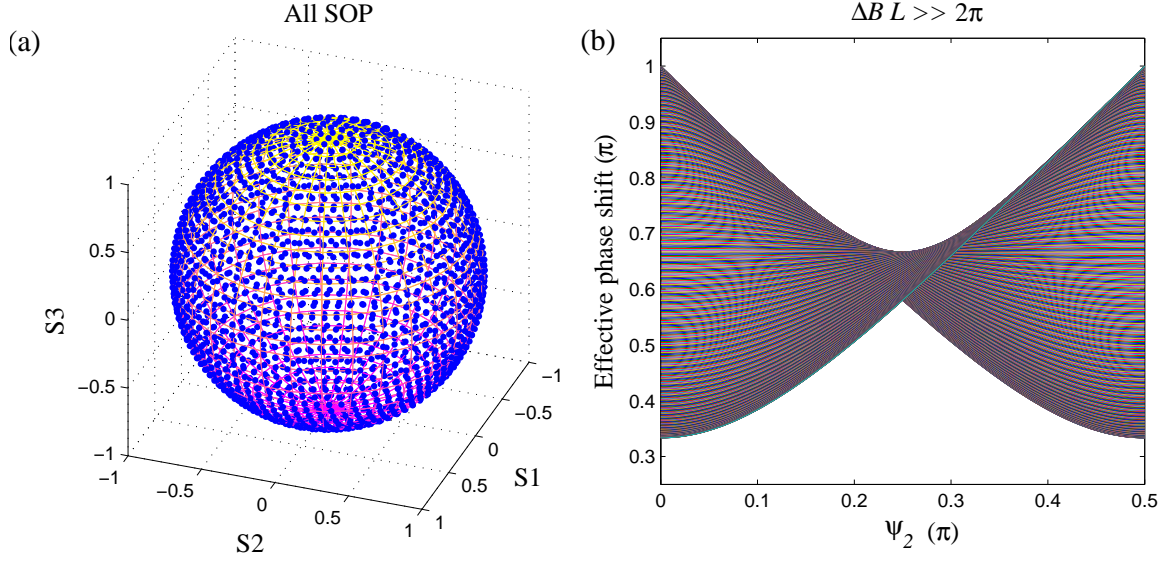
Figure 3.4: (a) All SOP of the pump beam used in simulation, and (b) the effective phase shift with $\Delta BL \gg 2\pi$ as the function of ψ_2

$$\tilde{b}_y = \frac{1}{\hat{k}}\left(-\frac{4\gamma P_1}{3}\cos(2\psi_1) + k + 2\tilde{\delta}^*\right) ,$$

$$\tilde{\delta} = \frac{\gamma P_1}{3}\sin(2\psi_1)e^{j(\Delta\theta_1 - \theta_{2x} + \theta_{2y})} .$$

In contrast, for the worse case, $a_x = \sqrt{P_2}\,e^{j\theta_{2x}}$ and $a_y = 0$, the output signal becomes,

$$\frac{A_{2x}(L)}{a_x} = \left(\cos\left(\frac{\hat{k}L}{2}\right) + j\tilde{\tilde{b}}_x\sin\left(\frac{\hat{k}L}{2}\right)\right)\exp\left(j\frac{4\gamma P_1 L}{3} + j\frac{kL}{2}\right) , \qquad (3.22)$$

$$\frac{A_{2y}(L)}{a_x} = j\frac{2\delta^*}{\hat{k}}\sin\left(\frac{\hat{k}L}{2}\right)\exp\left(j\frac{4\gamma P_1 L}{3} - j\frac{kL}{2}\right) , \qquad (3.23)$$

where

$$\tilde{\tilde{b}}_x = \frac{1}{\hat{k}}\left(\frac{4}{3}\gamma P_1\cos(2\psi_1) - k\right) . \qquad (3.24)$$

Fig. 3.5 depicts all the effective phase shifts as a function of PPD, where $2\gamma P_1 L$, λ_1 and L are set to be π, 1550 nm and 30 m, respectively. When PPD increases, the significance of the last terms of Eqs. (3.10)-(3.11) are reduced, and the variation of effective phase shift is also lowered. Furthermore, while $\Delta BL = 2\pi$ which indicate the total influence of the last terms of Eqs. (3.10)-(3.11) is small, the minimum phase shift variation would be obtained, such as PPD of 7 and 13.5 nm in Fig. 3.5. Consequently, if the birefringent

nonlinear fiber is longer, the PPD required to minimize the phase shift variation is smaller. Moreover, while the probe is launched at the birefringent axes of the fiber, the maximum and minimum nonlinear phase shifts are also plotted in Fig. 3.5 for comparison.
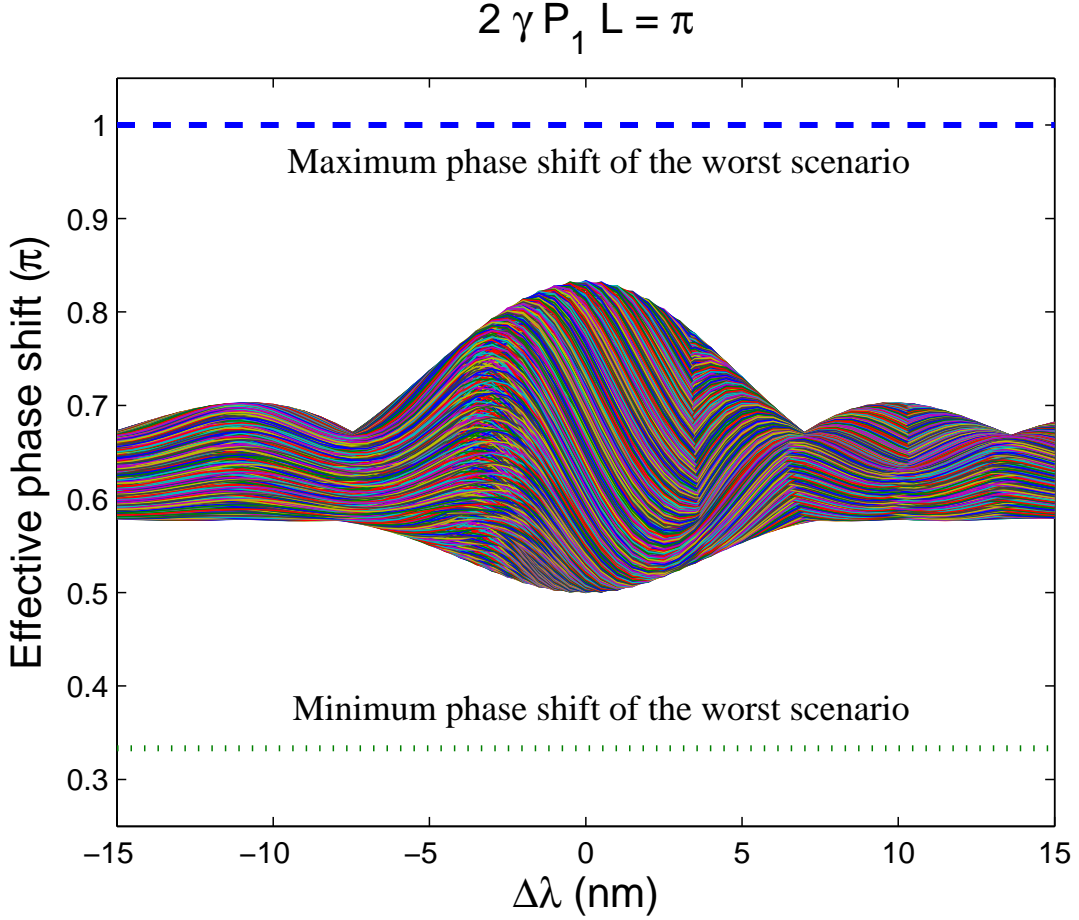
$$2\,\gamma\,P_1\,L = \pi$$

Figure 3.5: With $2\gamma P_1 L = \pi$, the effective phase shift of the best scenario, $\psi_2 = \pi/4$, as the function of PPD.

To investigate the optimal nonlinear effect, Fig. 3.6 depicts the maximum and minimum effective phase shifts with different PPD and nonlinear effects. Compared with PPD of 7 nm ($\Delta BL = 2\pi$), PPD of 3.5 nm ($\Delta BL = \pi$) shows not only larger variation of effective phase shift, but also lower minimum effective phase shift. Moreover, it is evident that the phase shifts of the best scenario with $\Delta BL = 2\pi$ and $\Delta BL \gg 2\pi$ ($\tilde{\varphi}_{\text{eff}}$) are about the same. As shown in Fig. 3.6, the perfect polarization-independent phase shift can be achieved by making $\psi_2 = 45°$, $2\gamma P_1 L = 3\pi/4$ and $\Delta BL \gg 2\pi$, although the effec-

tive phase shift is only 0.5π. Nevertheless, if the optimization represents maximizing the minimum phase shift, $2\gamma P_1 L = 1.1\pi$ is required for the best scenario, and the minimum phase shift has the largest value of about 0.58π. Additionally, $2\gamma P_1 L = 1.5\pi$ is required to achieve the largest minimum phase shift for the worst scenario, and it is only 0.5π.
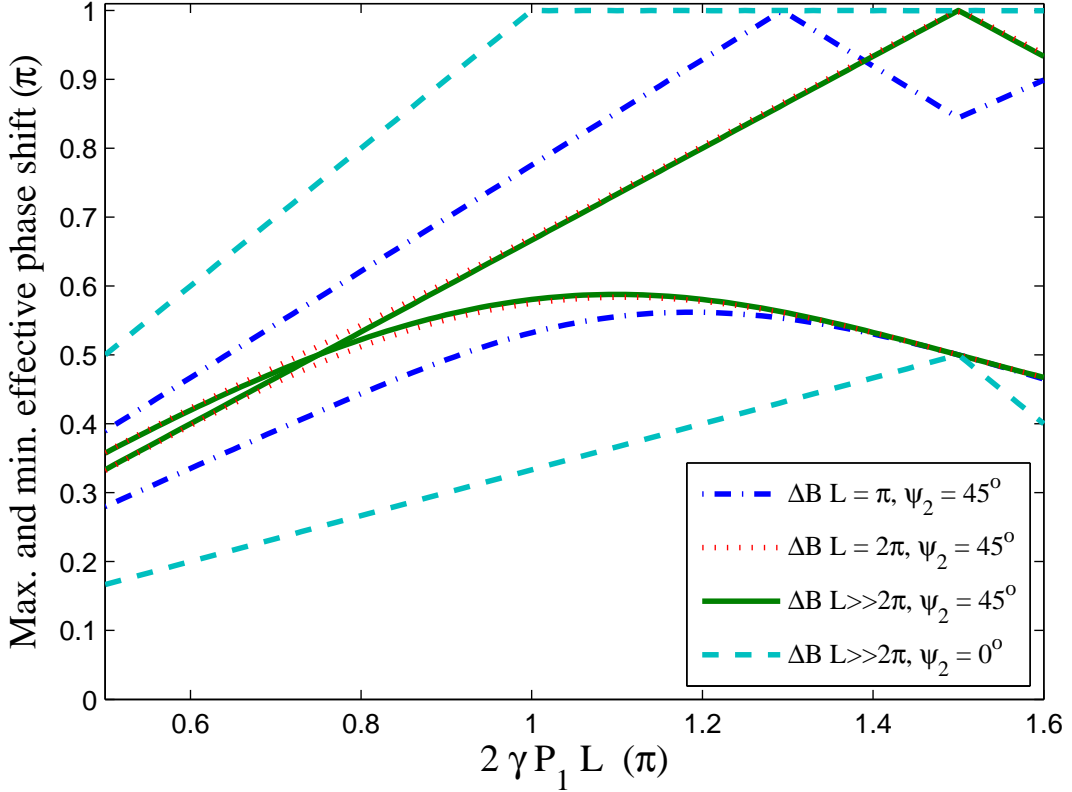
Figure 3.6: Maximum and minimum effective phase shifts as functions of nonlinear effects and PPD

3.2.4 Experimental RZ-OOK-to-RZ-DPSK conversion in a PCF

Figure 3.7 shows the experimental setup of RZ-OOK-to-RZ-DPSK conversion. The pump was a 40-Gbps RZ-OOK signal with PRBS of $2^{31} - 1$, and it was generated by feeding a tunable CW laser into an EAM. The probe was an optical clock generated by a semiconductor mode-locked laser (SMLL) with a fixed wavelength of 1553 nm. Therefore, the PPD in this experiment was adjusted by the pump wavelength. The full widths at
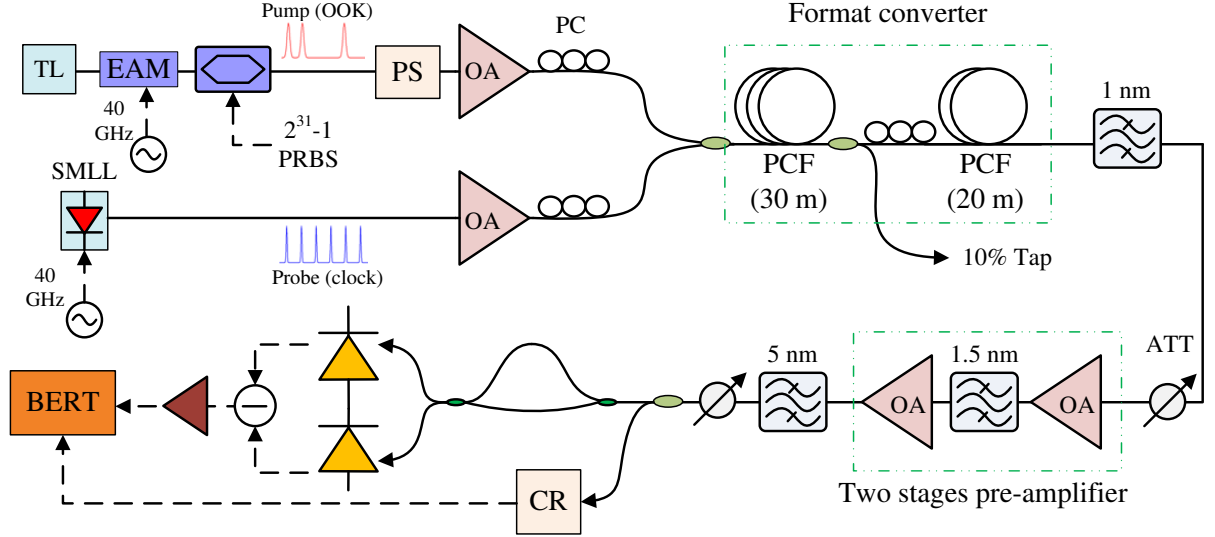
Figure 3.7: Experimental setup of 40 Gbps RZ-OOK-to-RZ-DPSK format converter (TL: tunable laser; SMLL: semiconductor mode-locked laser; EAM: electro-absorption modulator; PS: polarization scrambler; OA: optical amplifier; PC: polarization controller; ATT: optical attenuator; CR: clock recovery; BERT: bit error rate tester)

half maximum (FWHM) of the pump and probe beams are about 6 and 2 ps, respectively, and the much wider FWHM of the pump assures that the XPM-induced phase shift of the probe beam is almost identical over the entire single probe pulse. The SOP of the pump was controlled by a polarization scrambler (PS) to simulate random SOP, and by only a PC without any PS to investigate specific cases. After the high-power optical amplifiers, the average powers of the pump and probe were about 24 and 13 dBm, respectively. The nonlinear birefringent fiber was the commercial PCF (NL·1550·NEG·1 by Crystal Fibre A/S), and two spools of PCFs of 30 m and 20 m were cascaded to get higher nonlinear effect. The nonlinear coefficient and propagation loss of the PCF are 11 $W^{-1}km^{-1}$ and 8 dB/km, respectively. Its normal dispersion of > -1 ps/nm/km over the C-band can avoid modulation instability, and the dispersion slope is only $\sim 10^{-3}$ ps/nm^2/km. For a CW pump, the PCF shows high stimulated Brillouin scattering (SBS) threshold of $\sim$ 25 dBm for lengths of < 100 m. Moreover, the birefringent characteristics of the PCF is described by Eq. (3.7). At the receiver end, two stages pre-amplifier was adopted to obtain low-

noise high-gain amplification, and the balanced detector was used to achieve the 3-dB sensitivity benefit of DPSK signals.

As shown in Figs. 3.5 and 3.6, even though the probe is launched at 45°, sufficient PPD is required to reduce the polarization-dependent variation of the XPM effect. To characterize this PPD-dependent sensitivity, the XPM-induced spectral pedestal of the probe beam was measured [30]. While the XPM effect is strong with a specific SOP, the spectral pedestal must be high, and vice versa. Consequently, the power differential between maximum and minimum spectral pedestal of the probe can implies the amount of the XPM effect variation caused by different SOP of the pump. In order to reduce the spectral overlap between the pump and probe as PPD is small, the probe beam in Fig. 3.7 was replaced by a CW beam at 1553 nm. While the pump was scrambled, an optical spectral analyzer (OSA) was used to record the maximum and minimum power spectra of the probe after the format converter. The measured power differential as a function of PPD is shown in Fig. 3.8, and the theoretical curve calculated by Eqs. (3.20) and (3.21) is also shown for comparison. In theoretical calculation, 2-dB loss was inserted between 30-m and 20-m PCF to simulate the loss of the coupler and splicing. Figure 3.8 demonstrates that the PPD of at least 6 nm is needed to achieve polarization-insensitive XPM effect.

Figures. 3.9(a)-(f) show the eye-diagrams of the converted DPSK signals with the pump at 1547 nm after balanced detection. The FWHM of the eye-diagrams is much broader than 2 ps, because of the bandwidth limitation of the balanced detector, the transimpedance amplifier (TIA) and the oscilloscope. The best signal, as shown in Fig. 3.9(a), obtained by aligning both the pump and probe at the same birefringent axis of the PCF corresponds to the maximum XPM effect. Nevertheless, this best signal is not the best
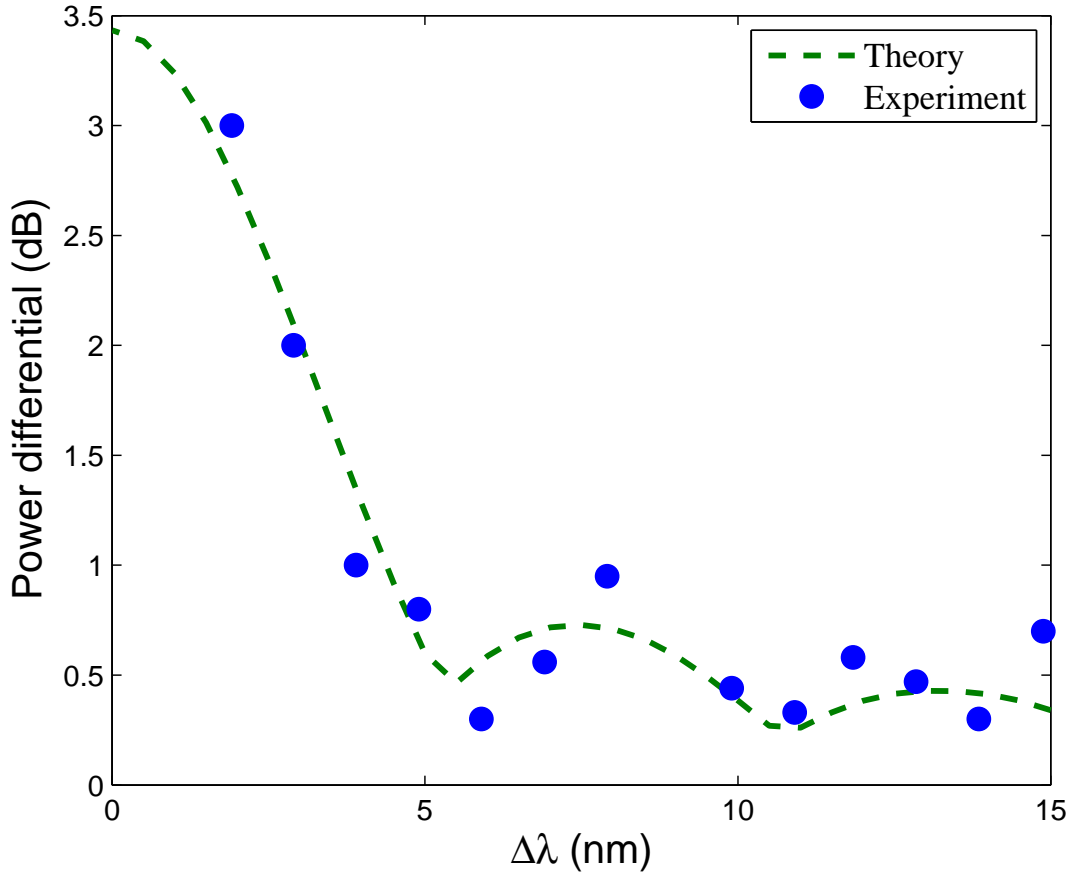
Figure 3.8: The experimental and theoretical power differential of XPM-induced spectral pedestal as a function of PPD

DPSK signal, since $2\gamma P_1 L = \pi$ was not achieved due to the insufficient PCF length and pump power. In contrast, the worst one occurred, when the pump beam was launched at the other orthogonal birefringent axis, as shown in Fig. 3.9(b). While the probe was launched at a birefringent axis and the pump was scrambled, Fig. 3.9(c) shows the corresponding eye-diagram which includes the cases of Figs. 3.9 (a) and (b). On the other hand, as the probe can be launched at 45° relative to the birefringent axes, Figs. 3.9(d)-(f) exhibit the best, the worst and the scrambled cases. Compared with Fig. 3.9(d), Fig. 3.9(a) has wider eye-opening due to larger nonlinear phase shift, but compared with Fig. 3.9(e), Fig. 3.9(b) shows a much worse eye-diagram due to extremely insufficient phase shift.
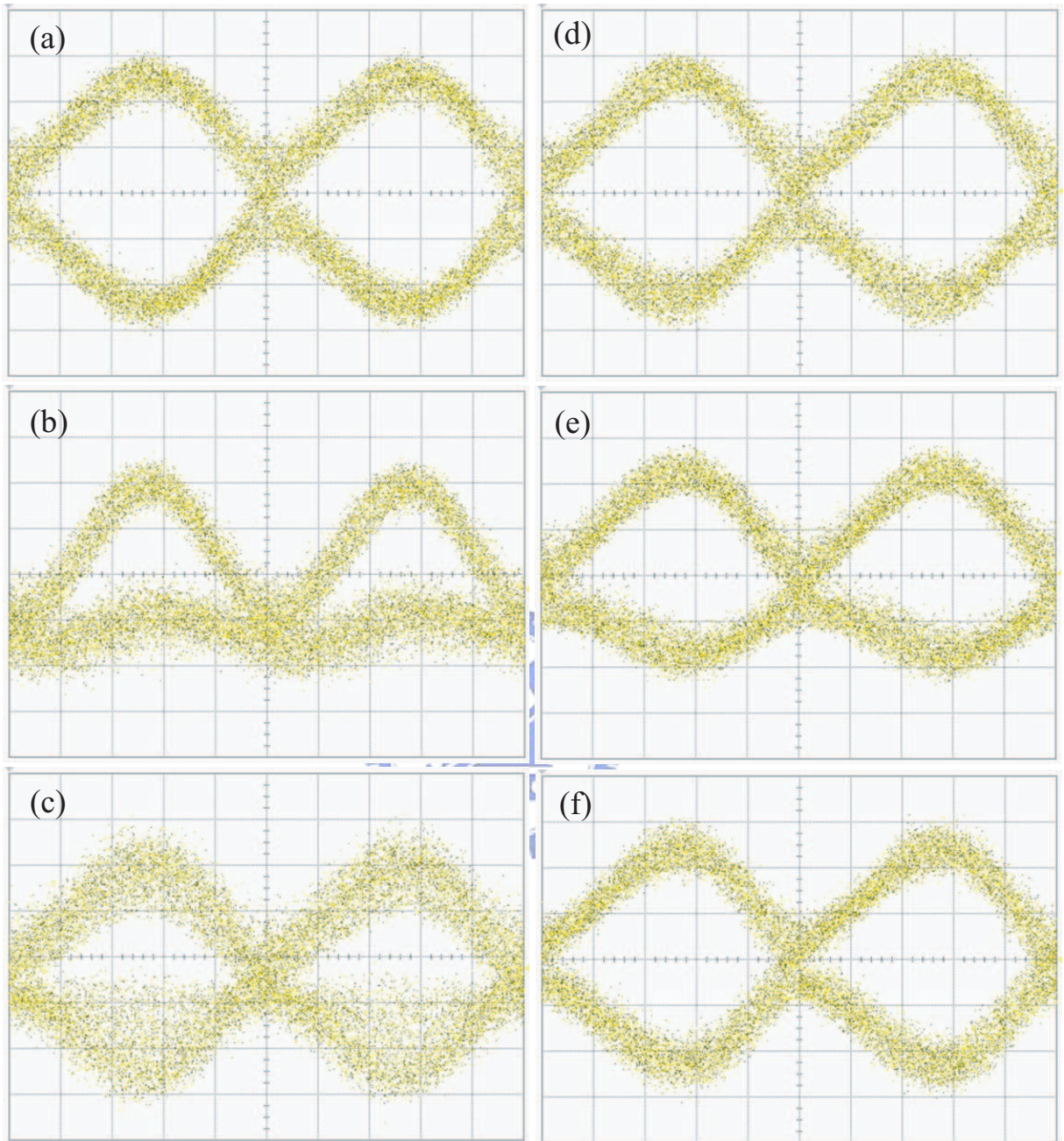
Figure 3.9: The eye-diagrams of converted DPSK signals with the pump at 1547 nm, while (a) the pump and probe beams were launched at the same birefringent axis; (b) the pump and probe beams were launched at different birefringent axes; (c) the pump was scrambled and the probe was launched at a birefringent axis; (d) the probe was launched at 45° relative to birefringent axes and the pump was adjusted to optimize the signal; (e) the probe was launched at 45° relative to birefringent axes and the pump was adjusted to get the worst signal; (f) the pump was scrambled and the probe was launched at 45° relative to birefringent axes.

Accordingly, while the pump is uncontrollable or scrambled, launching the probe at 45°

can avoid the worst case, which degrade signals seriously.
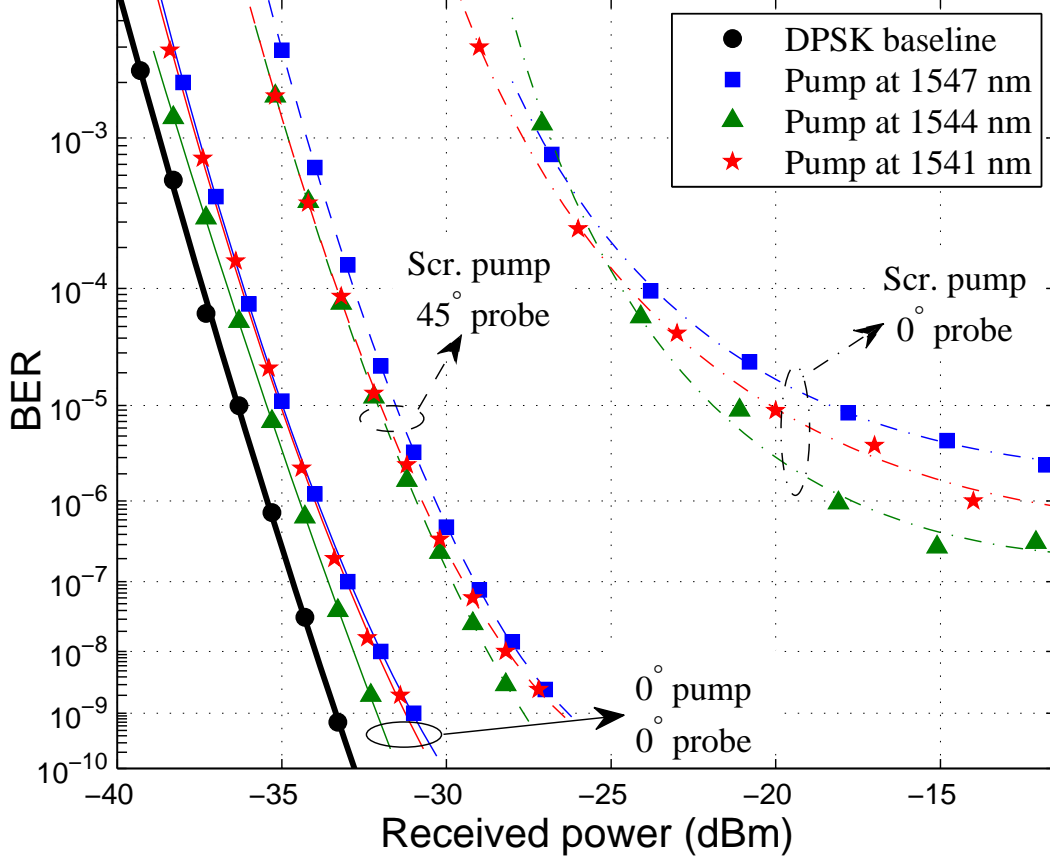
Figure 3.10: The BER measurement of the converted DPSK signals. (Scr.: scrambled; 45°: 45° relative to the birefringent axes; 0°: one of the birefringent axes)

The BER measurement was carried out to investigate the signal performance further, as shown in Fig. 3.10. The baseline of the DPSK signal was generated by an X-cut LN-MZM driven by a PRBS signal with $2V_\pi$ swing biased at the null point. Furthermore, the cases with PPD of 6, 9 and 12 nm, corresponding to the pump at 1547, 1544 and 1541 nm, respectively, were also measured. However, the BER with small PPD, such as 3 nm, cannot be carried out, even though the pump and probe were aligned on the same axis perfectly. This is because the spectra of the pump and probe beams overlap seriously,
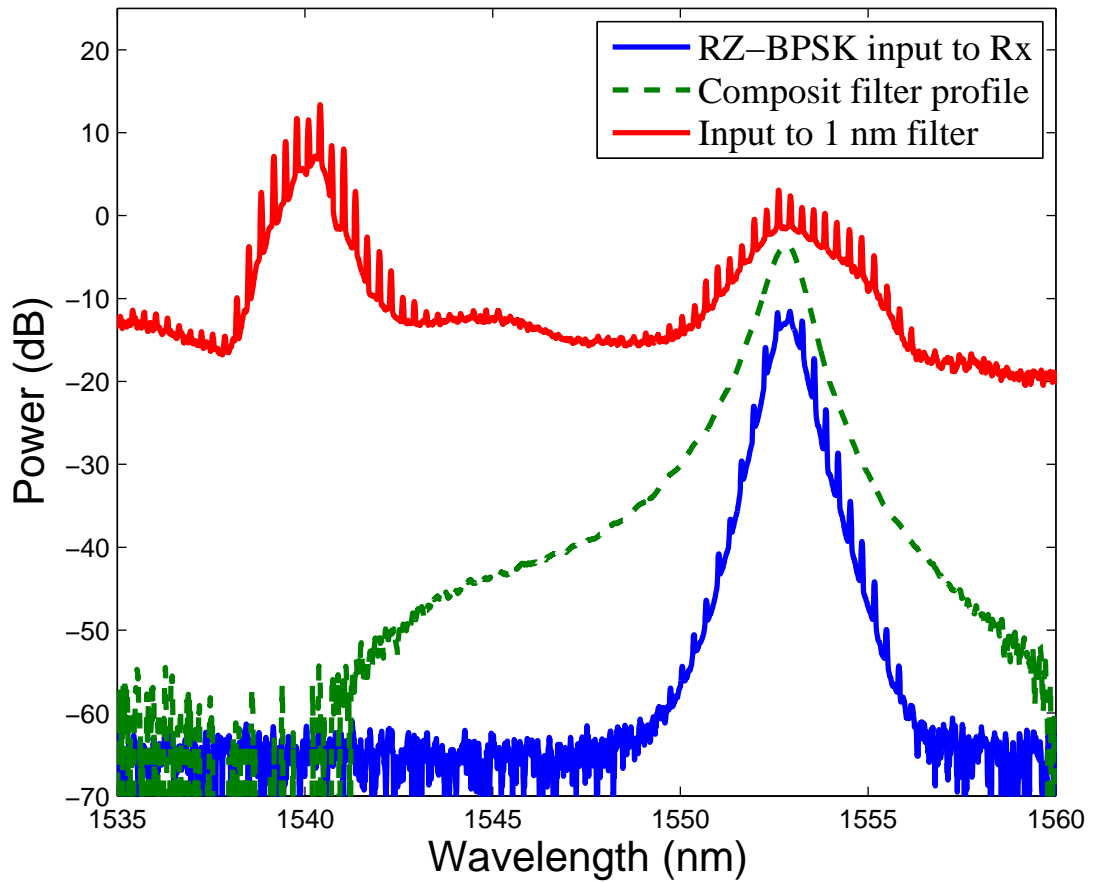
Figure 3.11: The optical spectra obtained with a resolution bandwidth of 0.05 nm and a PPD of 10 nm

and the converted DPSK signal was interfered by the pump signal. Figure 3.11 shows the optical spectra of the output of the PCF, the optical filter with 1-nm FWHM, and the DPSK signal in front of the receiver, where the spectra of both the pump and the probe were broadened by the SPM and XPM effects. Since there is a trade-off between the SPM effect and the OSNR of the probe, the 1-nm width filter can reduce undesired spectral broadening and increase the SPM tolerance. Owing to $2\gamma P_1 L \cong 0.76\,\pi$ in the experiment, the best conditions which was achieved by optimizing both the SOP of the pump and probe and correspond to Fig. 3.9(a) have about 1∼2.5-dB penalties relative to the DPSK baseline. The main reason of different penalties is the OSNR variation of the DPSK

signals due to the uneven gain spectra of the optical amplifiers. While the pump beam was scrambled, launching the probe at one birefringent axis can not achieve error free, but launching it at 45° shows only about 4.5-dB penalty, compared with the corresponding best unscrambled case. Actually, from Figs. 3.5 and 3.6, the minimum nonlinear phase shifts, which would dominate BER, are about the same, if PPD is larger than the first one exhibiting the minimum variation of phase shift (7 nm in Fig. 3.5 and 6 nm in Fig. 3.8). Therefore, the polarization-insensitive format conversion was demonstrated for different PPD, and the penalties induced by the scrambled pump would be about the same, only if PPD is larger than 6 nm. In addition, according to Fig. 3.6, the performance of the DPSK signal converted from the scrambled OOK signal should be improved and optimized, if the pump power or the PCF length can be increased to make $2\gamma P_1 L \cong 1.1\,\pi$.

3.3 Theoretical analyses of the penalty arising from OOK-to-DPSK conversion
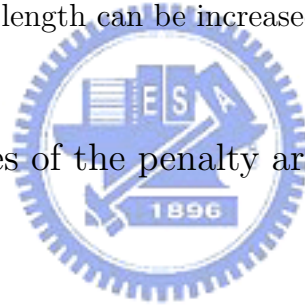
Various impairments to DPSK signals have been investigated [47][48]. However, using the power-dependent XPM effect to convert an OOK signal to a DPSK signal would cause some different issues. As shown in last section, many factors, such as polarization, power and fiber length, may cause insufficient phase shift of a converted DPSK signal. Besides, before arriving a format converter, an OOK signal probably has passed through a few optical amplifiers, and the AN of an OOK signal will be transferred to the PN of a converted DPSK signal through the XPM effect. In the following sections, these two issues will be discussed theoretically.

3.3.1 Insufficient phase shift

To simplify the discussion and to focus it on insufficient phase shift, the phase shift over entire bit period is assumed to be identical. As mentioned in the previous section, this assumption is correct , if the FWHM of OOK pulses is much larger than that of converted DPSK pulses. An optical matched filter preceding the receiver is assumed further, and therefore, the pulse shape of DPSK signals will not affect the discussion.

Considering an amplifier-noise limited DPSK system, the DPSK signal in front of the receiver, as shown in Fig. 3.1(b), can be represented as,

$$E(t) = \left(A_x e^{j\phi_x(t)} + n_x(t) \right) \hat{\mathbf{x}} + \left(A_y e^{j\phi_y(t)} + n_y(t) \right) \hat{\mathbf{y}}, \tag{3.25}$$

where $\phi_{x,y}(t)$ is either $\varphi_{x,y}$ or 0, which is induced by the mark or space of an OOK signal through the XPM effect, and the amplifier noises, n_x and n_y, are independent identically distributed (iid) complex zero-mean circular Gaussian random variables. The variances of the real and imaginary parts of the noises are both σ_n^2, and thus, $\langle |n_x|^2 \rangle = \langle |n_y|^2 \rangle = 2\sigma_n^2$, where $\langle \cdot \rangle$ indicates the expectation value. At the output of a DI, in which the DPSK signal interferes with its delay version, the two output signals are,

$$
\begin{aligned}
E_{\mathrm{DB}} = & \frac{1}{2} \left(A_x e^{j\phi_x(t)} + A_x e^{j\phi_x(t-T)} + n_x(t) + n_x(t-T) \right) \hat{\mathbf{x}} \\
& + \frac{1}{2} \left(A_y e^{j\phi_y(t)} + A_y e^{j\phi_y(t-T)} + n_y(t) + n_y(t-T) \right) \hat{\mathbf{y}},
\end{aligned} \tag{3.26}
$$

$$
\begin{aligned}
E_{\mathrm{AMI}} = & \frac{1}{2} \left(A_x e^{j\phi_x(t)} - A_x e^{j\phi_x(t-T)} + n_x(t) - n_x(t-T) \right) \hat{\mathbf{x}} \\
& + \frac{1}{2} \left(A_y e^{j\phi_y(t)} - A_y e^{j\phi_y(t-T)} + n_y(t) - n_y(t-T) \right) \hat{\mathbf{y}},
\end{aligned} \tag{3.27}
$$

where $n(t)$ and $n(t-T)$ are iid. As shown in Fig. 3.1, the electrical fields of Eqs. (3.26) and (3.27) represent the DB and AMI signals, respectively. Since the amplifier noise dominates the noise source, all the electrical noises are neglected, and the detector responsivity is set to be unity. Hence, the photocurrents at the output of detectors could be represented

as $|E_{\text{DB}}(t)|^2$ and $|E_{\text{AMI}}(t)|^2$, respectively. While two neighboring pulses are in-phase, $\phi_{x,y}(t) - \phi_{x,y}(t-T) = 0$, the photocurrents are,

$$i_{\text{DB}}(t) = \left| A_x + \frac{n_x(t) + n_x(t-T)}{2} \right|^2 + \left| A_y + \frac{n_y(t) + n_y(t-T)}{2} \right|^2 , \qquad (3.28)$$

$$i_{\text{AMI}}(t) = \left| \frac{n_x(t) - n_x(t-T)}{2} \right|^2 + \left| \frac{n_y(t) - n_y(t-T)}{2} \right|^2 . \qquad (3.29)$$

As $\phi_{x,y}(t) = \phi_{x,y}(t-T) = \varphi_{x,y}$, the relative phase shift between the signal and noise, $e^{j\varphi_{x,y}}$, is ignored in Eq. (3.28), because $[n_{x,y}(t) + n_{x,y}(t-T)]/2$ is still a complex circular Gaussian noise. In contrast, if two neighboring pulses are out-of-phase, $\phi_{x,y}(t) - \phi_{x,y}(t-T) = \pm\varphi_{x,y}$, the photocurrents become,

$$i_{\text{DB}}(t) = \left| A_x \cos\left(\frac{\varphi_x}{2}\right) + \frac{n_x(t) + n_x(t-T)}{2} \right|^2$$
$$+ \left| A_y \cos\left(\frac{\varphi_y}{2}\right) + \frac{n_y(t) + n_y(t-T)}{2} \right|^2 , \qquad (3.30)$$

$$i_{\text{AMI}}(t) = \left| A_x \sin\left(\frac{\varphi_x}{2}\right) + \frac{n_x(t) - n_x(t-T)}{2} \right|^2$$
$$+ \left| A_y \sin\left(\frac{\varphi_y}{2}\right) + \frac{n_y(t) - n_y(t-T)}{2} \right|^2 , \qquad (3.31)$$

where the relative phase shift between the signal and noise is also neglected for the same reason. Obviously, Eqs. (3.30) and (3.31) would become Eqs. (3.29) and (3.28), respectively, when the phase shift is optimized, i.e. $\varphi_{x,y} = \pi$. Furthermore, since $n_x(t) \pm n_x(t-T)$ and $n_y(t) \pm n_y(t-T)$ are independent of each other, all $[n_{x,y}(t) \pm n_{x,y}(t-T)]/2$ in Eqs. (3.28)-(3.31) can be treated as iid complex circular Gaussian random variable with the variance of $2\sigma^2 = \sigma_n^2$. Accordingly, after normalizing the photocurrents by σ^2, their probability density functions (pdf) are noncentral or central χ^2 distributions with four degrees of freedom,

$$p_{X_1}(x_1) = \frac{1}{2}\sqrt{\frac{x_1}{\lambda_1}} e^{-\frac{\lambda_1 + x_1}{2}} I_1\left(\sqrt{\lambda_1 x_1}\right) , \qquad (3.32)$$

$$p_{X_2}(x_2) = \frac{1}{4} x_2 e^{-\frac{x_2}{2}} , \qquad (3.33)$$

$$p_{X_3}(x_3) = \frac{1}{2}\sqrt{\frac{x_3}{\lambda_3}}e^{-\frac{\lambda_3+x_3}{2}}I_1\left(\sqrt{\lambda_3 x_3}\right), \tag{3.34}$$

$$p_{X_4}(x_4) = \frac{1}{2}\sqrt{\frac{x_4}{\lambda_4}}e^{-\frac{\lambda_4+x_4}{2}}I_1\left(\sqrt{\lambda_4 x_4}\right). \tag{3.35}$$

Eqs. (3.32)-(3.35) correspond to Eqs. (3.28)-(3.31), respectively, where $x = i/\sigma^2$, $\lambda_1 = \left(A_x^2 + A_y^2\right)/\sigma^2$, $\lambda_3 = \lambda_1\cos^2(\varphi_{\mathrm{eff}}/2)$ and $\lambda_4 = \lambda_1\sin^2(\varphi_{\mathrm{eff}}/2)$, and they are mutually independent. The definition of φ_{eff} is equivalent to Eq. (3.18), in which $|A_{2x,y}(0)A_{2x,y}(L)|$ is replaced by $A_{x,y}^2$. Because the photocurrent after balanced detection, $i_{\mathrm{bal}}(t) = i_{\mathrm{DB}}(t) - i_{\mathrm{AMI}}(t)$, is used to determine the logic of a received signal, the error probabilities with a threshold, h, are,

$$p_e^{\mathrm{in}} = \langle X_1 - X_2 < h\rangle = \int_0^\infty\left[\int_0^{x_2+h}p_{X_1}(x_1)\,\mathrm{d}x_1\right]p_{X_2}(x_2)\,\mathrm{d}x_2, \tag{3.36}$$

$$p_e^{\mathrm{out}} = \langle X_3 - X_4 > h\rangle = \int_0^\infty\left[\int_{x_4+h}^\infty p_{X_3}(x_3)\,\mathrm{d}x_3\right]p_{X_4}(x_4)\,\mathrm{d}x_4, \tag{3.37}$$

where the superscript indicates two neighboring pulses being in-phase or out-of-phase, and h is set to be greater than or equivalent to zero. The reason to assume $h \geq 0$ is that the penalty caused by insufficient phase shift, $\varphi_{\mathrm{eff}} < \pi$, only degrades the out-of-phase case.

Eq. (3.36) has an analytical solution (Appendix A),

$$p_e^{\mathrm{in}} = 1 - Q_1\left(2\sqrt{\rho_s},\sqrt{h}\right) + \frac{1}{2}e^{-\rho_s+\frac{h}{2}}Q_1\left(\sqrt{2\rho_s},\sqrt{2h}\right) \tag{3.38}$$

$$-\frac{1}{8}e^{-2\rho_s-\frac{h}{2}}\sqrt{\frac{h}{\rho_s}}I_1\left(2\sqrt{\rho_s h}\right) + \frac{1}{8}e^{-2\rho_s-\frac{h}{2}}\sum_{m=1}^\infty m\left(\frac{\rho_s}{h}\right)^{\frac{m}{2}}I_m\left(2\sqrt{\rho_s h}\right),$$

where $\rho_s = (A_x^2 + A_y^2)/(2\sigma_n^2)$ is the signal-to-noise ratio (SNR); I_m is the mth order modified bessel function; Q_m is the well-known Marcum Q-function,

$$Q_m(\mathcal{A},\mathcal{B}) = \frac{1}{\mathcal{A}^{m-1}}\int_\mathcal{B}^\infty x^m e^{-\frac{x^2+\mathcal{A}^2}{2}}I_{m-1}(\mathcal{A}x)\,\mathrm{d}x, \tag{3.39}$$

and m is a positive integer. Additionally, the analytical form of Eq. (3.37) is,

$$p_e^{\mathrm{out}} = \frac{4+h}{8}e^{-\rho_s-\frac{h}{2}}I_0\left(\rho_s\sin\varphi_{\mathrm{eff}}\right) + \frac{1}{8}e^{-\rho_s-\frac{h}{2}}\tan\left(\frac{\varphi_{\mathrm{eff}}}{2}\right)I_1\left(\rho_s\sin\varphi_{\mathrm{eff}}\right)$$

$$+e^{-\rho_s-\frac{h}{2}} \sum_{n=2}^{\infty} \left(\mathbf{c}_n + \frac{\mathbf{d}_n}{8} \right) \cot^{n-1}\left(\frac{\varphi_{\text{eff}}}{2}\right) I_{n-1}\left(\rho_s \sin \varphi_{\text{eff}}\right) , \tag{3.40}$$

where

$$\mathbf{c}_2 = 1 + \frac{h}{2} ,$$

$$\mathbf{c}_n = 1 + \frac{h}{2} + \sum_{l=2}^{n-1} \left[\frac{(-1)^{n-l}}{2} \binom{n-2}{l-1} + \sum_{m=l}^{n-1} (-1)^{m-l} \binom{m-1}{l-1} \right] \frac{h^l}{l!} , \qquad n \geq 3 ,$$

$$\mathbf{d}_2 = -1 - h + \frac{h^2}{2} ,$$

$$\mathbf{d}_n = \sum_{l=1}^{n-2} (-1)^{n-l} \left[\binom{n-1}{l-1} - \binom{n-3}{l-1} \right] \frac{h^l}{l!} - \frac{h^{n-1}}{(n-2)!} + \frac{h^n}{n!} , \qquad n \geq 3 .$$

$\binom{n}{k} = \Gamma(n+1)/\Gamma(k+1)/\Gamma(n-k+1)$ is the binomial coefficient, and $\Gamma(\cdot)$ is the Gamma function. Actually, while φ_{eff} is small and h is required to be large, Eq. (3.40) is hard to converge numerically, and it is easier to calculate the error probability through its integration form,

$$p_e^{\text{out}} = \frac{1}{4} \csc\left(\frac{\varphi_{\text{eff}}}{2}\right) e^{-2\rho_s \sin^2\left(\frac{\varphi_{\text{eff}}}{2}\right)} \tag{3.41}$$
$$\times \int_0^{\infty} \sqrt{\frac{x}{\rho_s}} e^{-\frac{x}{2}} I_1\left(2\sqrt{\rho_s x} \sin\left(\frac{\varphi_{\text{eff}}}{2}\right)\right) Q_2\left(2\sqrt{\rho_s} \cos\left(\frac{\varphi_{\text{eff}}}{2}\right), \sqrt{x+h}\right) \mathrm{d}x .$$

Moreover, if $h = 0$, Eqs. (3.38) and (3.40) become [49],

$$p_{e0}^{\text{in}} = \frac{1}{2} e^{-\rho_s} \left(1 + \frac{\rho_s}{4}\right) , \tag{3.42}$$

$$p_{e0}^{\text{out}} = Q_1\left(\sqrt{2\rho_s} \cos\left(\frac{\varphi_{\text{eff}}}{2}\right), \sqrt{2\rho_s} \sin\left(\frac{\varphi_{\text{eff}}}{2}\right)\right) - \frac{1}{2} e^{-\rho_s} I_0(\rho_s \sin \varphi_{\text{eff}})$$
$$+ \frac{1}{8} e^{-\rho_s} \left(\tan\left(\frac{\varphi_{\text{eff}}}{2}\right) - \cot\left(\frac{\varphi_{\text{eff}}}{2}\right)\right) I_1(\rho_s \sin \varphi_{\text{eff}}) . \tag{3.43}$$

Undoubtedly, Eq. (3.43) equals to Eq. (3.42) as $\varphi_{\text{eff}} = \pi$. While the probabilities of in-phase and out-of-phase cases are the same, the total error probability is,

$$p_e = \frac{p_e^{\text{in}} + p_e^{\text{out}}}{2} . \tag{3.44}$$

Actually, the fixed threshold of zero for an ideal DPSK signal is one of its advantages, compared with the SNR-dependent threshold of an OOK signal. However, as $\varphi_{\text{eff}} \neq \pi$,

the optimal threshold is not zero apparently, and it can be obtained by,

$$\frac{\mathrm{d}p_e}{\mathrm{d}h}\bigg|_{h=h_{\mathrm{opt}}} = 0 \,.$$

That is,

$$
\begin{aligned}
0 = \int_0^\infty \sqrt{x(x+h_{\mathrm{opt}})}e^{-x}\bigg[\sqrt{x}I_1\Big(2\sqrt{\rho_s(x+h_{\mathrm{opt}})}\Big) \\
- \frac{2\csc\varphi_{\mathrm{eff}}}{\sqrt{\rho_s}}I_1\Big(2\sqrt{\rho_s x}\sin\Big(\frac{\varphi_{\mathrm{eff}}}{2}\Big)\Big) I_1\Big(2\sqrt{\rho_s(x+h_{\mathrm{opt}})}\cos\Big(\frac{\varphi_{\mathrm{eff}}}{2}\Big)\Big)\bigg]\,\mathrm{d}x\,.
\end{aligned}
\tag{3.45}
$$

Furthermore, if a polarized receiver is adopted, the noise which orthogonal to the DPSK signal will be filtered out. In this case, all the equations can be renovated by assuming $A_y = n_y = 0$ in Eqs. (3.28)-(3.31). The pdf of the photocurrents become to the ones with second degrees of freedom,

$$p_{X_1}(x_1) = \frac{1}{2}e^{-\frac{\lambda_1+x_1}{2}}I_0\Big(\sqrt{\lambda_1 x_1}\Big)\,, \tag{3.46}$$

$$p_{X_2}(x_2) = \frac{1}{2}e^{-\frac{x_2}{2}}\,, \tag{3.47}$$

$$p_{X_3}(x_3) = \frac{1}{2}e^{-\frac{\lambda_3+x_3}{2}}I_0\Big(\sqrt{\lambda_3 x_3}\Big)\,, \tag{3.48}$$

$$p_{X_4}(x_4) = \frac{1}{2}e^{-\frac{\lambda_4+x_4}{2}}I_0\Big(\sqrt{\lambda_4 x_4}\Big)\,. \tag{3.49}$$

The error probabilities of Eqs. (3.38), (3.40)-(3.43) can be derived as,

$$p_e^{\mathrm{in}} = 1 - Q_1\Big(2\sqrt{\rho_s}, \sqrt{h}\Big) + \frac{1}{2}e^{-\rho_s+\frac{h}{2}}Q_1\Big(\sqrt{2\rho_s}, \sqrt{2h}\Big)\,, \tag{3.50}$$

$$
\begin{aligned}
p_e^{\mathrm{out}} = \frac{1}{2}e^{-\rho_s-\frac{h}{2}}I_0\left(\rho_s\sin\varphi_{\mathrm{eff}}\right) \\
+ e^{-\rho_s-\frac{h}{2}}\sum_{n=2}^\infty \mathbf{c}_n \cot^{n-1}\Big(\frac{\varphi_{\mathrm{eff}}}{2}\Big)I_{n-1}\left(\rho_s\sin\varphi_{\mathrm{eff}}\right)\,,
\end{aligned}
\tag{3.51}
$$

$$
\begin{aligned}
p_e^{\mathrm{out}} = \frac{1}{2}e^{-2\rho_s\sin^2\left(\frac{\varphi_{\mathrm{eff}}}{2}\right)} \\
\times \int_0^\infty e^{-\frac{x}{2}}I_0\Big(2\sqrt{\rho_s x}\sin\Big(\frac{\varphi_{\mathrm{eff}}}{2}\Big)\Big)Q_1\Big(2\sqrt{\rho_s}\cos\Big(\frac{\varphi_{\mathrm{eff}}}{2}\Big), \sqrt{x+h}\Big)\,\mathrm{d}x\,,
\end{aligned}
\tag{3.52}
$$

$$p_{e0}^{\mathrm{in}} = \frac{1}{2}e^{-\rho_s}\,, \tag{3.53}$$

$$p_{e0}^{\mathrm{out}} = Q_1\Big(\sqrt{2\rho_s}\cos\Big(\frac{\varphi_{\mathrm{eff}}}{2}\Big), \sqrt{2\rho_s}\sin\Big(\frac{\varphi_{\mathrm{eff}}}{2}\Big)\Big) - \frac{1}{2}e^{-\rho_s}I_0(\rho_s\sin\varphi_{\mathrm{eff}})\,, \tag{3.54}$$

and the optimal threshold becomes,

$$0 = \int_0^\infty e^{-x} \left[I_0\left(2\sqrt{\rho_s(x + h_{\mathrm{opt}})} \right) \right.$$
$$\left. - I_0\left(2\sqrt{\rho_s x}\, \sin\left(\frac{\varphi_{\mathrm{eff}}}{2}\right) \right) I_0\left(2\sqrt{\rho_s(x + h_{\mathrm{opt}})}\, \cos\left(\frac{\varphi_{\mathrm{eff}}}{2}\right) \right) \right] \, \mathrm{d}x . \tag{3.55}$$
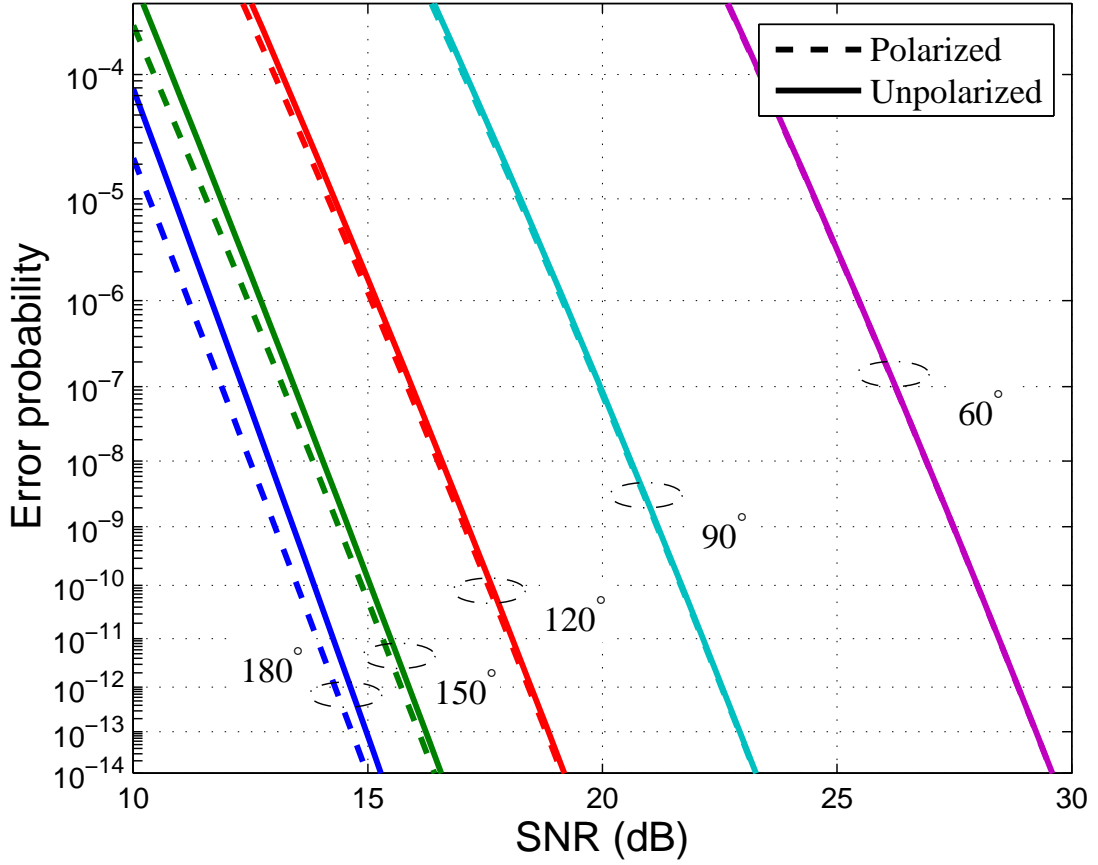
Figure 3.12: The error probabilities of DPSK signals with various phase shifts

Figure 3.12 shows the results of Eqs. (3.38), (3.41), (3.50) and (3.52), and the optimal threshold is adopted. Because the noise orthogonal to the signal is filtered, the polarized receiver can outperform the unpolarized recevier. However, while the SNR is larger than ~ 19 dB, there is no obvious difference between the polarized and unpolarized cases. The reason is that the signal-noise beating noise would dominate the noise source, and

therefore, the orthogonal noise, which does not play a part in the beating noise, is not important. Furthermore, by comparing Eqs. (3.38) and (3.50), they are almost identical as the SNR is high.
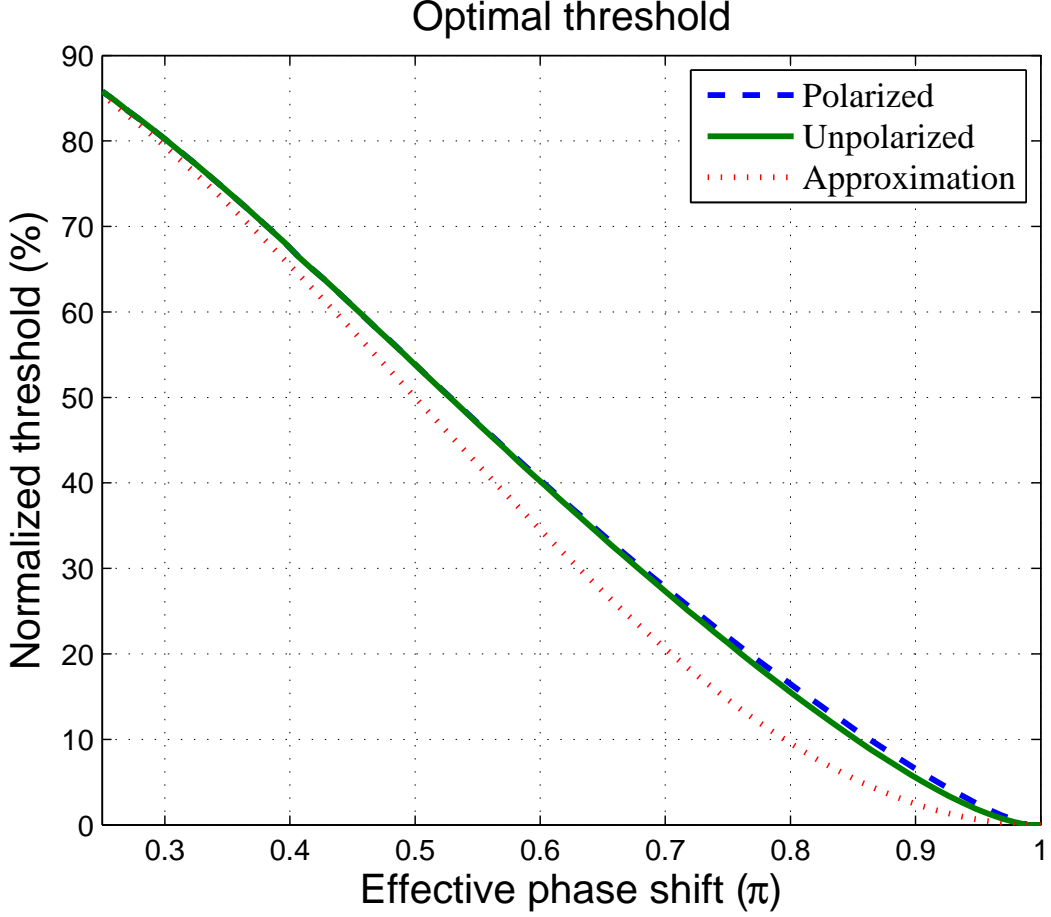
Figure 3.13: Normalized optimal threshold

Since the optimal thresholds of Eqs (3.45) and (3.55) have integration forms, it is not easy to obtain the solution directly. A simple approximation can be made by assuming that the in-phase and out-of-phase traces are symmetric. In other words, the threshold is set in the middle of two traces with $\sigma_n^2 = 0$,

$$\tilde{h}_{\mathrm{opt}} = \frac{\lambda_1 + (\lambda_3 - \lambda_4)}{2} = 4\rho_s \cos^2\left(\frac{\varphi_{\mathrm{eff}}}{2}\right). \tag{3.56}$$

Figure 3.13 depicts the optimal and approximated thresholds normalized by λ_1. The maximum error of the approximated threshold is $\sim 7\%$, and it occurs around $\varphi_{\mathrm{eff}} = 0.65\pi$.
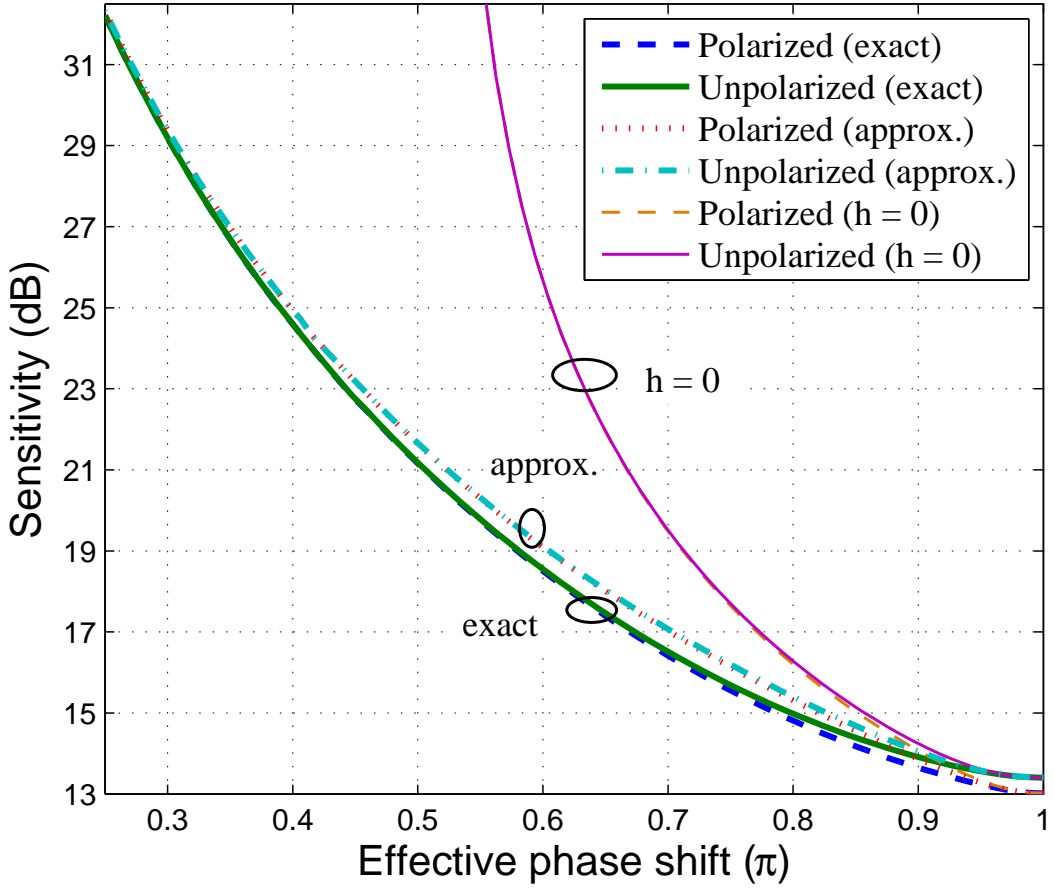
Figure 3.14: The sensitivity of DPSK signals as a function of effective phase shift

According to [49], the error probabilities of differential quadrature phase-shift keying (DQPSK) signal with an unpolarized and a polarized receiver are,

$$p_e = Q_1(\mathcal{A}, \mathcal{B}) - \frac{1}{2}e^{-\frac{\mathcal{A}^2 + \mathcal{B}^2}{2}}I_0(\mathcal{A}\mathcal{B}) + \frac{1}{8}e^{-\frac{\mathcal{A}^2 + \mathcal{B}^2}{2}}\left(\frac{\mathcal{B}}{\mathcal{A}} - \frac{\mathcal{A}}{\mathcal{B}}\right)I_1(\mathcal{A}\mathcal{B}),\qquad(3.57)$$

$$p_e = Q_1(\mathcal{A}, \mathcal{B}) - \frac{1}{2}e^{-\frac{\mathcal{A}^2 + \mathcal{B}^2}{2}}I_0(\mathcal{A}\mathcal{B}),\qquad(3.58)$$

where

$$\mathcal{A} = \sqrt{\rho_s\left(1 - \sqrt{\frac{1}{2}}\right)}, \qquad \mathcal{B} = \sqrt{\rho_s\left(1 + \sqrt{\frac{1}{2}}\right)},$$

and the corresponding sensitivities are both about 17.9 dB. According to Fig. 3.14, in which the sensitivity of DPSK signals as a function of effective phase shift is shown, the DPSK signal with the phase shift of $\pi/2$ is worse than the DQPSK and OOK signals,

64

while the distance between symbols of the DPSK signal is the same to that of OOK signal (Fig. 3.2) and the nearest one of DQPSK signal. This indicates that the distance between symbols is not a good way to tell signal performance when direct detection is adopted. Moreover, using the approximated threshold of Eq. (3.56), the approximated sensitivities are also plotted in Fig. 3.14, and the maximum error is only about 0.7 dB indicating the approximation is acceptable. If the threshold is fixed at 0, the much higher SNR required to achieve the error probability of 10^{-9} is also shown in Fig. 3.14.

According to Figs. 3.6, 3.13 and 3.14, for the worse scenario with $\Delta BL \gg 2\pi$ and $2\gamma P_1 L = \pi$, the optimized thresholds and penalties of the DPSK probe are $0 \sim 76.2\%$ and $0 \sim 14.1$ dB, and they become $0 \sim 53.8\%$ and $0 \sim 7.8$ dB by setting $2\gamma P_1 L = 1.5\pi$. By contrast, for the best scenario with $\Delta BL \gg 2\pi$ and $2\gamma P_1 L = \pi$, they can be reduced to $31.5\% \sim 42.8\%$ and 3.7 dB ~ 5.6 dB, and they become $23.2\% \sim 41.8\%$ and 2.5 dB $\sim$ 5.4 dB by setting $2\gamma P_1 L = 1.1\pi$. As a result, launching the probe at $45°$ can decrease the variations of both threshold and sensitivity caused by arbitrary polarized OOK pump, but the penalty is never zero. Moreover, for the perfect polarization-independent operation, the phase shift is always only $\pi/2$, and the penalty is 7.8 dB. It implies that the signal is worse than an OOK signal, even though their symbol distances on the constellation diagram are the same.

3.3.2 Finite SNR of OOK

While a format converter is put in a gateway to convert OOK signals from remote nodes, the SNR of these OOK signals is finite due to optical amplifiers used to compensate transmission loss or increase nonlinear effect in format conversion. Because the format conversion is realized by XPM effect, finite SNR of OOK signals may be harmful to

converted DPSK signals through AN to PN conversion.

Considering only the noise parallel with an OOK signal, the powers of the mark and space of the OOK are,

$$y_{\text{on}} = |A_1 + n_1|^2 \, , \tag{3.59}$$

$$y_{\text{off}} = |n_1|^2 \, , \tag{3.60}$$

where n_1 is a complex zero-mean circular Gaussian noise with the variance of $2\sigma_1^2$, and the SNR of the OOK signal is $\rho_1 = A_1^2/(4\sigma_1^2)$. Because y_{on}/σ_1^2 and $y_{\text{off}}/\sigma_1^2$ have second order noncentral and central χ^2 distributions, the pdf of optical power are,

$$p_{Y_{\text{on}}}(y) = \frac{1}{2\sigma_1^2} e^{-\frac{A_1^2 + y}{2\sigma_1^2}} I_0\left(\sqrt{y}\frac{A_1}{\sigma_1^2}\right)$$

$$= \frac{1}{2\pi} \int_{-\infty}^{\infty} \frac{\exp\left(\dfrac{jA_1^2 t}{1 - j2\sigma_1^2 t}\right)}{1 - j2\sigma_1^2 t} e^{-jyt} \, \mathrm{d}t \, , \tag{3.61}$$

$$p_{Y_{\text{off}}}(y) = \frac{1}{2\sigma_1^2} e^{-\frac{y}{2\sigma_1^2}}$$

$$= \frac{1}{2\pi} \int_{-\infty}^{\infty} \frac{1}{1 - j2\sigma_1^2 t} e^{-jyt} \, \mathrm{d}t \, , \tag{3.62}$$

which are also represented by the Fourier transform of their characteristic functions. Using XPM effect in a nonlinear medium to convert OOK to DPSK, $2\gamma A_1^2 L_{\text{eff}} = \pi$ is required, where L_{eff} is the effective length of the nonlinear medium. Moreover, the power fluctuation of the OOK signal would also be converted to the PN of the DPSK signal through the relation, $2\gamma L_{\text{eff}} Y = \Theta$. However, $\Theta \in [-\pi, \pi]$ is periodic, and the characteristics of the pdf of Θ must be discrete. Accordingly, the pdf of Θ are,

$$p_{\Theta_\pi}(\theta) = \frac{1}{4\pi\gamma L_{\text{eff}}} \sum_{\frac{m'}{2\gamma L_{\text{eff}}} = -\infty}^{\infty} \frac{\exp\left(\dfrac{jA_1^2 m'}{1 - j2\sigma_1^2 m'}\right)}{1 - j2\sigma_1^2 m'} e^{-j\frac{\theta m'}{2\gamma L_{\text{eff}}}}$$

$$= \frac{1}{2\pi} \sum_{m=-\infty}^{\infty} \frac{\exp\left(\dfrac{j\pi m}{1 - j2\tilde{\sigma}^2 m}\right)}{1 - j2\tilde{\sigma}^2 m} e^{-jm\theta} \, , \tag{3.63}$$

66

$$p_{\Theta_0}(\theta) = \frac{1}{4\pi\gamma L_{\text{eff}}} \sum_{\frac{m'}{2\gamma L_{\text{eff}}}=-\infty}^{\infty} \frac{1}{1 - j2\sigma_1^2 m'} e^{-j\frac{\theta m'}{2\gamma L_{\text{eff}}}}$$

$$= \frac{1}{2\pi} \sum_{m=-\infty}^{\infty} \frac{1}{1 - j2\tilde{\sigma}^2 m} e^{-jm\theta}, \tag{3.64}$$

where $\tilde{\sigma}^2 = 2\gamma L_{\text{eff}}\sigma_1^2 = \pi/(4\rho_1)$. However, since $|1 - j2\tilde{\sigma}^2 m|^{-1}$ decreases slowly as m increases, it is difficult to calculate $p_{\Theta_0}(\theta)$ by the Fourier series of Eq. (3.64). In fact, $p_{\Theta_0}(\theta)$ can be represented by convolution to avoid the numerically convergent problem, and it is,

$$p_{\Theta_0}(\theta) = \frac{1}{2\tilde{\sigma}^2} \sum_{m=-\infty}^{\infty} e^{-\frac{\theta - 2m\pi}{2\tilde{\sigma}^2}} \times \begin{cases} \dfrac{1}{1 - e^{-\frac{\pi}{\tilde{\sigma}^2}}} & \text{if } \theta \in [\theta, \pi] \\[3mm] \dfrac{1}{e^{\frac{\pi}{\tilde{\sigma}^2}} - 1} & \text{if } \theta \in [-\pi, 0) \end{cases}, \tag{3.65}$$

The phase distributions are plotted in Fig. 3.15, and Θ_π has much wider distribution than Θ_0 due to the signal-noise beating of the marks of OOK signals.

While the differential phase, $\Delta\Theta$, between two neighboring bits of a DPSK signal determines signal performance, the pdf of differential phase is required to evaluate a DPSK signal. Since the pdf of two neighboring bits are independent, the characteristic function of $\Delta\Theta$ is the product of the original and conjugate characteristic functions of Θ. As a result, the pdf of differential phase are,

$$p_{\Delta\Theta_{\pi\pi}}(\Delta\theta) = \frac{1}{2\pi} \sum_{m=-\infty}^{\infty} \left| \frac{\exp\left(\dfrac{j\pi m}{1 - j2\tilde{\sigma}^2 m}\right)}{1 - j2\tilde{\sigma}^2 m} \right|^2 e^{-jm\Delta\theta}, \tag{3.66}$$

$$p_{\Delta\Theta_{00}}(\Delta\theta) = \frac{1}{2\pi} \sum_{m=-\infty}^{\infty} \frac{1}{|1 - j2\tilde{\sigma}^2 m|^2} e^{-jm\Delta\theta}, \tag{3.67}$$

$$p_{\Delta\Theta_{\pi0}}(\Delta\theta) = \frac{1}{2\pi} \sum_{m=-\infty}^{\infty} \frac{\exp\left(\dfrac{j\pi m}{1 - j2\tilde{\sigma}^2 m}\right)}{|1 - j2\tilde{\sigma}^2 m|^2} e^{-jm\Delta\theta}, \tag{3.68}$$

$$p_{\Delta\Theta_{0\pi}}(\Delta\theta) = \frac{1}{2\pi} \sum_{m=-\infty}^{\infty} \frac{\exp\left(\dfrac{-j\pi m}{1 + j2\tilde{\sigma}^2 m}\right)}{|1 + j2\tilde{\sigma}^2 m|^2} e^{-jm\Delta\theta}. \tag{3.69}$$
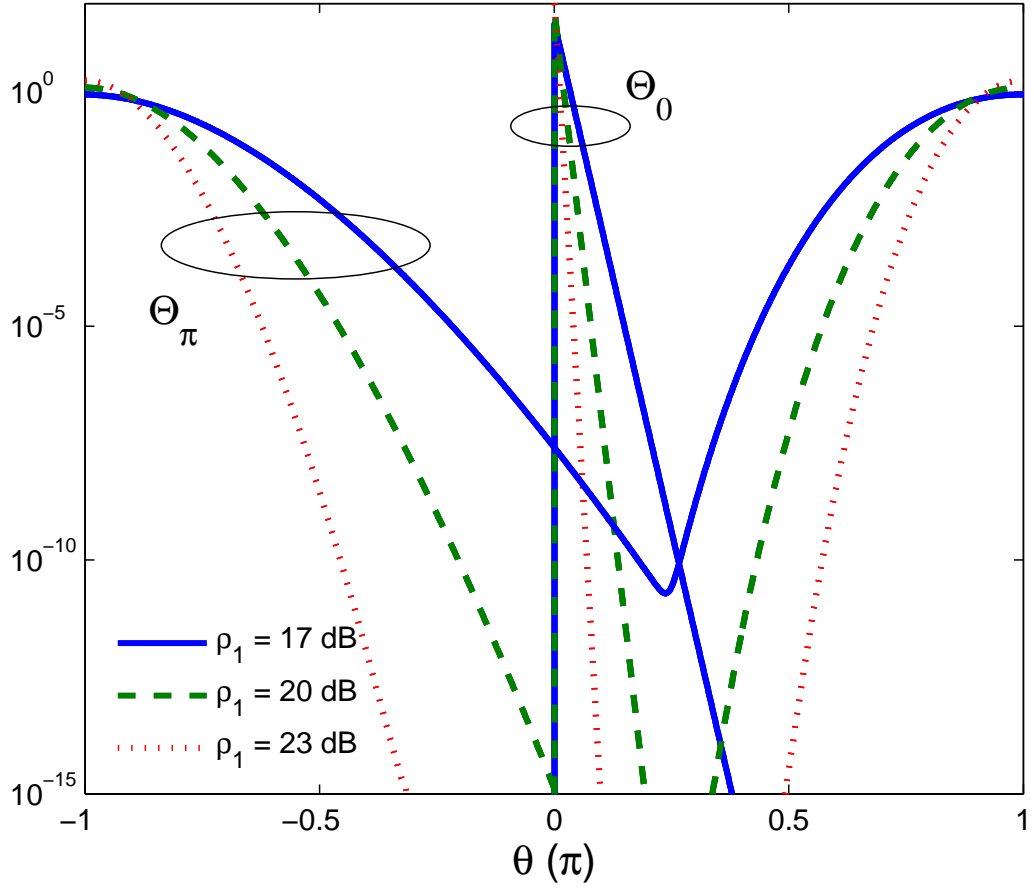
Figure 3.15: The phase distributions with different SNR of OOK signals

Therefore, the pdf of in-phase and out-of-phase differential phase can be represented as,

$$p_{\Delta\Theta_{\text{in}}}(\Delta\theta) = \frac{p_{\Delta\Theta_{\pi\pi}}(\Delta\theta) + p_{\Delta\Theta_{00}}(\Delta\theta)}{2} \tag{3.70}$$

$$= \frac{1}{2\pi} \sum_{m=-\infty}^{\infty} \Psi_{\text{in}}(m) e^{-jm\Delta\theta},$$

$$p_{\Delta\Theta_{\text{out}}}(\Delta\theta) = \frac{p_{\Delta\Theta_{\pi 0}}(\Delta\theta) + p_{\Delta\Theta_{0\pi}}(\Delta\theta)}{2}$$

$$= \frac{1}{2\pi} \sum_{m=-\infty}^{\infty} \Psi_{\text{out}}(m) e^{-jm\Delta\theta}. \tag{3.71}$$

where

$$\Psi_{\text{in}}(m) = \frac{1}{2} \left| \frac{\exp\left(\dfrac{j\pi m}{1 - j2\tilde{\sigma}^2 m}\right)}{1 - j2\tilde{\sigma}^2 m} \right|^2 + \frac{1}{2\left|1 - j2\tilde{\sigma}^2 m\right|^2},$$

$$\Psi_{\text{out}}(m) = \frac{\Re\left\{\exp\left(\dfrac{j\pi m}{1 - j2\tilde{\sigma}^2 m}\right)\right\}}{|1 + j2\tilde{\sigma}^2 m|^2} \, .$$

Similarly, because $|1 - j2\tilde{\sigma}^2 m|^{-2}$ converges slowly, by using the relation,

$$\frac{1}{2\pi} \int_{-\infty}^{\infty} \frac{1}{|1 - j2\tilde{\sigma}^2 t|^2} e^{-jyt} \, \mathrm{d}t = \frac{1}{4\tilde{\sigma}^2} e^{-\frac{|y|}{2\tilde{\sigma}^2}} \, ,$$

$p_{\Delta\Theta_{00}}$ can also be rewritten as,

$$
\begin{aligned}
p_{\Delta\Theta_{00}}(\Delta\theta) &= \frac{1}{4\tilde{\sigma}^2} \sum_{m=-\infty}^{\infty} e^{-\frac{|\Delta\theta - 2m\pi|}{2\tilde{\sigma}^2}} \\
&= \frac{1}{4\tilde{\sigma}^2} \left(e^{-\frac{|\Delta\theta|}{2\tilde{\sigma}^2}} + 2\cosh\left(\frac{\Delta\theta}{2\tilde{\sigma}^2}\right) \sum_{m=1}^{\infty} e^{-\frac{m\pi}{\tilde{\sigma}^2}} \right) \\
&= \frac{1}{4\tilde{\sigma}^2} \operatorname{csch}\left(\frac{\pi}{2\tilde{\sigma}^2}\right) \cosh\left(\frac{\pi - |\Delta\theta|}{2\tilde{\sigma}^2}\right) \, ,
\end{aligned}
\tag{3.72}
$$

which is much easier to be calculated numerically. Figure 3.16 shows the numerical results of differential phase distributions.

Since only PN is induced during the conversion process, the error probabilities caused by the finite SNR of the OOK signal can be obtained by,

$$p_e^{\text{in}} = 1 - \int_{-\xi}^{\xi} p_{\Delta\Theta_{\text{in}}}(\Delta\theta) \, \mathrm{d}\Delta\theta \, , \tag{3.73}$$

$$p_e^{\text{out}} = \int_{-\xi}^{\xi} p_{\Delta\Theta_{\text{out}}}(\Delta\theta) \, \mathrm{d}\Delta\theta \, , \tag{3.74}$$

where $\xi = \cos^{-1}(\bar{h}/A_2^2)$; $\bar{h}$ is the threshold, and A_2^2 is the power of the DPSK signal. According to Eqs. (3.44) and (3.70)-(3.72), the total error probability is,

$$p_e = \frac{1}{2} + \frac{1}{\pi} \sum_{m=1}^{\infty} \frac{\sin(m\xi)}{m} \left(\Psi_{\text{out}}(m) - \Psi_{\text{in}}(m) \right) \, . \tag{3.75}$$

Figure 3.17 shows the results of Eq. (3.75) with the conventional threshold of $\bar{h} = 0$ and the optimal threshold. The optimal threshold was obtained by minimizing Eq. (3.75) and it is about -20%. The minus threshold corresponds that $p_{\Delta\Theta_{\text{in}}}$ has longer tails, as shown in Fig. 3.16, although the penalty caused by setting $\bar{h} = 0$ is less than 1 dB. Moreover,
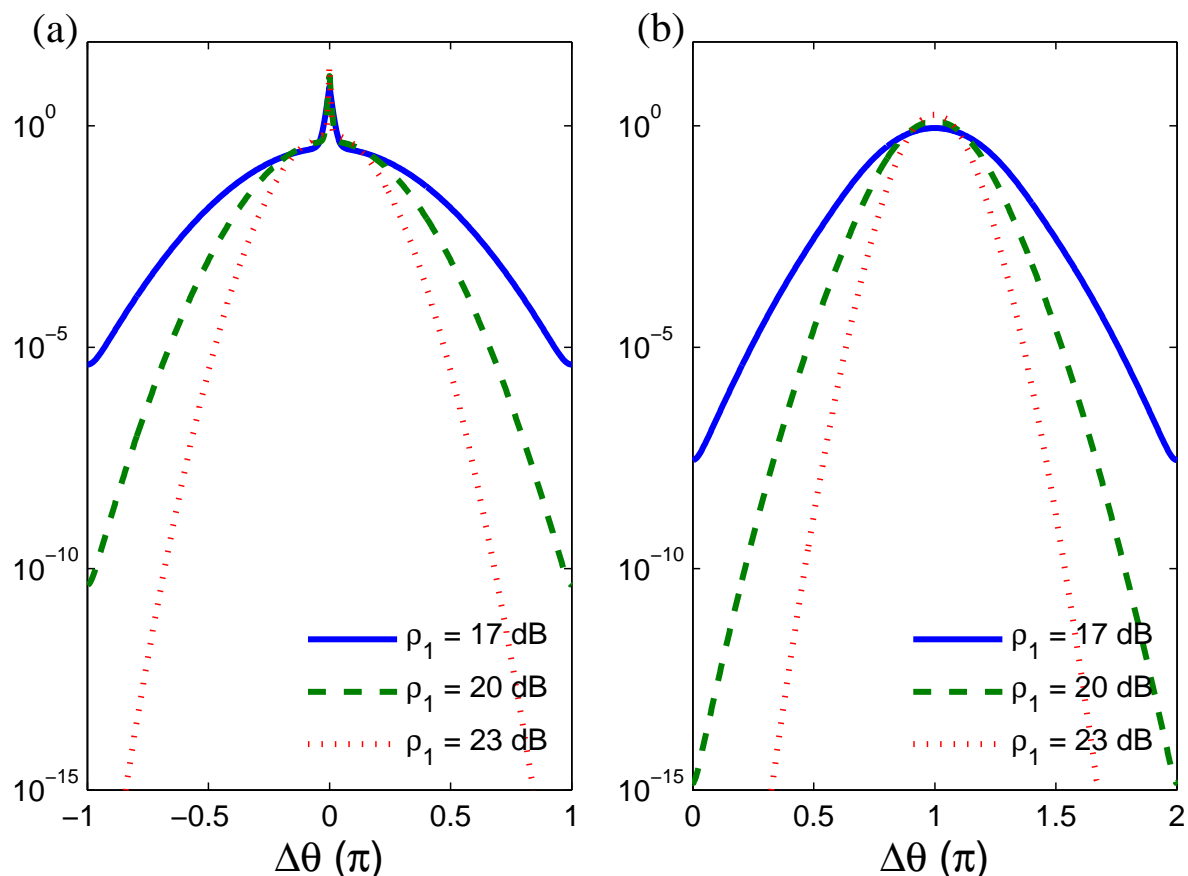
Figure 3.16: (a) In-phase and (b) out-of-phase differential phase distributions with different SNR of OOK signals

the sensitivity is 23.5 dB, and the DPSK signal can not achieve error free when the SNR of the OOK is lower than that. For comparison, the OOK signal of Eqs. (3.59) and (3.60) has the sensitivity of ~ 15.8 dB.

Actually, to evaluate a DPSK signal converted from an OOK signal with finite SNR, noise loading on the DPSK signal is required. Assuming the loaded noise is additive Gaussian noise with the variance of $2\sigma_n^2$, the SNR of the DPSK is $\rho_s = A_2^2/(2\sigma_n^2)$. The loaded noise will induces linear PN on the DPSK signal, and the pdf of this PN is [50],

$$p_{\Theta_n}(\vartheta) = \frac{1}{2\pi} \sum_{m=-\infty}^{\infty} \frac{\sqrt{\pi\rho_s}}{2} e^{-\frac{\rho_s}{2}} \Pi_m(\rho_s) e^{-jm\vartheta}, \qquad (3.76)$$
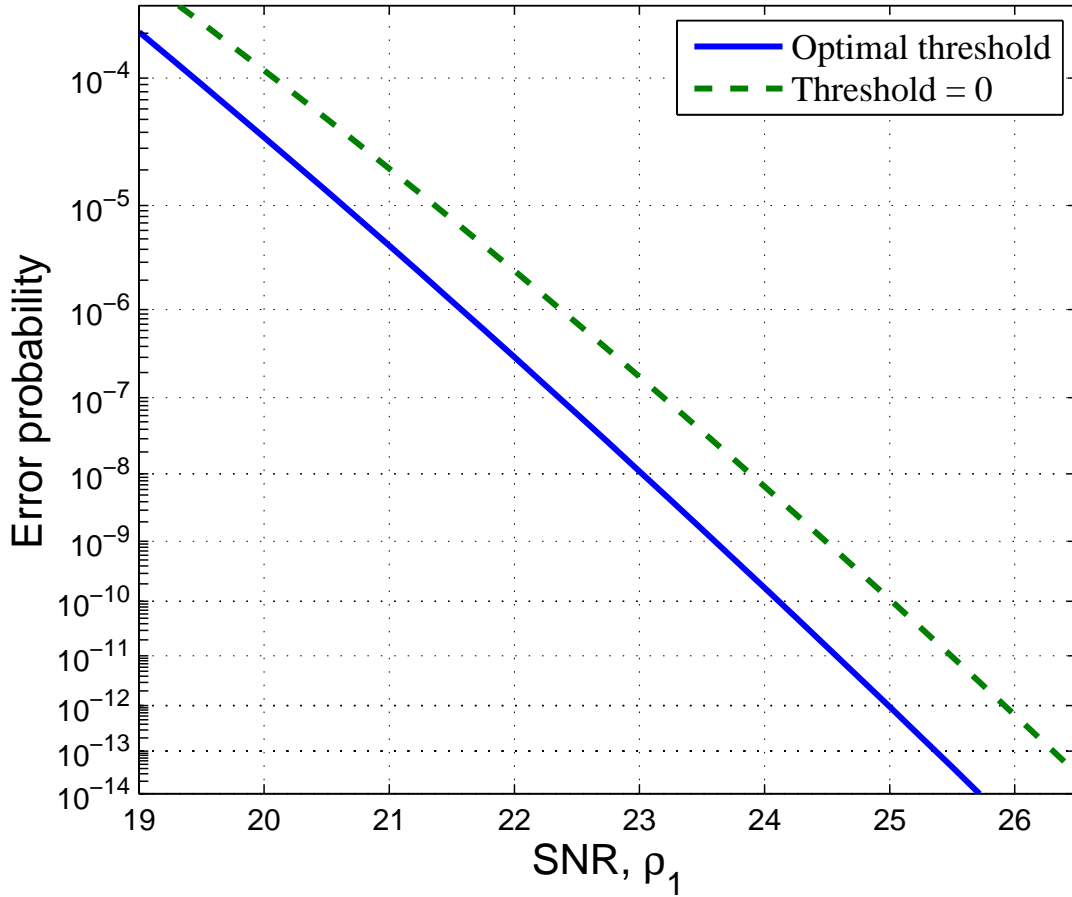
Figure 3.17: Error probability as a funciton of the finite SNR of the OOK signal

where

$$\Pi_m(\rho) = I_{\frac{m-1}{2}}\left(\frac{\rho}{2}\right) + I_{\frac{m+1}{2}}\left(\frac{\rho}{2}\right) . \tag{3.77}$$

Accordingly, the differential PN has the pdf,

$$p_{\Delta\Theta_n}(\Delta\vartheta) = \frac{1}{2\pi} \sum_{m=-\infty}^{\infty} \frac{\pi\rho_s}{4} e^{-\rho_s} \Pi_m^2(\rho_s) e^{-jm\Delta\vartheta} . \tag{3.78}$$

Considering both linear and nonlinear noise source, the pdf of the differential phase distributions, Eqs. (3.70) and (3.71), become,

$$p_{\Delta\Theta_{\mathrm{in},n}}(\Delta\theta) = \frac{\rho_s e^{-\rho_s}}{8} \sum_{m=-\infty}^{\infty} \Pi_m^2(\rho_s) \Psi_{\mathrm{in}}(m) e^{-jm\Delta\theta} , \tag{3.79}$$

$$p_{\Delta\Theta_{\mathrm{out},n}}(\Delta\theta) = \frac{\rho_s e^{-\rho_s}}{8} \sum_{m=-\infty}^{\infty} \Pi_m^2(\rho_s) \Psi_{\mathrm{out}}(m) e^{-jm\Delta\theta} . \tag{3.80}$$

71

Unfortunately, since AN is also generated after noise loading, Eqs. (3.73) and (3.74) can not be applied to Eqs. (3.79) and (3.80), except the threshold is set at 0. Therefore, while $\bar{h} = 0$, the error probability is,

$$p_{e,n0} = \frac{1}{2} + \frac{\rho_s e^{-\rho_s}}{4} \sum_{k=0}^{\infty} \frac{(-1)^k}{2k+1} \Pi_{2k+1}^2(\rho_s) \left(\Psi_{\text{out}}(2k+1) - \Psi_{\text{in}}(2k+1)\right). \qquad (3.81)$$

It is worth to note that when $\rho_1 = \infty$ ($\tilde{\sigma}^2 = 0$), Eq. (3.81) is equivalent to Eq. (3.53). On the other hand, if ρ_s is approaching infinity, Eq. (3.81) becomes Eq. (3.75). Furthermore, to calculate the error probability with an arbitrary threshold, a more troublesome method is needed. Similar to Eqs. (3.51) and (3.52), while the phase difference between neighboring bits is $\Delta\theta$, the error probabilities are,

$$
\begin{aligned}
\hat{p}_e^{\text{in}}(\Delta\theta) &= \frac{1}{2} e^{-2\rho_s \cos^2\left(\frac{\Delta\theta}{2}\right)} \int_0^{\infty} e^{-\frac{x}{2}} I_0\left(2\sqrt{\rho_s x} \cos\left(\frac{\Delta\theta}{2}\right)\right) \\
&\quad \times Q_1\left(2\sqrt{\rho_s} \left|\sin\left(\frac{\Delta\theta}{2}\right)\right|, \sqrt{x+h}\right) \mathrm{d}x \qquad (3.82) \\
&= \frac{1}{2} e^{-\rho_s - \frac{h}{2}} I_0\left(\rho_s \sin \Delta\theta\right) + e^{-\rho_s - \frac{h}{2}} \sum_{n=2}^{\infty} \mathbf{c}_n \tan^{n-1}\left(\frac{\Delta\theta}{2}\right) I_{n-1}\left(\rho_s \sin \Delta\theta\right),
\end{aligned}
$$

$$
\begin{aligned}
\hat{p}_e^{\text{out}}(\Delta\theta) &= 1 - \frac{1}{2} e^{-2\rho_s \cos^2\left(\frac{\Delta\theta}{2}\right)} \int_0^{\infty} e^{-\frac{x}{2}} I_0\left(2\sqrt{\rho_s x} \cos\left(\frac{\Delta\theta}{2}\right)\right) \\
&\quad \times Q_1\left(2\sqrt{\rho_s} \left|\sin\left(\frac{\Delta\theta}{2}\right)\right|, \sqrt{x+h}\right) \mathrm{d}x \qquad (3.83) \\
&= 1 - \frac{1}{2} e^{-\rho_s - \frac{h}{2}} I_0\left(\rho_s \sin \Delta\theta\right) - e^{-\rho_s - \frac{h}{2}} \sum_{n=2}^{\infty} \mathbf{c}_n \tan^{n-1}\left(\frac{\Delta\theta}{2}\right) I_{n-1}\left(\rho_s \sin \Delta\theta\right),
\end{aligned}
$$

where $h = -\bar{h}\sigma_n^2/2$ is assumed to be positive. Consequently, the total error probability can be written as,

$$
\begin{aligned}
p_{e,n} &= \left\langle \frac{\hat{p}_e^{\text{in}}(\Delta\theta) + \hat{p}_e^{\text{out}}(\Delta\theta)}{2} \right\rangle \qquad (3.84) \\
&= \frac{1}{2} \int_{-\pi}^{\pi} p_{\Delta\Theta_{\text{in}}}(\Delta\theta) \hat{p}_e^{\text{in}}(\Delta\theta) + p_{\Delta\Theta_{\text{out}}}(\Delta\theta) \hat{p}_e^{\text{out}}(\Delta\theta) \, \mathrm{d}\Delta\theta \\
&= \frac{1}{2} + \int_0^{\pi} \left(p_{\Delta\Theta_{\text{in}}}(\Delta\theta) - p_{\Delta\Theta_{\text{out}}}(\Delta\theta)\right) \hat{p}_e^{\text{in}}(\Delta\theta) \, \mathrm{d}\Delta\theta.
\end{aligned}
$$

Actually, since most of error might be contributed by the nonlinear PN, Eqs. (3.73) and

(3.74) might be used to estimate it,

$$p_{e,n} \cong \frac{1}{2} + \frac{\rho_s e^{-\rho_s}}{4} \sum_{m=1}^{\infty} \frac{\sin(m\xi)}{m} \Pi_m^2(\rho_2) \left(\Psi_{\text{out}}(m) - \Psi_{\text{in}}(m) \right) . \tag{3.85}$$

Figure 3.18 shows the comparison between Eqs. (3.84) and (3.85). Although the approximation underestimates the error probability due to omission of AN, the small difference between the exact and approximated ones implies that Eq. (3.85) is a good approximation. The error probability with $\bar{h} = 0$ is also plotted, and the penalties increase exponentially when ρ_1 is close to the critical values exhibited in Fig. 3.17.
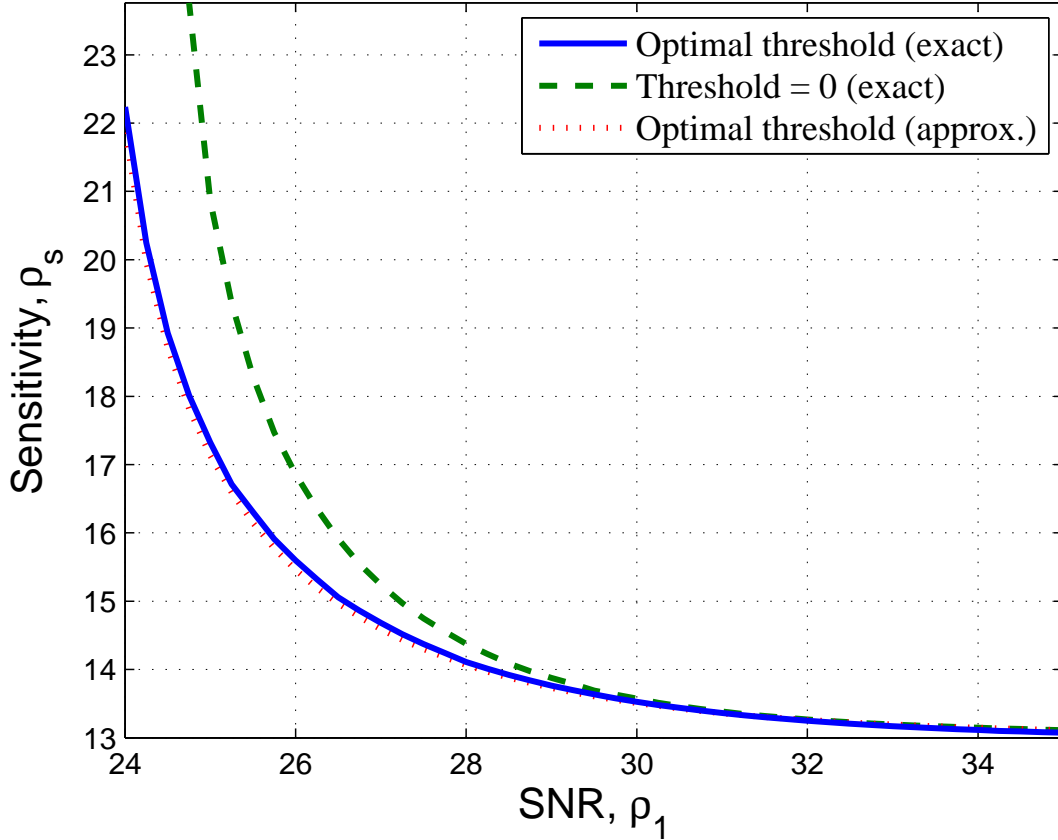
Figure 3.18: Sensitivity as a function of ρ_1

Chapter 4

All-optical phase noise suppression of DPSK signals

4.1   Introduction to the regeneration of DPSK signals

In recent years, the RZ-DPSK format has attracted much attention and become a promising format in long-haul high-speed optical communication systems [29] due to its superior sensitivity, higher nonlinear tolerance and higher spectral efficiency, compared with the traditional OOK format. However, because optical DPSK signal carries binary data on its phase domain, DPSK systems are limited by both AN and PN. Therefore, either PN or AN must be prevented from being accumulated to expand the reach of DPSK systems. Spectral inversion by phase conjugation [51][52] and post nonlinear phase-shift compensators [53][54] can reduce accumulated nonlinear PN. Although in-line filtering is a simple means of constraining PN by the stabilization of amplitude [55][56], in-line regenerators for DPSK signals are needed to manage either AN or PN and to further expand the transmission distance. Unfortunately, most of the all-optical regeneration schemes for the OOK format [15]-[17] are not suitable for the DPSK format, because these regenerators will distort its phase information. Phase-preserving amplitude regeneration has been proposed to reduce AN of DPSK signals but not to affect the phase of DPSK signals much [19][20]. While the amplitude of DPSK signals is managed by these phase-preserving regenerators, the nonlinear PN induced by nonlinear signal-noise beating can be reduced simultaneously [20]. However, existent PN will keep being accumulated due to the absence of phase management. Moreover, unlike power which can be detected

74

independently, phase is a relative parameter. Hence, a reference beam is needed to identify and regenerate phase information. A PSA which requires a coherent reference beam can eliminate both AN and PN simultaneously [18]. Unfortunately, if such a phase-locked coherent beam can be obtained practically, coherent-detection BPSK signals would have been adopted, instead of direct-detection DPSK signals. Another approach is to convert a DPSK signal to OOK signals (DB and AMI), and then convert the amplitude information of these signals to the phase of a probe beam [57][58]. The PN is suppressed due to nonlinear phase-to-intensity conversion in a DI [57] or amplitude regeneration of OOK signals [58]. However, because the amplitude data of these OOK signals are the differential code of phase data of the DPSK signal, the regenerative DPSK signal carries different data from original DPSK signal, and this should be avoided by precoding the data at the transmitter. Additionally, while the number of this kind of regenerators in the transmission is n, the precoding times must be $n + 1$.

In fact, since the DPSK signals are demodulated by a DI, what influences received signals is differential PN, instead of PN itself. Consequently, not only reducing PN, but also increasing the correlation between PN of neighboring pulses can improve signal performance. In the following sections, a novel PNA which can average the PN of adjacent pulses will be introduced. Both decreasing PN and increasing the correlation of PN of adjacent bits can be achieved simultaneously by averaging PN. Furthermore, the effects of PN averaging on linear and nonlinear PN are also investigated.

4.2   Concept and realization of phase noise averaging

The function of a PNA is to average the PN of one bit with that of its adjacent bit. Figure 4.1 presents a simple concept in the realization of a PNA. Based on an assumption

that all signals have a constant amplitude, E_0, each bit of the DPSK signals can be represented as, $E_n = s_n E_0 \exp(j\vartheta_n)$, where $s_n = \pm 1$ corresponds to a zero or π phase shift and ϑ_n is the PN of the n-th pulse. After one bit delay, if the logic of the delay data sequence can be modified to be equivalent to that of the original DPSK data, as shown in Fig. 4.1, then the sum of this modified signals and the original signals can be written as,

$$E_n' = 2s_n E_0 \cos\left(\frac{\vartheta_n - \vartheta_{n-1}}{2}\right) \times e^{j\frac{\vartheta_n + \vartheta_{n-1}}{2}} . \tag{4.1}$$

Therefore, the output field will have original information and contain averaged PN and minor AN converted from the differential PN. If ϑ_n and ϑ_{n-1} can be treated as independent noise with the same variance, σ^2, from Eq. (4.1), the variance of the output PN, $(\vartheta_n + \vartheta_{n-1})/2$, is $\sigma^2/2$. However, after demodulation via a DI, the received signals are influenced by the differential PN, $\Delta\vartheta_n = \vartheta_n - \vartheta_{n-1}$, not by the PN itself. Furthermore, the variance of the original differential PN is $2\sigma^2$, and the differential PN becomes $(\vartheta_n - \vartheta_{n-2})/2$ with the variance of $\sigma^2/2$ after this PNA is applied. Accordingly, the PNA can increase the correlation between the PN of neighboring bits and reduce the differential PN. The assumption of uncorrelated PN is not always correct for nonlinear PN, although linear PN of neighboring pulses caused by ASE noise can be treated as iid random variables. Therefore, how the PN averaging affects PN and differential PN should be investigated after understanding the characteristics of various PN.

Moreover, since the PN after an ideal PNA can be also written as,

$$\vartheta_n' = \frac{1}{2}\left[\binom{1}{0}\vartheta_n + \binom{1}{1}\vartheta_{n-1}\right] ,$$

the PN passing through PNAs twice becomes,

$$\vartheta_n^{(2)} = \frac{1}{2}\left\{\frac{1}{2}\left[\binom{1}{0}\vartheta_n + \binom{1}{1}\vartheta_{n-1}\right] + \frac{1}{2}\left[\binom{1}{0}\vartheta_{n-1} + \binom{1}{1}\vartheta_{n-2}\right]\right\}$$
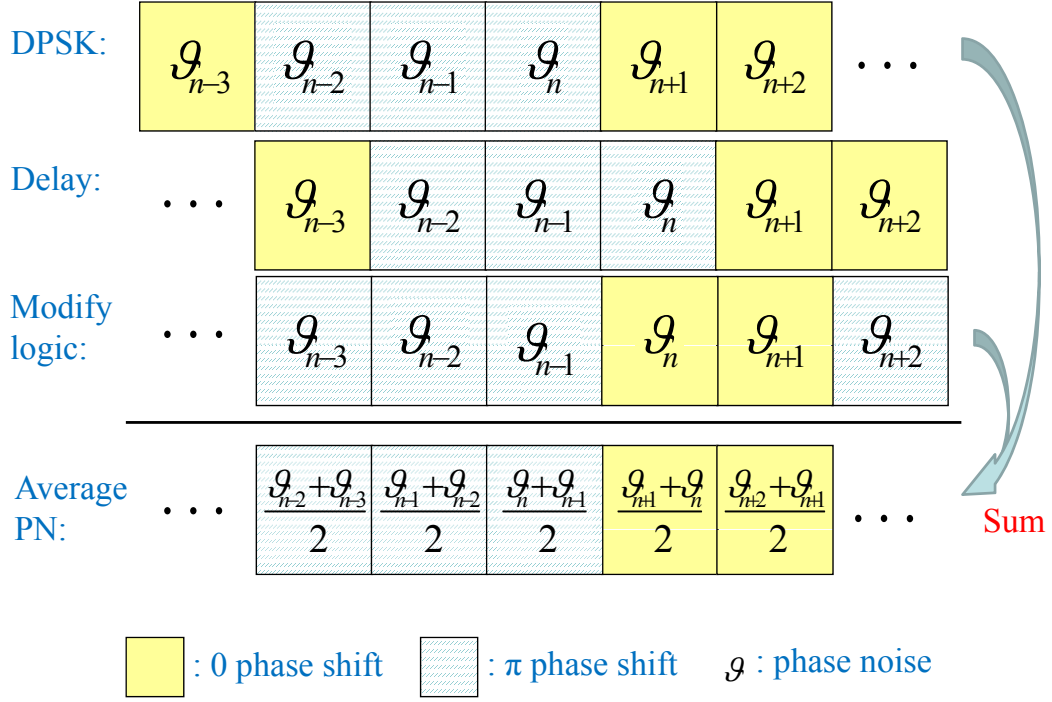
Figure 4.1: Concept of a PNA

$$= \frac{1}{2^2} \left[\binom{2}{0} \vartheta_n + \binom{2}{1} \vartheta_{n-1} + \binom{2}{2} \vartheta_{n-2} \right],$$

where the identity of binomial coefficients, $\binom{n+1}{k} = \binom{n}{k} + \binom{n}{k-1}$, is used. With the same processing, the PN after N PNAs is,

$$\vartheta_n^{(N)} = \frac{1}{2^N} \sum_{k=0}^{N} \binom{N}{k} \vartheta_{n-k} , \tag{4.2}$$

showing the multiple PN averaging effect.

Before discussing the types of PN and their properties, how to realize a PNA will be given in the following in advance. Figure. 4.2 shows the setup of a PNA, which is made up by a PSA. Considering only a PSA, in which a coherent pump beam, E_p, and a signal beam, E_s, are launched, the output field of the PSA is [18],

$$E_s' = e^{j\phi_0} \left(E_s \cos \phi_{\mathrm{nl}} - E_p \sin \phi_{\mathrm{nl}} \right) , \tag{4.3}$$

77
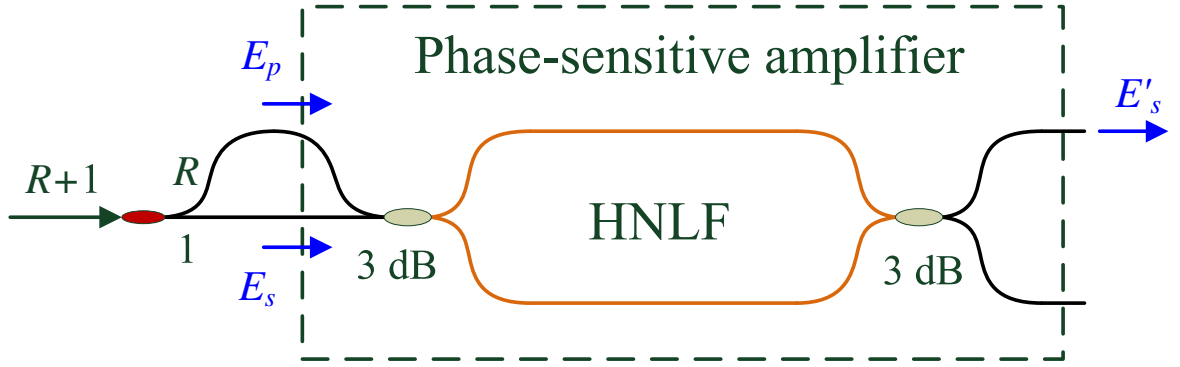
Figure 4.2: Setup of a PNA

where

$$\phi_0 = j\frac{\alpha L}{2} + \frac{\gamma L_{\text{eff}}\left(|E_s|^2 + |E_p|^2\right)}{2} , \qquad (4.4)$$

$$\phi_{\text{nl}} = \gamma L_{\text{eff}}|E_s||E_p|\sin\left(\phi_s - \phi_p\right) ; \qquad (4.5)$$

γ is the nonlinear coefficient of the HNLF; α denotes the fiber loss; L is the fiber length; L_{eff} is the effective fiber length, and ϕ_s and ϕ_p are the phases of signal and pump beams, respectively. Eq. (4.3) clearly reveals that the weighting term of E_p can modify its logic information to be identical with the data of the signal beam. Hence, the basic idea of phase regeneration is let the pump power much larger than signal power, and the output field is approximately proportional to $E_p \sin \phi_{\text{nl}}$, which implies the phase modulation of the coherent pump field is either 0 or π. Figure. 4.3 shows the results of Eq. (4.3), where $|E_p|^2/|E_s|^2 = 13$ dB and $\gamma L|E_p|^2 = \pi/2$, and it is obvious that the PSA works as a phase limiter.

The main difference between the proposed PNA and the conventional PSA is that a challenging phase-locking pump beam is not needed. The pump beam is replaced by the original signal beam with one bit delay and the power ratio of the pump beam to the signal beam is R, as shown in Fig. 4.2. When this PNA is put after an ideal
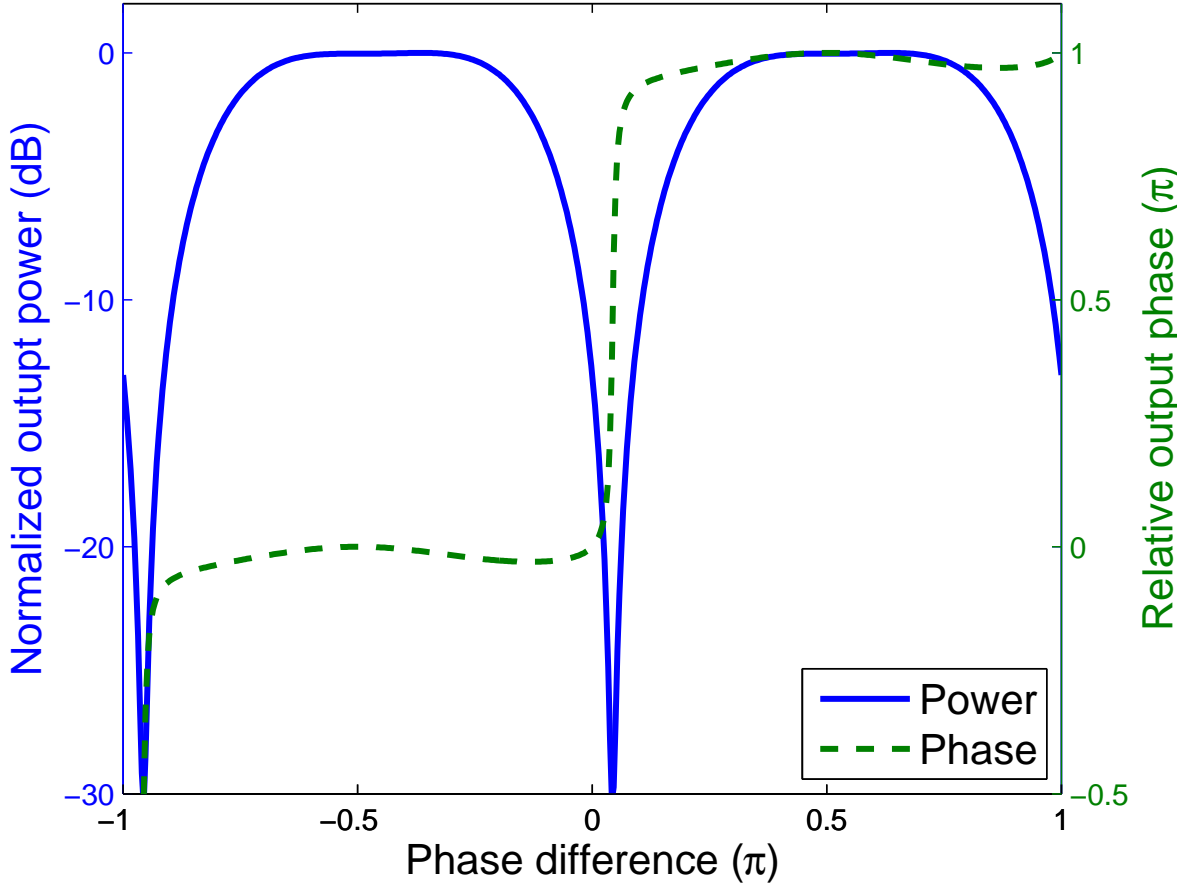
Figure 4.3: The output power and phase of a PSA

phase-preserving amplitude regenerator and the pump beam can be represent as $E_p = s_{n-1}E_0\sqrt{R}\exp(j\vartheta_{n-1})$, the output filed becomes,

$$E'_s = e^{j\phi_0}\left(e^{j\vartheta_n} - \Gamma_n\sqrt{R}\tan\phi_{\mathrm{nl}}\right) \times s_n E_0 \cos\phi_{\mathrm{nl}}e^{j\vartheta_{n-1}}, \qquad (4.6)$$

where $\Gamma_n = s_n/s_{n-1} = \pm 1$. Hence, Γ_n represents that the signal beam and pump beam are in-phase or out-of-phase. That is, $\sin(\phi_s - \phi_p)$ can be written as $\Gamma_n \times \sin\Delta\vartheta_n$. As a result, Eq. (4.6) can be rewritten as,

$$E'_s = e^{j\phi_0}\left(e^{j\vartheta_n} - \sqrt{R}\tan\vartheta_{\mathrm{nl}}\right) \times s_n E_0 \cos\vartheta_{\mathrm{nl}}e^{j\vartheta_{n-1}}, \qquad (4.7)$$

where $\vartheta_{\mathrm{nl}} = \Phi\sqrt{R}\sin\Delta\vartheta_n$ and $\Phi = \gamma L_{\mathrm{eff}}|E_s|^2$. Considering the first-order approximation of trigonometric functions, the bracket in Eq. (4.7) is the only part related to the

79

differential PN and can be rewritten as,

$$\tilde{E}'_s = e^{j\vartheta_n} - \Phi R \sin \Delta\vartheta_n \,. \qquad (4.8)$$

Moreover, the operating points can be derived from two conditions to yield the desired function of a PNA:

$$\frac{\partial \angle \tilde{E}'_s}{\partial \Delta\vartheta_n} = \frac{1}{2}\,, \qquad \frac{\partial |\tilde{E}'_s|^2}{\partial \Delta\vartheta_n} = 0 \,. \qquad (4.9)$$

The first part of Eq. (4.9) guarantees that the PNA can average the PN and the second part minimizes the output AN induced by differential PN. Hence, from Eqs. (4.8) and (4.9), the operating points are

$$\Phi R = \frac{1}{\sqrt{2}}\,, \qquad \Delta\phi_Q = -\tan^{-1}\sqrt{2}\,, \qquad (4.10)$$

where the second one is the required phase difference between the signal arm and the pump arm. Setting $R = 10$ dB and $\Phi = 0.071$, Figs. 4.4(a)-(c) presents the normalized output power, output phase and output phase slope of this PSA-based PNA, respectively. Therefore, when the splitting ratio of the first coupler in Fig. 4 is selected and a fixed phase difference between the two arms is given, a PSA can function as a PNA.

4.3 Capacity of phase noise averaging

4.3.1 Nonlinear phase noise

Besides linear PN, the nonlinear PN can be classified into several categories, as shown in Fig. 4.5. In WDM systems, the inter-channel nonlinearities occur between different wavelength channels, and intra-channel effects indicate those occur inside each channel. Since each channel contains the signal and ASE noise, the nonlinear interactions can be noise-noise beating, signal-noise beating, or signal-signal beating. In general, noise-noise
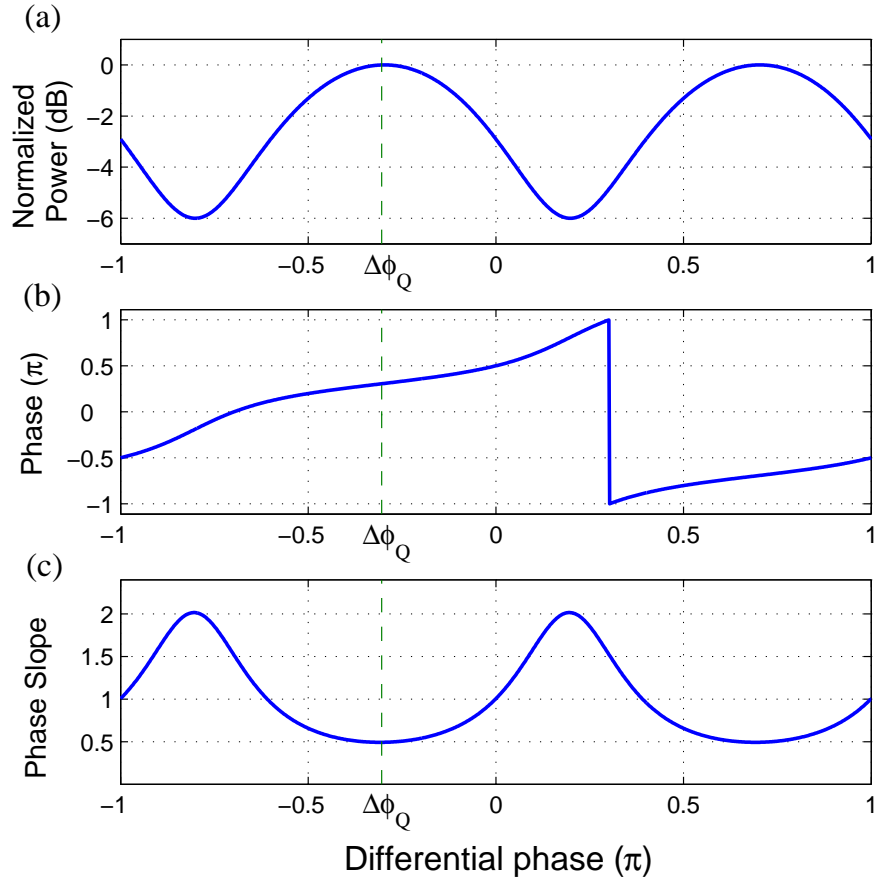
Figure 4.4: (a) Normalized output power, (b) output phase and (c) output phase slope of a PNA

beating can be neglected due to much smaller power of ASE noise, and phase shifts generated by signal-noise beating and signal-signal beating are the main contributions to nonlinear PN. Actually, the impairment caused by signal-signal beating is deterministic, instead of random. Nevertheless, it shows almost random statistics due to the random binary data of optical pulses, and accordingly, this deterministic nonlinear phase shift is still called nonlinear PN to avoid complexity of naming.

4.3.2 Multiple PN averaging effect

In different systems, different types of nonlinear PN will show different weightiness. To simplify the discussion, a usual transmission line with periodical full dispersion-
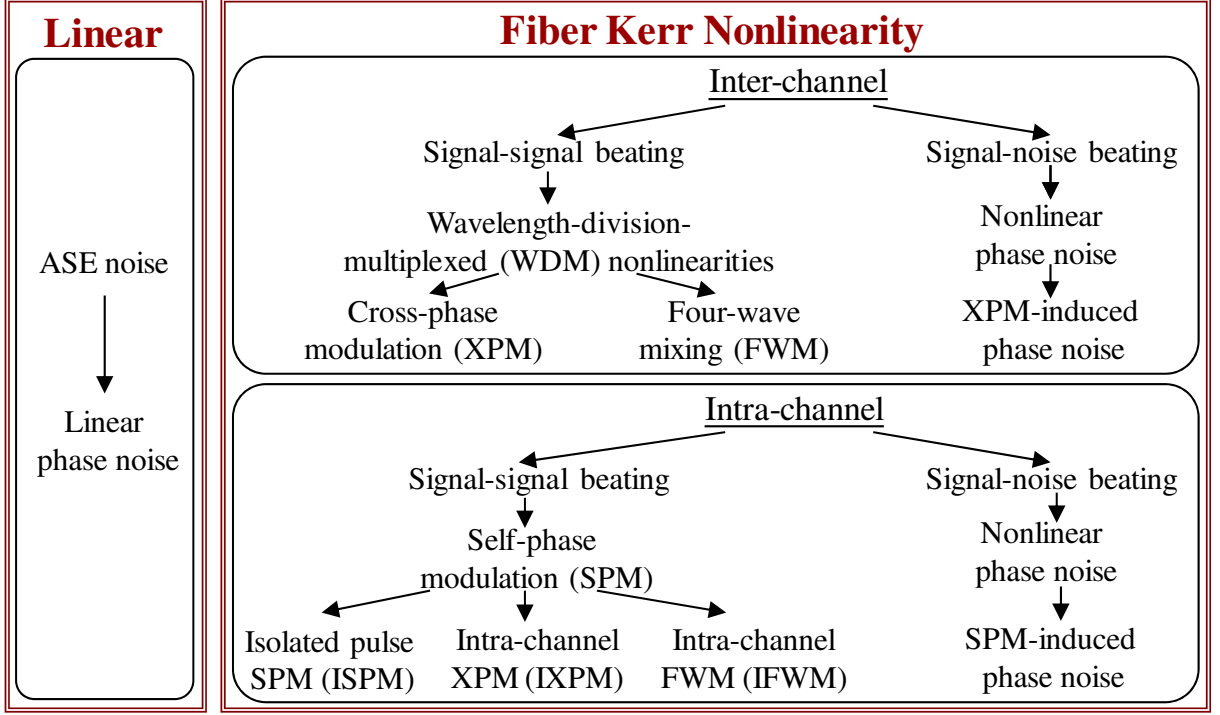
Figure 4.5: Classification of phase impairments

compensation is considered. In Fig. 4.6, a phase-preserving amplitude regenerator and a PNA are arranged following the transmission of K spans, which consist of standard single mode fibers (SSMF), dispersion compensating fibers (DCF) and EDFAs. If PNAs are not inserted, this system is called an amplitude-managed system, and PN will be accumulated [20]. Since the DPSK signal will pass through multiple PNAs in Fig. 4.6, the multiple PN averaging effect must be derived. The multiple PN averaging effect equivalent to Fig. 4.6 is schematically plotted in Fig. 4.7, in which $\vartheta_{N,n}$ represents the PN of n-th pulse created between $(N-1)$-th and N-th PNAs. As a result, according to Eq. (4.2), the total PN at the receiver is,

$$\Theta_n = \sum_{N=1}^{M} \vartheta_{N,n}^{(1+M-N)} = \sum_{N=1}^{M} \sum_{k=0}^{1+M-N} \frac{1}{2^{1+M-N}} \binom{1+M-N}{k} \vartheta_{N,n-k}, \qquad (4.11)$$

and it is influenced by the relations between PNs created in different spans and between PNs of different pulses. Furthermore, the differential PN can be represented as,

$$\Delta\Theta_n = \sum_{N=1}^{M} \sum_{k=0}^{N+1} a_{N,k} \cdot \vartheta_{1+M-N,n-k} \,, \tag{4.12}$$

where

$$a_{N,k} = \frac{1}{2^N} \left[\binom{N}{k} - \binom{N}{k-1} \right].$$
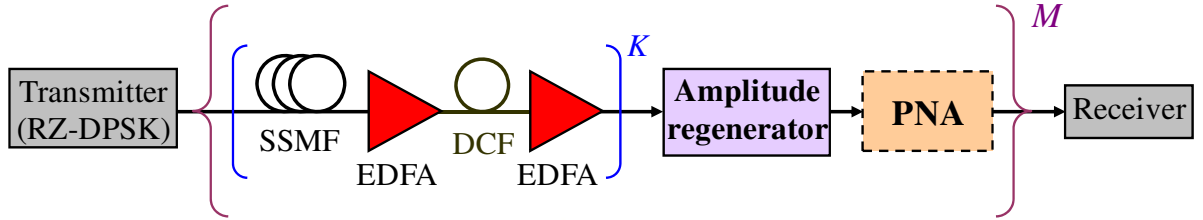
Figure 4.6: Optical DPSK transmission system with amplitude regenerators and PNAs inserted every K spans.
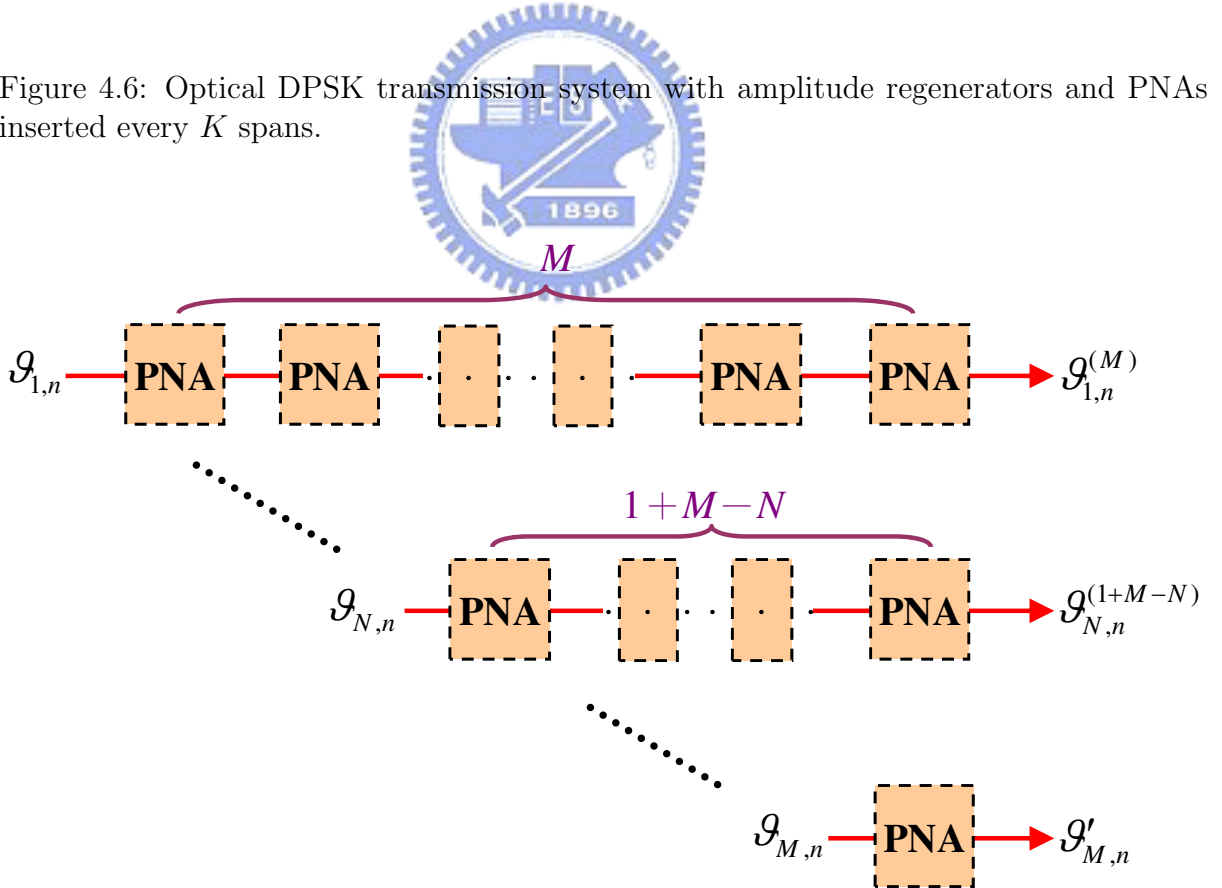
Figure 4.7: Multiple PN averaging effect in the transmission system

4.3.2.1 Random phase noise

Random PN consists of linear PN and nonlinear PN induced by signal-noise beating. Although linear PNs of each pulse are independent, nonlinear PNs of neighboring pulses could be correlated due to chromatic dispersion [59]. Nevertheless, due to amplitude regenerators inserted periodically to remove AN, random nonlinear PNs created in different regeneration span are induced by the ANs from different noise sources and can be treated as independent. In other words, $\vartheta_{N,n}$ and $\vartheta_{L,n}$ are independent, but $\vartheta_{N,n}$ and $\vartheta_{N,l}$ could be correlative. Hence, the correlation relation can be described as,

$$\langle \vartheta_{N,n} \times \vartheta_{L,l} \rangle = \delta_{N,L} \times C_{n-l} \times \sigma_r^2 \,, \tag{4.13}$$

where $\delta_{m,n}$ is the Kronecker Delta function; $C_k = C_{-k}$ is the correlation coefficient between the PNs of two pulses away from k bits and $\sigma_r^2 = \langle \vartheta_{N,n}^2 \rangle$ is the variance of random PN. By Eqs. (4.12) and (4.13), the variance of total differential PN is,

$$\langle \Delta \Theta^2 \rangle = \left(\sum_k \mathfrak{A}_k \times C_k \right) \times \sigma_r^2 \,, \tag{4.14}$$

where
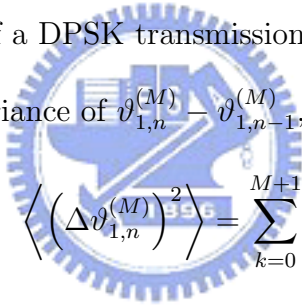
$$\mathfrak{A}_k = \sum_{N=1}^{M} a_{N,k} \otimes a_{N,-k}$$
$$= \sum_{N=1}^{M} \frac{1}{2^{2N}} \left[2 \times \binom{2N}{N+k} - \binom{2N}{N+k+1} - \binom{2N}{N+k-1} \right]$$
$$= 2\delta_{0,k} + \delta_{1,k} + \delta_{-1,k} - 4 \times \frac{1}{2^{2M+2}} \binom{2M+2}{M+k+1} \,,$$

and $\otimes$ denotes convolution. Since the last term of $\mathfrak{A}_k$ is a binomial distribution and C_k generally becomes smaller as $|k|$ is increasing, the variance in Eq. (4.14) is monotonically increasing as enlarging M. When M approaches infinity, $\langle \Delta \Theta^2 \rangle$ converges to $2(1+C_1)\sigma_r^2$. For comparison, without inserting PNA to suppress random PN, $\langle \Delta \Theta^2 \rangle$ becomes $2M(1-C_1)\sigma_r^2$, which is proportional to M.

Actually, while phase-preserving amplitude regenerators are inserted periodically to manage AN, the random PN is mainly contributed by linear PN. Furthermore, while the signal bit rate is high, nonlinear random PN would also be suppressed further by pulse broadening [60]. In this situation, C_k can be approximated as $\delta_{0,k}$, and the variance becomes,

$$\left\langle \Delta\Theta^2 \right\rangle = \left[2 - \frac{1}{4^M}\begin{pmatrix} 2M+2 \\ M+1 \end{pmatrix} \right] \times \sigma_r^2 . \tag{4.15}$$

This indicates that the total differential random PN will never exceed that before the first averager. Based on Eq. (4.15), Fig. 4.8 illustrates the variances of differential linear PN with and without PNAs. Figure 4.8 clearly shows that the equivalent accumulated PN never exceeds that generated in every K spans. It guarantees that the accumulated linear PN will not limit the reach of a DPSK transmission system with amplitude regenerators and PNAs. Moreover, the variance of $\vartheta_{1,n}^{(M)} - \vartheta_{1,n-1}^{(M)}$,

$$\left\langle \left(\Delta\vartheta_{1,n}^{(M)} \right)^2 \right\rangle = \sum_{k=0}^{M+1} a_{M,k}^2 , \tag{4.16}$$

is also shown in the figure to demonstrate the effect of multiple PN averaging.

4.3.2.2   Deterministic phase noise

While the deterministic nonlinear PN is induced by signal-signal beating, the PN generated in all spans are identical and add coherently span after span as the worst case, if chromatic dispersion of each channel is fully compensated by DCF at the end of each span. Therefore, similar to Eq. (4.13), the correlation relation between deterministic PN can be represented as,

$$\left\langle \vartheta_{N,n} \times \vartheta_{L,l} \right\rangle = \hat{C}_{n-l} \times \sigma_d^2 , \tag{4.17}$$
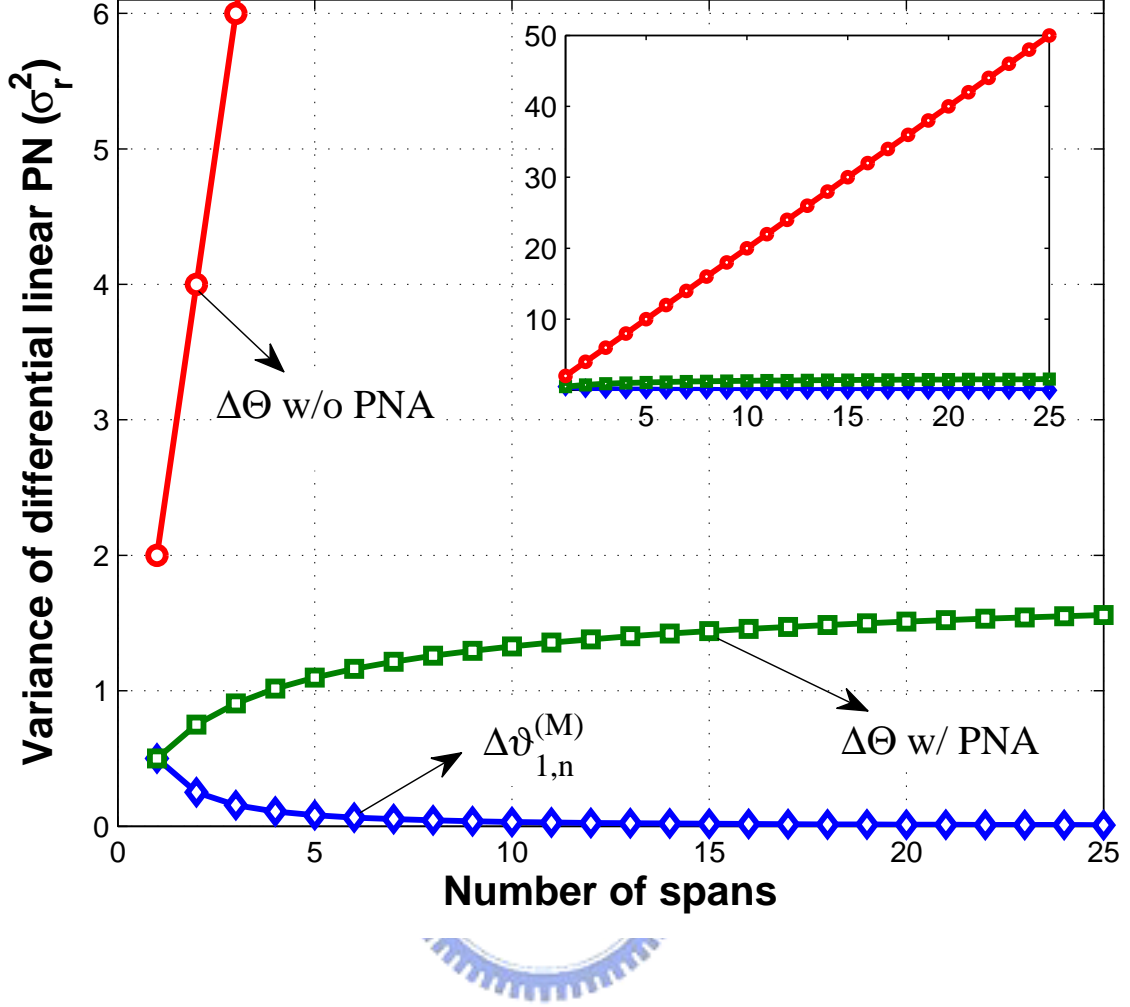
Figure 4.8: The variances of differential linear PN as functions of the number of PNAs

where $\hat{C}_k$ is the correlation coefficient and σ_d^2 is the variance of deterministic PN. Due to $\vartheta_{N,n} = \vartheta_n$, Eq. (4.12) can be rewritten as,

$$\Delta\Theta_n = \sum_{k=0}^{M+1} \left(\sum_{N=1}^{M} a_{N,k} \right) \cdot \vartheta_{n-k}\,. \qquad (4.18)$$

As a result, the variance of total deterministic PN is,

$$\langle \Delta\Theta^2 \rangle = \left(\sum_k \mathfrak{B}_k \times \hat{C}_k \right) \times \sigma_r^2\,, \qquad (4.19)$$

where

$$\mathfrak{B}_k = \left(\sum_{N=1}^{M} a_{N,k} \right) \otimes \left(\sum_{N=1}^{M} a_{N,-k} \right)$$

$$= \left[\delta_{0,k} + \delta_{1,k} - \frac{1}{2^M} \binom{M+1}{k} \right] \otimes \left[\delta_{0,-k} + \delta_{1,-k} - \frac{1}{2^M} \binom{M+1}{-k} \right]$$

$$= 2\delta_{0,k} + \delta_{1,k} + \delta_{-1,k}$$

$$+ 4 \left[\frac{1}{2^{2M+2}} \binom{2M+2}{M+k+1} - \frac{1}{2^{M+2}} \binom{M+2}{k+1} - \frac{1}{2^{M+2}} \binom{M+2}{-k+1} \right],$$

The last three terms in $\mathfrak{B}_k$ could be viewed as the binomial distributions centered at $k = 0$, $N/2$ and $-N/2$, with the variances of $(N+1)/2$, $(N+2)/4$ and $(N+2)/4$, respectively. Then $\langle \Delta \Theta^2 \rangle$ is expected to approach a maximum value, when the first binomial distribution contributes the most to the product in Eq. (4.19), but the second and the third terms contribute little. Moreover, if two pulses are far from each other in the time domain, the correlation between their PNs should be zero. Consequently, as M is large, the main contribution to the differential PN is $2\delta_{0,k} + \delta_{1,k} + \delta_{-1,k}$ of $\mathfrak{B}_k$. That is, $\langle \Delta \Theta^2 \rangle$ converges to $2(1 + \hat{C}_1)\sigma_d^2$ as $M \to \infty$. If PNAs are not inserted, $\langle \Delta \Theta^2 \rangle$ becomes $2M^2(1 - C_1)\sigma_d^2$, which accumulates at an accelerated rate due to coherent characteristics of PN and is not improved by inserting phase-preserving amplitude regenerators.

Moreover, with respect to high-speed transmissions (> 10 Gbps) in SSMF with dispersion of 17 ps/nm/km, the inter-channel nonlinearity affects systems much less than intra-channel nonlinearity due to fast walk-off between channels and pulse broadening. Among intra-channel effects, isolated pulse SPM (ISPM) and intra-channel XPM (IXPM) only induce identical deterministic nonlinear PN to each pulse, owing to the same power of pulses. Hence, in amplitude-managed highly dispersed RZ-DPSK systems, the nonlinear PN induced by intra-channel FWM (IFWM) is the main contribution to deterministic PN, and the correlation coefficient of IFWM-induced PN is necessary to understand in detail the effect of periodic PN averaging on deterministic PN. To simplify the analysis, the nonlinear effect is treated as a perturbation, and the optical field of n-th pulse of

RZ-DPSK singal is assumed to be,

$$u_n(t) = s_n\sqrt{P} \exp\left[-\frac{(t + nT)^2}{2\tau^2}\right] , \tag{4.20}$$

where 1.66τ is the FWHM. In previous works [61][62], nonlinearity of DCF was neglected. However, it significantly influences the characteristics of IFWM-induced PN, and especially the correlation between the PNs of neighboring bits. Accordingly, the analysis is extended to the nonlinear effects from both SSMF and DCF. Following some manipulation, the nonlinear PN can be represented as,

$$\vartheta_n = \sum_{l,m} s_l s_m s_n s_{l+m-n} \left[\gamma_1 P_1 F_{l,m}(L_1, \alpha_1, \beta_1'') - \gamma_2 P_2 e^{-\alpha_2 L_2} F_{l,m}(L_2, \alpha_2, \beta_2'')\right] , \tag{4.21}$$

where γ_i, P_i, L_i, α_i and β_i'' are the nonlinear coefficients, the launch peak power, the length, the loss and the GVD parameter of SSMF $(i = 1)$ and DCF $(i = 2)$; $\beta_1'' L_1 = \beta_2'' L2$ is required for complete dispersion compensating, and $F_{l,m}(L, \alpha, \beta'')$ is,

$$F_{l,m}(L, \alpha, \beta'') = \Re\left\{\int_0^L \frac{e^{-\alpha z}}{\sqrt{1 + j2\frac{\beta'' z}{\tau^2} + 3\left(\frac{\beta'' z}{\tau^2}\right)^2}}\right. \tag{4.22}$$

$$\left. \times \exp\left\{-\left(\frac{T}{\tau}\right)^2 \left[\frac{3lm}{1 + j3\frac{\beta'' z}{\tau^2}} + \frac{(l - m)^2}{1 + j2\frac{\beta'' z}{\tau^2} + 3\left(\frac{\beta'' z}{\tau^2}\right)^2}\right]\right\}\mathrm{d}z\right\} ,$$

giving the strength of the nonlinear effect from l-th, m-th and $(l + m)$-th pulses. The first and second terms of Eq. (4.21) represent the nonlinear effects occurring in SSMF and DCF, respectively.

To investigate the IFWM-induced PN of a specific system, 40 Gbps RZ-DPSK signals with a 33% duty cycle are considered; the length of in each span is 80 km; the nonlinear coefficients, the loss and the GVD parameters of SSMF and DCF are 1.3 and 5.4 W^{-1}km^{-1}, 0.2 and 0.65 dB/km, and -21.7 and 127.6 ps^2/km, respectively. The launch power of DCF is 7 dB lower than that of SSMF, and these values are chosen such that the mean nonlinear phase shift, $\Phi_{\mathrm{nl}} = N\gamma_1 P_{1,\mathrm{ave}} L_{1,\mathrm{eff}} + N\gamma_2 P_{2,\mathrm{ave}} L_{2,\mathrm{eff}}$, to a specific value,

where $L_{i,\text{eff}}$ is the effective length per span and $P_{i,\text{ave}} = \sqrt{\pi} P_i \tau / T$ is the average launch power. Since the pulses are highly broadened when sent into DCF, two pulses will interact even though these pulses are far away from each other. Hence, all distributions of $-22 \le l, m, l+m \le 22$ in Eq. (4.21) are considered to fully capture pulse-to-pulse interactions, and $l \ne n$ and $m \ne n$ are set to exclude ISPM and IXPM effects. With a De Bruijn sequence of 2^{16} bits and $\Phi_{\text{nl}} = 1$ rad after 40 spans, Figs. 4.9(a)-(c) depict the distributions of nonlinear PN caused by nonlinearities of both SSMF and DCF, only SSMF, and only DCF, respectively. These figures clearly show that the strength of nonlinear effect in DCF is not such small to be able to be neglected. The correlation coefficients of IFWM-induced PN are also plotted in Fig. 4.10, and the nonlinearity of DCF could increase the correlation of PNs of remote pulses but decrease that of adjoining pulses.

Based on the results of Fig. 4.10 and Eq. (4.17) and the setup of Fig. 4.6 with $K = 1$ and without amplitude regenerators, Fig. 4.11 analytically plots the variance of differential PN as a function of the number of the spans. The variance is maximal near 20 spans, and converges to about $3\sigma_d^2$ very slowly. Figure 4.11 also plots the results of a numerical simulation to verify the effect of PN averaging. All of the parameters of the simulation are identical to those in Fig. 1, and ASE noise is neglected to focus on the pattern effect. When the number of spans is less than 20, the theory agrees excellently with the simulation. Since the amplitude of the signals is not regenerated in the simulation, the IFWM-induced AN generates additional nonlinear PN increasingly. Therefore, for $N > 35$, $\langle \Delta \Theta^2 \rangle$ with PNAs begins to increase rather than decrease. However, if ideal phase-preserving amplitude regenerators are inserted behind each span, then the simulation results would be identical to the theoretical results. Furthermore, both the results without PNA in Fig. 4.11 agree that increases as the square of the distance.
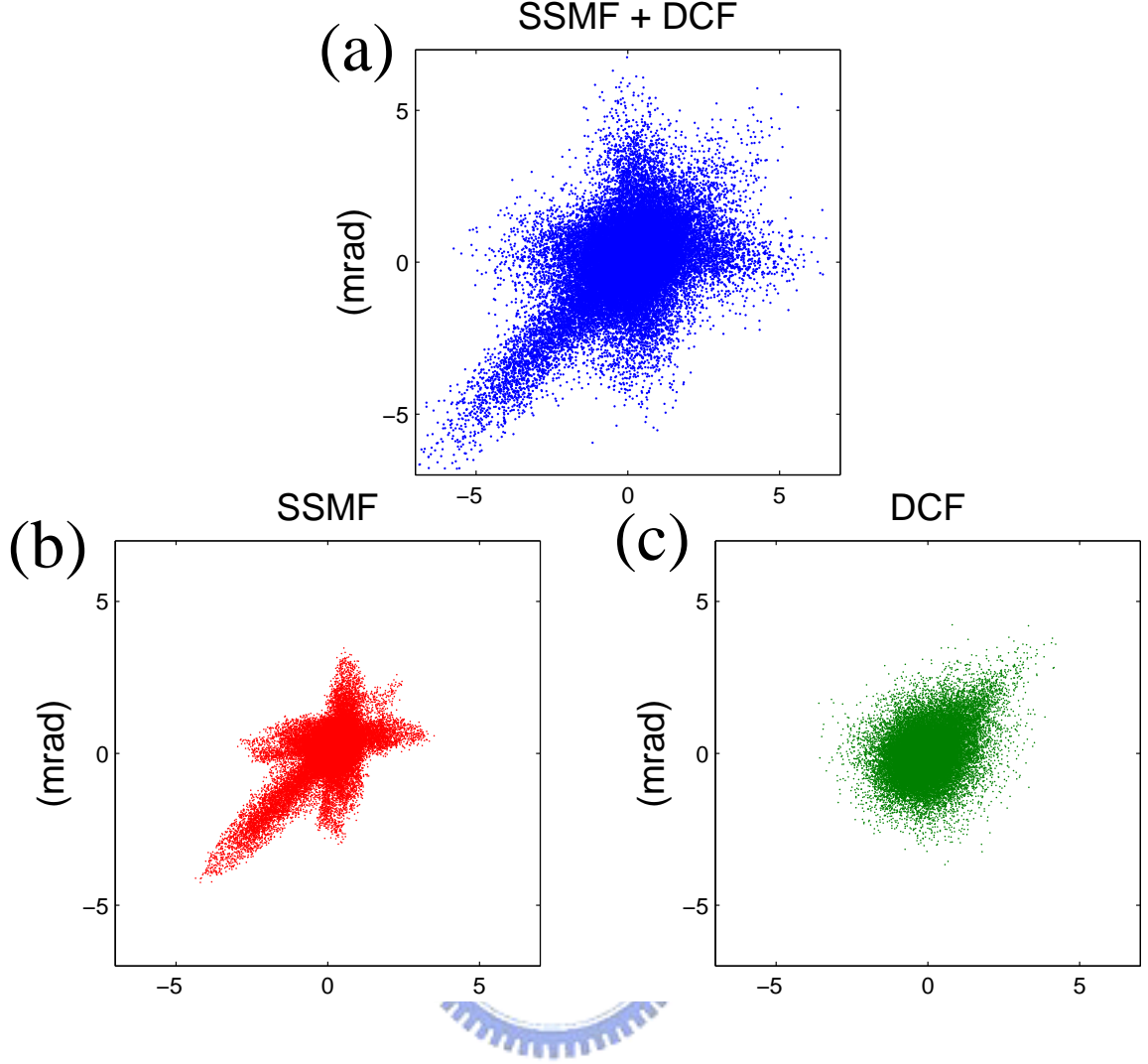
Figure 4.9: The distributions of IFWM-induced PN, ϑ_n and ϑ_{n-1}, generated in (a) SSMF and DCF (b) only SSMF, and (c) only DCF

To further investigate the effect of PN averaging on reducing nonlinear impairment, a semi-analytical method is used to compute the error probability and the nonlinear penalties. Based on Eq. (3.54) and previous work [62], the error probability related to an SNR, ρ_s, and the nonlinear differential PN is equal to,

$$p_e = \left\langle Q_1\left(2\sqrt{\rho_s}\left|\sin\left(\frac{\Delta\Theta}{2}\right)\right|, 2\sqrt{\rho_s}\left|\cos\left(\frac{\Delta\Theta}{2}\right)\right|\right) - \frac{1}{2}e^{-\rho_s}I_0\left(\rho_s|\sin\Delta\Theta|\right)\right\rangle. \quad (4.23)$$

The error probability curves as functions of SNR with different IFWM-induced PNs are calculated based on Eqs. (4.21)-(4.23), and the conditions of $\Phi_{nl} = 1$, 3 and 5 rad after 40 spans with and without PNAs are both plotted in Fig. 4.12. For comparison, the baseline
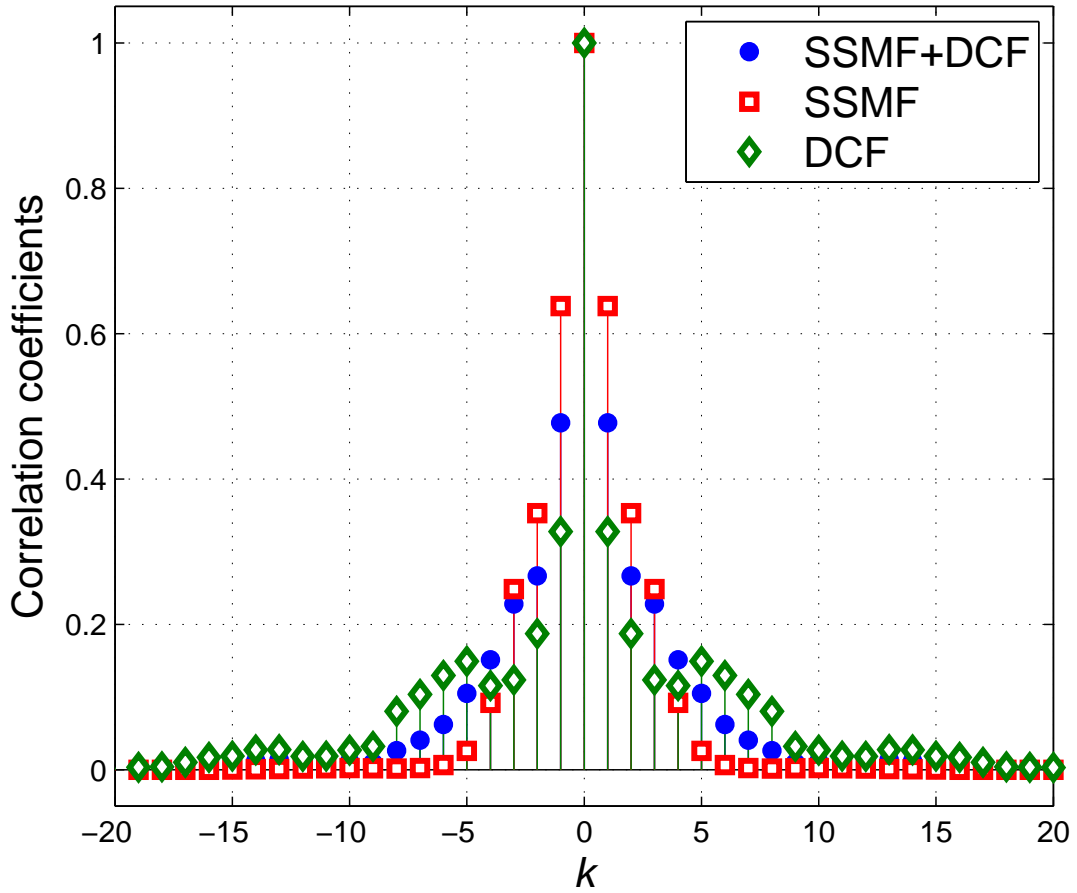
Figure 4.10: The correlation coefficients of the IFWM-induced PN

shown in Fig. 4.12 is the error probability without the PN of $e^{-\rho_s}/2$. Note that all the error probabilities with periodic PN averaging overlap the baseline and this fact indicates that the nonlinear penalty is negligible. Moreover, both increasing the transmission distance and the launch power will increase Φ_{nl}, and therefore degrade DPSK signals increasingly. In addition, longer sequences (up to 2^{24}) are tested in calculating both $\hat{C}_k$ and the error probability, and the results do not change significantly with the length of the pulse train as it exceeds 2^{16}.
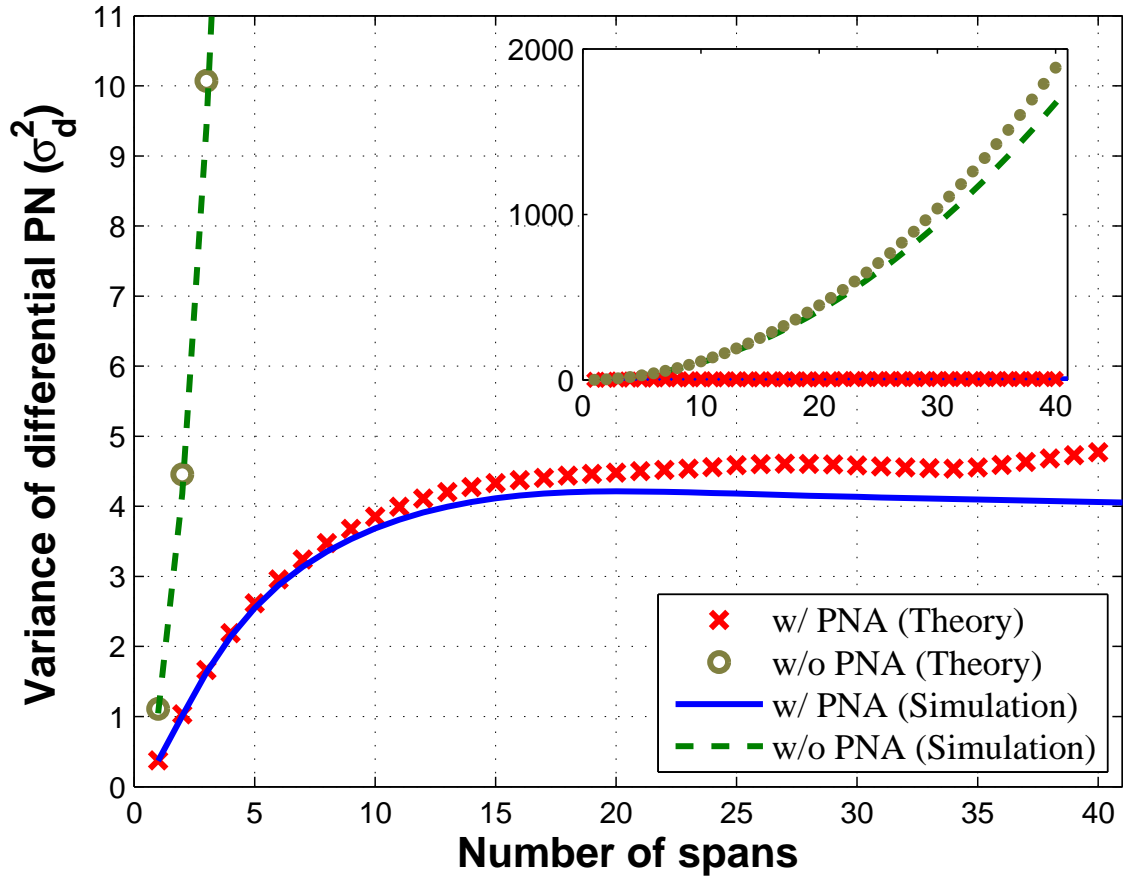
Figure 4.11: The variances of differential PN as functions of the number of spans

4.3.2.3 Simulation of RZ-DPSK transmission

In order to examine the effect of actual PNAs illustrated in Fig. 4.2 with both linear and nonlinear PNs, a single-channel 40 Gbps RZ-DPSK transmission system is then investigated using commercially available software, *VPI TransmissionMaker* v6.5. The transmission system in the simulation is shown in Fig. 4.13 which is identical to the setup displayed in Fig. 4.6. The laser linewidth of the transmitter is 10 MHz and the duty cycle of RZ-DPSK is 33%. The length, dispersion, dispersion slope, nonlinear coefficient and loss of the SSMF are 80 km, 17 ps/nm/km, 0.07 ps/nm^2/km, 1.3/W/km and 0.2 dB/km, respectively. For DCF, the corresponding parameters are 13.6 km, -100 ps/nm/km, -0.41 ps/nm^2/km, 5.4/W/km and 0.65 dB/km. The noise figure (NF) of the EDFAs is 5 dB;
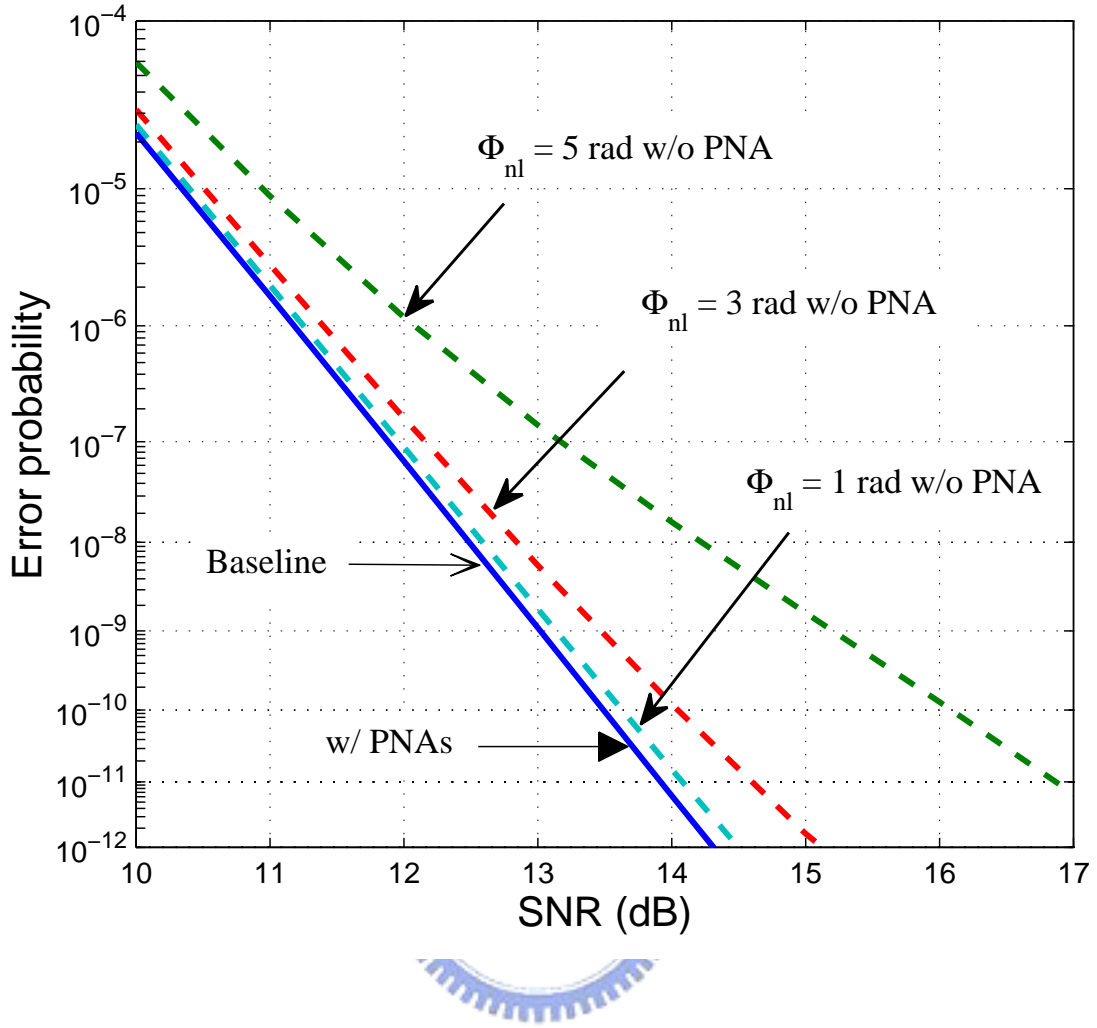
Figure 4.12: The curves of error probability as functions of the SNR and nonlinear impairment

the launch power into SSMFs and DCFs are 3 dBm and -3 dBm, respectively. The approach of the phase-preserving amplitude regenerator adopted in the simulation is based on the FWM effect in fibers because it has a simple structure. The characteristics of the FWM-based regenerator are described elsewhere [63], and in this regenerator, HNLF length, dispersion, dispersion slope, nonlinear coefficient, loss, $\Delta\lambda$ (wavelength difference between a pump beam and a DPSK signal beam), pump power, output peak power, and filter bandwidth are 1.5 km, 0.09 ps/nm/km, 0.03 ps/nm^2/km, 16.2/W/km, 0.5 dB/km, 3 nm, 30 mW, 8.4 mW, and 160 GHz, respectively. The characteristics of the PNA in the simulation are described in Fig. 4.4. The transmitted signal is a De Bruijn sequence
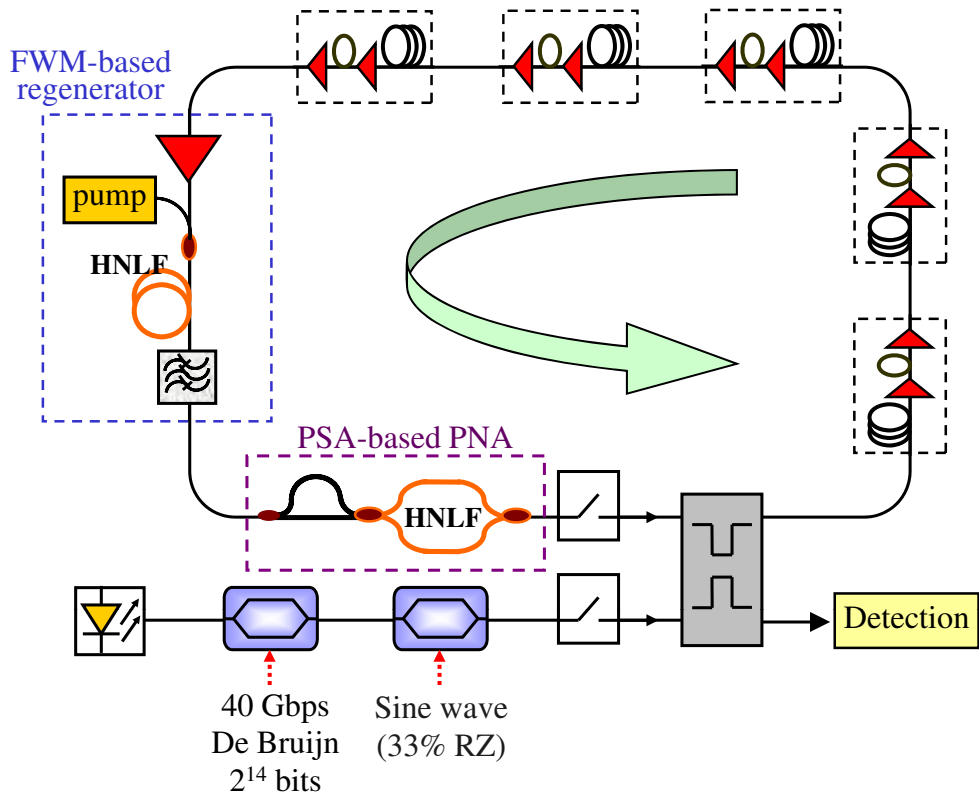
Figure 4.13: The simulation setup of 40 Gbps 33% RZ-DPSK

of 4096 bits. A FWM-based amplitude regenerator and a PSA-based PNA are inserted
every 400 km of transmission, i.e. $K = 5$.

Figure 4.14(a) displays the standard deviation (STD) of intensity noise (IN) normal-
ized to the average peak power every 80 km of transmission. Figure 4.14(b) shows the
STD of differential PN of DPSK signals at the corresponding distances. In the DPSK
transmission system without regenerators and PNAs, normalized IN and differential PN
increase absolutely with the transmission distance. With amplitude regenerators, IN can
be effectively managed, but PN is still continuously accumulated. The PN initially de-
clines at first and second regenerators due to the optical filter in the regenerators [55][56].
However, the differential PN with regenerators exceeds that without regenerators after
1600 km, because the regenerators add extra PN [63]. If PNAs are inserted after regen-
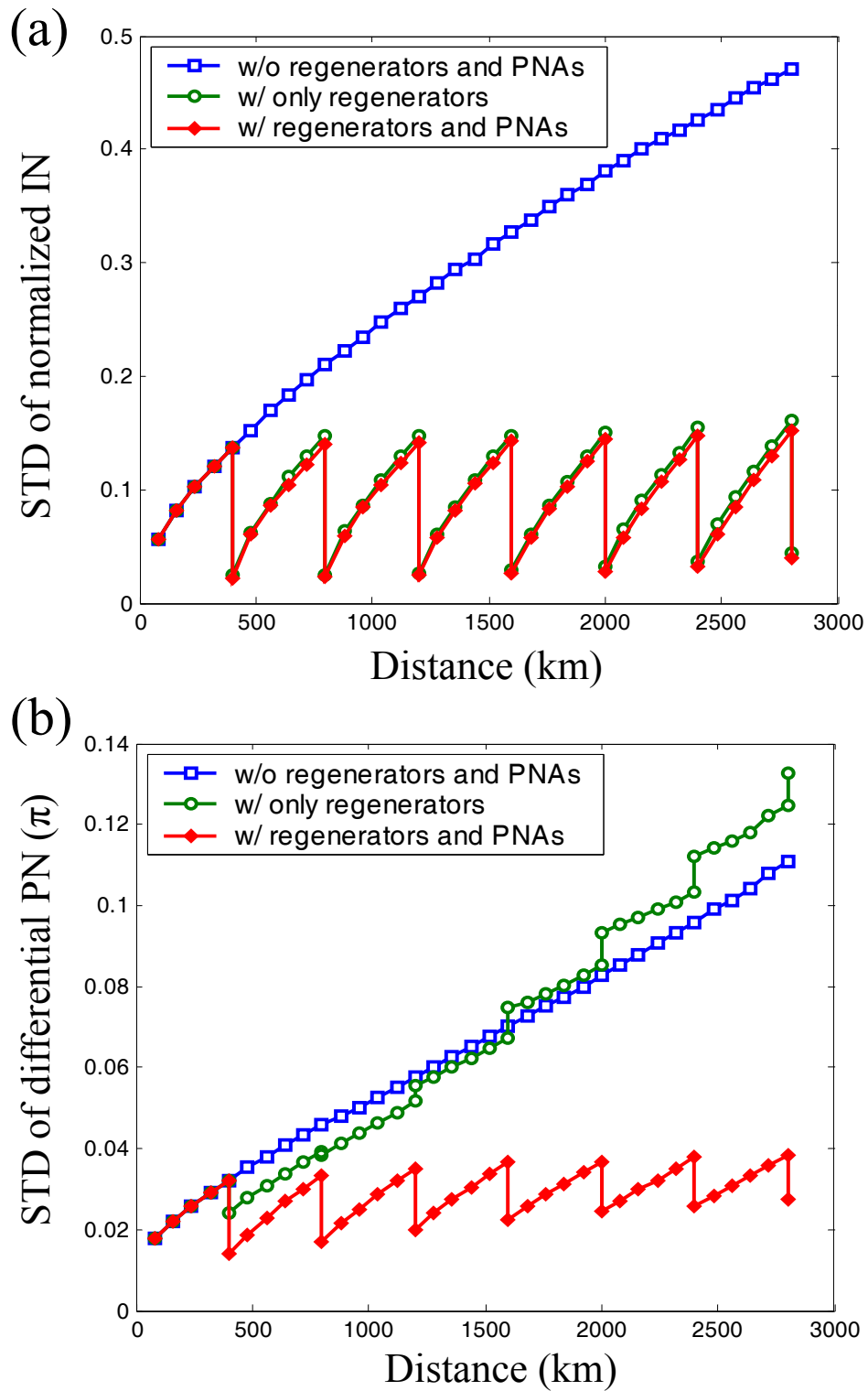
Figure 4.14: (a) Normalized IN and (b) differential PN versus transmission distance for 40 Gbps 33% RZ-DPSK

(a)

(b)

(c)

(d)

0   25 ps

0   25 ps
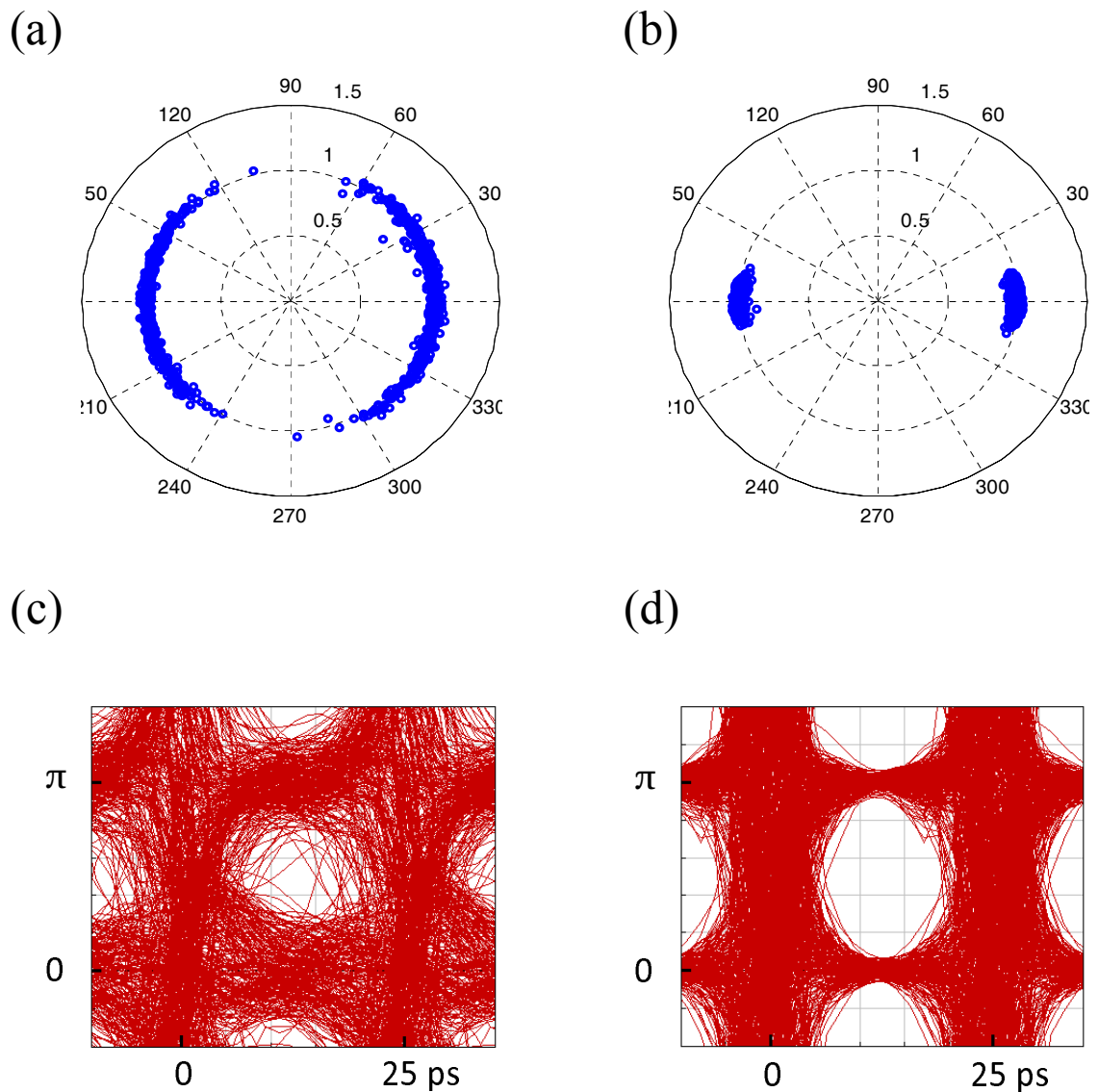
Figure 4.15: Differential phasor diagrams for 40 Gbps 33% RZ-DPSK after 2800 km transmission. For (a), FWM-based regenerators are inserted, and for (b), FWM-based regenerators and PSA-based PNA are both inserted every 400 km. (c) and (d) are the differential phase eye-diagrams corresponding to (a) and (b), respectively.

erators, then the differential PN behind the averagers is constrained and increases at a

extremely low rate. Figures 4.15(a)-(d) illustrate the differential phase constellations and

differential phase eye-diagrams of DPSK signals after 2800 km of transmission with and

without PNAs. In Figs. 4.15(a) and (c), the DPSK signals without PNAs suffer from

serious PN and the differential phase eye is almost closed. Consequently, although the

amplitude of DPSK signals is managed well, as shown in Fig. 4.15(a), the groups with zero and π phase shifts almost overlap each other. When PNAs are used, PN is managed efficiently even after transmission of 2800 km and the performance of signals is effectively maintained.

4.4 Analysis of error probability

It has been proposed that only phase-preserving amplitude regeneration can also realized PN averaging [35]-[37]. Nevertheless, while linear PN, ϑ_n, becomes $(\vartheta_n + \vartheta_{n-1})/2$ by PN averaging, only less than 30% of PN is removed. How the 30% reduction of linear PN influences DPSK signals will be discussed in this section. Moreover, various regeneration schemes are considered, and the pdf of the phase distribution and the error probability of a DPSK system with complex Gaussian noise are given analytically for the first time. Comparing the results with ideal PN regeneration demonstrates that PN-averaging can eliminate most of the PN-induced penalty. Since only Gaussian noise is considered, these results show the upper limits of various regeneration schemes.

Figure 4.16: Schematic of regeneration configuration

Figure 4.16 presents the configuration of the DPSK system with regeneration. When a polarizer is applied to filter out the noise which is orthogonal to DPSK signals, the

signals with complex Gaussian noise at point **1** can be represented as $u(t) = A(t) + n_1(t)$, where $A(t) = \pm A_0$ is the DPSK signal, and n_1 is complex Gaussian noise with the variance of $2\sigma_1^2$. To bett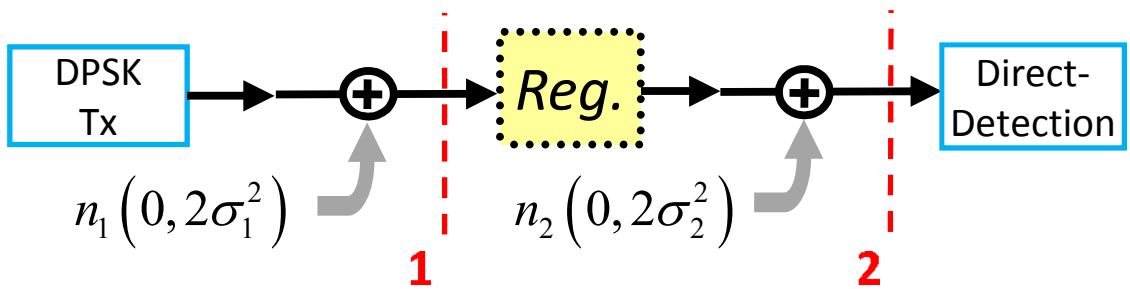er understand the noise suppression capability of a regenerator, the inherent noises of the regenerator can be included after the regenerator, and therefore, all regenerators discussed in this work are assumed to be noiseless and lossless (or gain $= 1$). With phase-preserving regeneration, the amplitude-regenerated signals become $\mathrm{AR}\{u(t)\} = \pm\sqrt{A_0^2 + 2\sigma_1^2} \times \exp(j\vartheta)$, where $\mathrm{AR}\{\cdot\}$ indicates the phase-preserving amplitude regeneration without changing average power and $\vartheta = \measuredangle(A_0 + n_1)$ is the PN. Identical to Eq. (3.76), the pdf of ϑ can be expressed as a Fourier series,

$$p_\Theta(\vartheta) = \frac{1}{2\pi} \sum_{m=-\infty}^{\infty} \frac{\sqrt{\pi\rho_1}}{2} e^{-\frac{\rho_1}{2}} \Pi_m(\rho_1) e^{-jm\vartheta} , \tag{4.24}$$

where $\rho_1 = A_0^2/(2\sigma_1^2)$ is the SNR at point **1**. When complex Gaussian noise with a variance of $2\sigma_2^2$ is added between points **1** and **2**, as shown in Fig. 4.16, the pdf of differential PN at point **1** and point **2** are,

$$p_{\Delta\Theta}(\Delta\vartheta) = \frac{\rho_1 e^{-\rho_1}}{8} \sum_{m=-\infty}^{\infty} \Pi_m^2(\rho_1) e^{-jm\Delta\vartheta} , \tag{4.25}$$

$$p_{\Delta\Theta,\mathrm{pp}}(\Delta\vartheta) = \frac{\pi\rho_1\rho_{\mathrm{pp}} e^{-(\rho_1+\rho_{\mathrm{pp}})}}{32} \sum_{m=-\infty}^{\infty} \Pi_m^2(\rho_1)\Pi_m^2(\rho_{\mathrm{pp}}) e^{-jm\Delta\vartheta} , \tag{4.26}$$

where $\rho_{\mathrm{pp}} = (A_0^2 + 2\sigma_1^2)/(2\sigma_2^2) = \rho_2(1 + \rho_1^{-1})$ and $\rho_2 = A_0^2/(2\sigma_2^2)$. Eqs. (4.25) and (4.26) are derived based on the fact that the characteristic function of the sum of independent random variables is the product of individual characteristic functions. Then, the error probability of signals with phase-preserving regeneration is,

$$p_{e,\mathrm{pp}} = 1 - \int_{-\frac{\pi}{2}}^{\frac{\pi}{2}} p_{\Delta\Theta,\mathrm{pp}}(\Delta\vartheta)(\Delta\vartheta) \, \mathrm{d}\Delta\vartheta \tag{4.27}$$

$$= \frac{1}{2} - \frac{\pi\rho_1\rho_{\mathrm{pp}} e^{-(\rho_1+\rho_{\mathrm{pp}})}}{8} \sum_{m=0}^{\infty} \frac{(-1)^m}{2m+1} \Pi_{2m+1}^2(\rho_1)\Pi_{2m+1}^2(\rho_{\mathrm{pp}}) .$$

For comparison, the error probability of direct-detection DPSK signals without regener-

ation, according to Eq. (3.53), is,

$$p_{e,0} = \frac{e^{-\rho_0}}{2}, \tag{4.28}$$

where $\rho_0^{-1} = \rho_1^{-1} + \rho_2^{-1}$ is the final SNR at the receiver. Furthermore, an ideal coherent regenerator, such as an ideal coherent PSA [18], is assumed to be able to completely eliminate both AN and PN. The error probability determined by a coherent beam at the regenerator is identical to the case of coherent detection, $\text{erfc}(\sqrt{\rho_1})/2$, where $\text{erfc}\{\cdot\}$ is the complementary error function [48]-[50]. Because the regenerator is lossless, the error probability at the direct-detection receiver is $\exp(-\rho_{\text{pp}})/2$. With negligible differences the cross term can be omitted, and the final error probability with coherent regeneration is,

$$p_{e,\text{co}} = \frac{1}{2}\left(\text{erfc}\left(\sqrt{\rho_1}\right) + e^{-\rho_{\text{pp}}}\right). \tag{4.29}$$
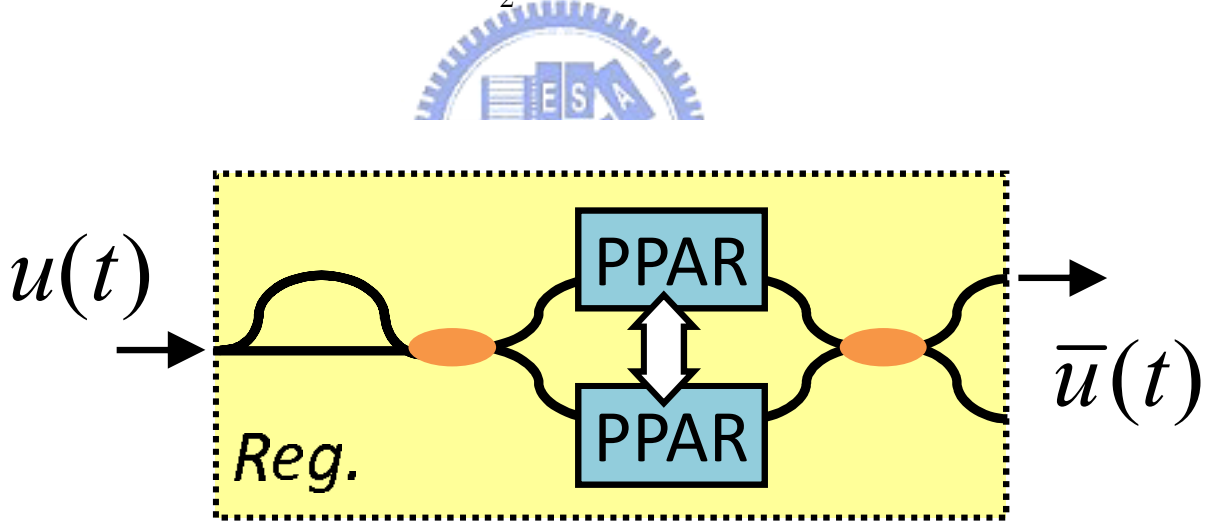
Figure 4.17: Setup of the PN-averaged regenerator. PPAR: phase-preserving amplitude regenerator.

Moreover, phase-preserving amplitude regenerators can simultaneously realize AN elimination and PN averaging [37]. As shown in Fig. 4.17, a DI converts the DPSK signals into two phase-modulated OOK signals: DB, $[A(t) + A(t-T) + n_1(t) + n_1(t-T)]/2$, and AMI, $[A(t) - A(t-T) + n_1(t) - n_1(t-T)]/2$. Ideally, the amplitude regenerators can

eliminate AN of both marks and spaces, i.e., the output power of both OOK signals is either 0 or $A_0^2 + \sigma_1^2$ and the signals become $\bar{u}(t) = \mathrm{AR}\{A(t) + [n_1(t) \pm n_1(t - T)]/2\}$, where 3-dB loss is neglected and $\pm$ depends on $A(t)$ and $A(t - T)$ being in-phase or out-of-phase. Since $\vartheta(t) \cong \Im\{n_1(t)\}/A(t)$, where $\Im\{\cdot\}$ is the imaginary part, the PN of $\bar{u}(t)$ can be approximated as $[\vartheta(t) + \vartheta(t - T)]/2$, which turns out to be the averaged PN. Although cascading another DI after the PNA regenerator can further increase the correlation between PNs of adjacent pulses, it also induces additional AN, and this is beyond the scope of this discussion. Owing to $\bar{u}(t)$ and $\bar{u}(t - T)$ influenced by identical noise $n_1(t - 2T)/2$ as well as independent noise $n_1(t)/2$ and $n_1(t - 2T)/2$, the pdfs of differential PN at points **1** and **2** are (Appendix B)

$$p_{\Delta\Theta}(\Delta\vartheta) = \frac{e^{-4\rho_1}}{8} \sum_{m=-\infty}^{\infty} H_m(1, 4\rho_1) e^{-jm\Delta\vartheta} , \qquad (4.30)$$

$$p_{\Delta\Theta,\mathrm{pna}}(\Delta\vartheta) = \frac{\pi\rho_{\mathrm{pna}} e^{-(4\rho_1 + \rho_{\mathrm{pna}})}}{32} \sum_{m=-\infty}^{\infty} H_m(1, 4\rho_1) \Pi_m^2(\rho_{\mathrm{pna}}) e^{-jm\Delta\vartheta} , \qquad (4.31)$$

where

$$H_m(\xi, \rho) = \int_0^\infty y e^{-(1+\xi)y} I_0\left(2\sqrt{\xi\rho y}\right) \Pi_m^2(y) \, \mathrm{d}y , \qquad (4.32)$$

and $\rho_{\mathrm{pna}} = (A_0^2 + \sigma_1^2)/(2\sigma_2^2) = \rho_2[1 + (2\rho_1)^{-1}]$. Moreover, since the ideal amplitude regeneration of OOK signals must make a binary decision on signals, the error probability determined at the PNA regenerator, $p_{e,1}$, depends on the criterion of the binary decision. While the amplitude regenerators in Fig. 4.17 are steplike and mutually independent, the error probability can be approximated as double that of the OOK signals: $p_{e,1} = \exp(-\rho_1/2)$ [48]. Otherwise, when the decision is made by comparing the power of two OOK signals [35][36], it is similar to direct-detection DPSK: $p_{e,1} = \exp(-\rho_1)/2$. Therefore, by integrating Eq. (4.31) the error probability at the receiver is,

$$p_{e,\mathrm{pna}} = \frac{e^{-\rho_1}}{2} + \frac{1}{2} - \frac{\pi\rho_{\mathrm{pna}} e^{-(4\rho_1\rho_{\mathrm{pna}})}}{8} \sum_{m=0}^{\infty} \frac{(-1)^m}{2m+1} H_{2m+1}(1, 4\rho_1) \Pi_{2m+1}^2(\rho_{\mathrm{pna}}) . \qquad (4.33)$$

The first term in Eq. (4.33) is $p_{e,1}$ with the best decision criterion. Even though the amplitude regenerators in Fig. 4.17 only remove the AN of spaces with marks left unchanged, the PN of adjacent bits have been simultaneously averaged. The regenerated signals become $\bar{u}'(t) = A(t) + [n_1(t) \pm n_1(t - T)]/2$ of which the phase is identical to that of $\bar{u}(t)$ but residual AN still exists. Hence, neighboring pulses at point **2** contain identical and mutually independent noises with variances of $\sigma_1^2/2$ and $\sigma_1^2 + 2\sigma_2^2$, respectively, and the pdf of differential PN and the error probability become,

$$p_{\Delta\Theta,\text{pna}'}(\Delta\vartheta) = \frac{(4\rho_1 + \rho_2)e^{-4\rho_1}}{8\rho_2} \sum_{m=-\infty}^{\infty} H_m\left(1 + \frac{4\rho_1}{\rho_2}, 4\rho_1\right) e^{-jm\Delta\vartheta}, \qquad (4.34)$$

$$p_{e,\text{pna}'} = \frac{e^{-\rho_1}}{2} + \frac{1}{2} \qquad (4.35)$$
$$- \frac{(4\rho_1 + \rho_2)e^{-4\rho_1}}{2\rho_2} \sum_{m=0}^{\infty} \frac{(-1)^m}{2m + 1} H_{2m+1}\left(1 + \frac{4\rho_1}{\rho_2}, 4\rho_1\right).$$

Figure 4.18(a) plots the pdfs of PN, differential PN, and averaged differential PN without n_2, which are described by Eqs. (4.24), (4.25) and (4.30) with $\rho_1 = 14$ dB. The tail of differential PN distribution, which is the main contributor to the error probability, is effectively suppressed by PNA regeneration. Moreover, the variance of these phase distribution can be simply calculated through $\int_{-\pi}^{\pi} \theta^2 \, p_X(\theta) \, d\theta$, where $p_X(\theta)$ is the corresponding pdf, and they are,

$$\text{PN}: \quad \frac{\pi^2}{3} + 2\sqrt{\pi\rho_1}e^{-\frac{\rho_1}{2}} \sum_{m=1}^{\infty} \frac{(-1)^m}{m^2} \Pi_m(\rho_1)$$

$$\text{Differential PN}: \quad \frac{\pi^2}{3} + \pi\rho_1 e^{-\rho_1} \sum_{m=1}^{\infty} \frac{(-1)^m}{m^2} \Pi_m^2(\rho_1)$$

$$\text{Averaged differential PN}: \quad \frac{\pi^2}{3} + \pi e^{-4\rho_1} \sum_{m=1}^{\infty} \frac{(-1)^m}{m^2} H_m(1, 4\rho_1)$$

The results plotted in Fig. 4.18(b) indicate that the configuration of Fig. 4.17 can realize PN averaging, since the variance of averaged differential PN is about the quarter of that of original differential PN.

After loading n_2, the solid curves in Fig. 4.19 show the analytical results of $p_{e,0}$, $p_{e,\mathrm{co}}$, $p_{e,\mathrm{pp}}$, $p_{e,\mathrm{pna}}$ and $p_{e,\mathrm{pna'}}$, corresponding to Eqs. (4.28), (4.29), (4.27), (4.33) and (4.35), respectively. The error floors for coherent regeneration and PNA regeneration are determined by n_1, and it indicates that any regenerator can only improve signal performance but cannot correct existing errors. In addition, the error probabilities indicated by markers in Fig. 4.19 are assessed by the brute-force Monte Carlo method, performed with 10^9 bits, and the results closely agree with each other.

The SNR required to achieve the BER of 10^{-9}, shown in Fig. 4.20, indicates that PNA regeneration can remove most penalty induced by PN, because the difference between its SNR and that of perfect coherent regeneration is less than $\sim$0.3 dB. However, if steplike independent amplitude regenerators are adopted in PNA regeneration (dashed curve in Fig. 4.20) then regeneration fails when ρ_1 is less than 16.2 dB. Accordingly, the amplitude regenerators shown in Fig. 4.17 dominate the performance of PNA regeneration if the input SNR is low. Furthermore, Fig. 4.20 demonstrates that the improvement over phase-preserving regeneration vanishes when SNR is lower than 15 dB, because the PN induced by n_1 dominates the whole PN. Similarly, since averaging PN suppresses most PN-induced penalties, the signals with PNA residual AN regeneration can outperform those with phase-preserving regeneration, as ρ_1 is low.
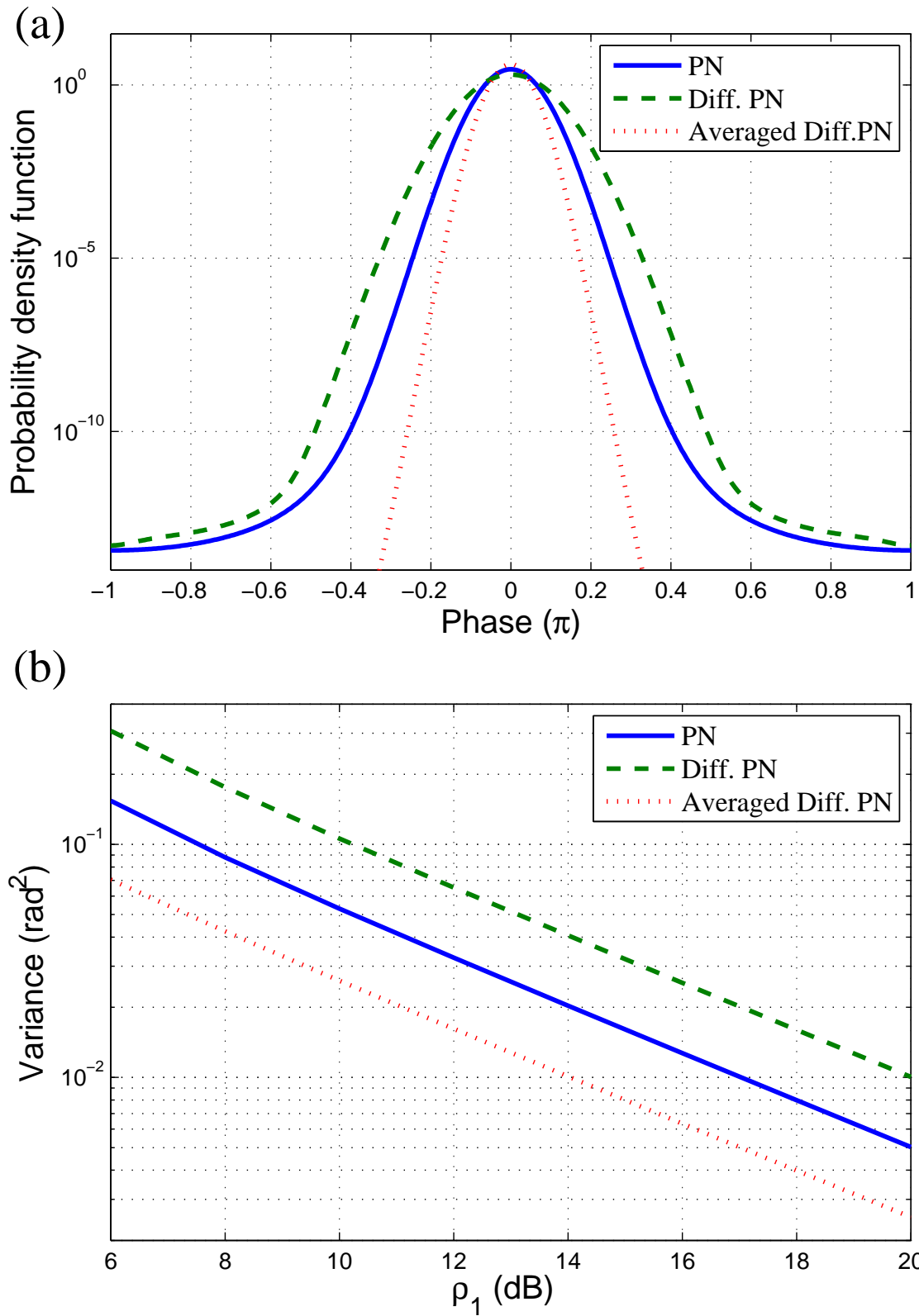
Figure 4.18: (a) pdf of phase distributions with $\rho_1 = 14$ dB, and (b) variance of phase distributions as a function of ρ_1
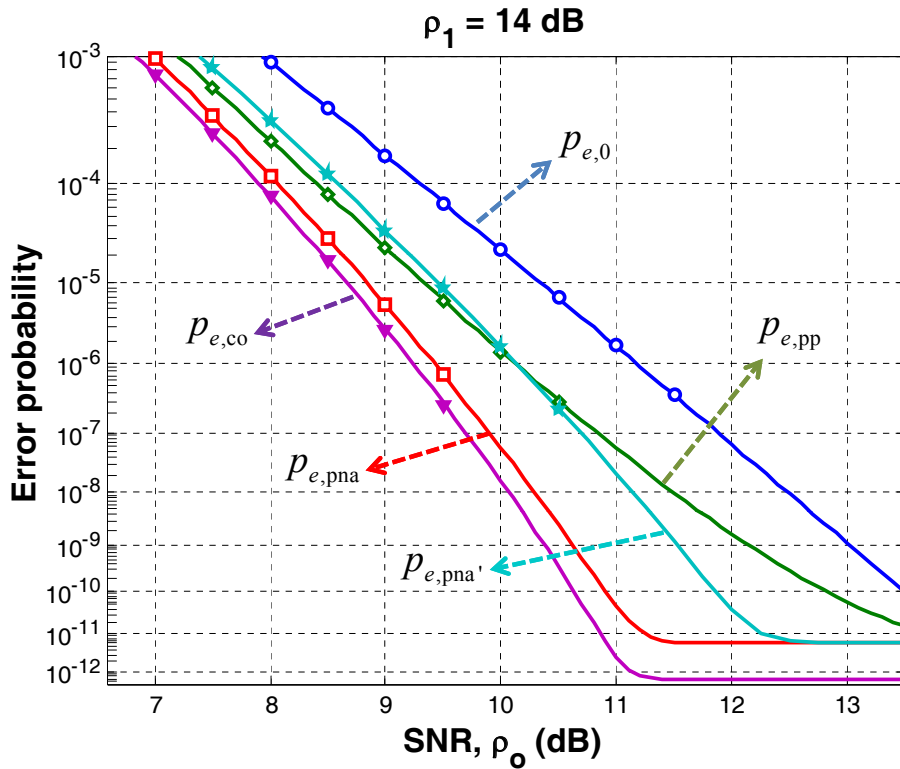
Figure 4.19: Error probabilities of DPSK signals with various regeneration schemes (curves: analytical results and markers: Monte Carlo method)
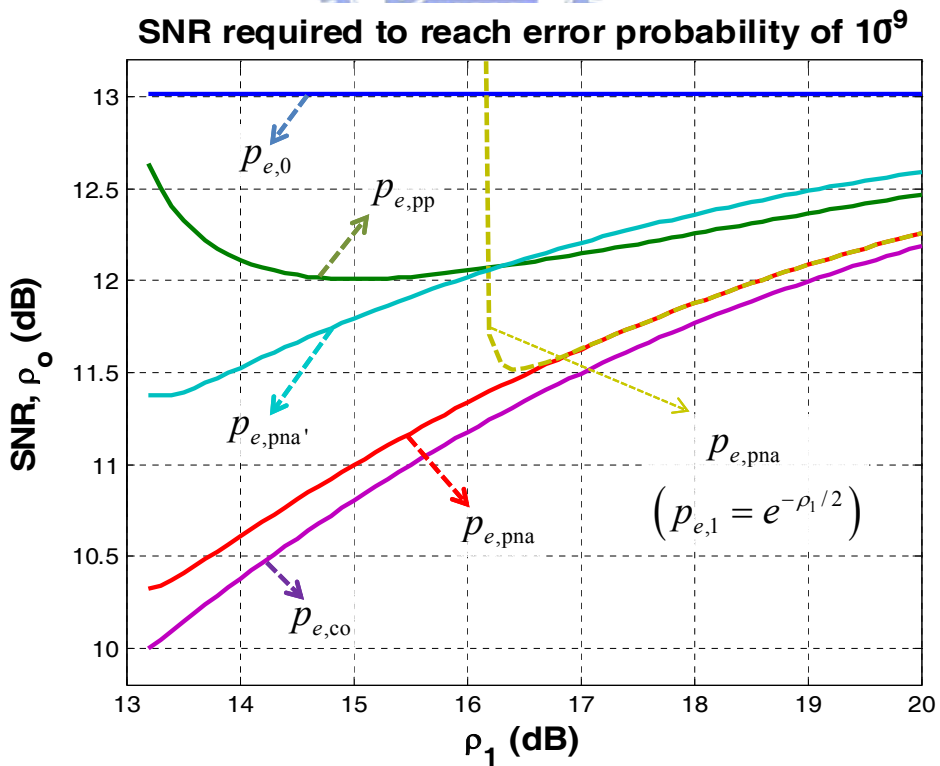
Figure 4.20: SNR at the error probability of 10^{-9}

Chapter 5

Conclusions

In this dissertation research, we have studied a number of key all-optical signal processing issues that are vital to the high bit-rate, high performance optical communications applications.

5.1 Wavelength conversion

For wavelength conversion, our work has proposed a novel wavelength conversion scheme called DXPoM by simply adding an extra birefringence delay line in the standard XPoM. The delay line adjusts the time differential between two orthogonal modes to overcome the limitation of the carriers recovery time in an SOA. Both the large-signal simulation based on TMM and experimental results indicate that the proposed method significantly improves the wavelength conversion performance. The new technique exhibits an error free wavelength conversion operation with more than 7-dB power penalty improvement over XPoM. The DXPoM scheme shows a pulse reshaping function, an improvement of more than 300% in rise time, reduced timing jitter and a higher ER. The small-signal model of XPoM is presented for the first time. Nevertheless, the modulation bandwidth of XPoM is identical to XGM, and is limited by the carrier's recovery time. By considering the time delay between two orthogonal modes, the corresponding transfer function of DXPoM shows apparent bandwidth improvement. Through the analytical expression of modulation bandwidth of DXPoM, we can readily observe the relations between the bandwidth improvement of DXPoM and several parameters, such as lifetimes,

confinement factors, gain coefficients, and operating points.

5.2 Format conversion

The work of format conversion was done at UMBC during the period of my exchange program. We used the XPM effect in a nonlinear PCF to carry out the conversion of RZ-OOK-to-RZ-DPSK at 40 Gb/s for the first time. Because the PCF has high linear birefringence, and its birefringent axes remain for entire length, launching the probe at 45° relative to the birefringence axes of the PCF and having the PPD greater than ~ 6 nm can realize polarization-insensitive XPM-based conversion. While the OOK pump and probe are launched at the same birefringent axis, the converted DPSK probe performed better than the baseline of the OOK signal. However, after the pump is polarization scrambled, an error floor was observed. Once the probe was adjusted to be at 45° with respect to the PCF birefringent axes, error-free BER was achieved, but it shows $\sim$ 7-dB penalty compared with the baseline of the DPSK signal. Moreover, this part theoretically analyzes XPM effect in a highly birefringent HNLF with an arbitrary polarized pump beam by the nonlinear Schrödinger equation. When the probe beam is launched at an axis and $2\gamma P_1 L = \pi$, the optimized threshold and penalties of a DPSK probe are $0 \sim 76.2\%$ and $0 \sim 14.1$ dB. By contrast, if the probe beam with $\Delta BL = 2\pi$ is launched at 45° and $2\gamma P_1 L = \pi$, the variations can be reduced to $31.5\% \sim 42.8\%$ and 3.7 dB ~ 5.6 dB, and they become $23.2\% \sim 41.8\%$ and 2.5 dB ~ 5.4 dB by setting $2\gamma P_1 L = 1.1\pi$. Consequently, launching the probe at 45° can decrease the variations of both threshold and sensitivity caused by arbitrary polarized OOK signals, but the penalty is never zero. Furthermore, since optical amplifiers are required to compensate transmission loss or increase nonlinear effect in format conversion, the SNR of OOK signals must be finite and the OOK signals

must have AN. Through theoretical investigation, the SNR of > 29 dB is required to suppress the correspond penalty of the DPSK probe less than 1 dB.

5.3   Phase regeneration

As to the regeneration of the DPSK format, we propose a novel all-optical PSA-based PNA that does not require a complicated optical coherent pump beam with optical phase-locking. The PNA can increase the correlation between PN of neighboring bits. Theoretical analyses confirm that inserting PNAs after in-line amplitude regenerators can effectively reduce the differential PN. Since the PN is suppressed by increasing its correlation, the multiple PN averaging effect dependents on the characteristics of PN. According the characteristics, PN can be divided into two categories, random and deterministic PNs, and the later one is caused by signals and fiber nonlinearity. In a high-speed amplitude managed DPSK transmission system, the main PNs of two categories are linear PN and IFWM-induced PN, respectively. For linear PN, the total differential PN is limited to less than that before the first averager and is independent of the number of DPSK spans. For IFWM-induced PN, a comprehensive theoretical model that incorporates the nonlinear effect of DCF is established to investigate the property of IFMW-induced PN, and the results indicate that the PN induced in DCF cannot be neglected. The multiple PN averaging effect on IFWM-induced PN is examined by both theoretical analysis and numerical simulation, and a strong agreement between them confirms the convergence of IFWM-induced PN with periodic PN averaging. Furthermore, the semianalytical method is used to compute BER and shows that PN averaging can obviate the nonlinear penalty. Moreover, the numerical simulation of a practical 40 Gbps DPSK system confirms that inserting PNAs after in-line amplitude regenerators can effectively reduce the differential

PN even after the transmission of 2800 km. Compared with the system without regeneration, periodic PNAs can reduce the STD of DPN by $\sim 75\%$. Moreover, by considering only linear PN, we analytically derives the BERs of amplitude-regenerated DPSK signals with no additional phase processing, PN averaging, and ideal phase regeneration. The SNR difference at the BER of 10^{-9} between PNA regeneration and ideal phase regeneration is less than 0.3 dB, indicating that incoherent PNA regeneration eliminates most of the PN-induced penalty, even though PN is statistically reduced by less than 30%.

5.4   Future works

In order to increase the spectral efficiency to more than 1 b/s/Hz without polarization-division multiplexing, multilevel signals, such as DQPSK and quadrature-amplitude modulation (QAM), must be adopted to transmit more than one bit per symbol. While the DQPSK format are transmitted with polarization-division multiplexing, the spectral efficiency is more than 2 b/s/Hz [64]. Recently, the interest in the DQPSK format has increased because of its high tolerance to fiber nonlinearities, similar to the DPSK format, and several all-optical signal processing schemes related to the DQPSK format have been proposed, such as wavelength conversion [65] and format conversion [14][66]. However, compared with DPSK signals, DQPSK signals have lower tolerance to PN [67]. Although phase-preserving amplitude regeneration may be applied to decelerate the accumulation of the nonlinear PN in DQPSK systems, the residual PN can be much more harmful to signal performance. Consequently, the all-optical phase regeneration of DQPSK would be an important research topic, and it has not been investigated. Actually, cascading the PN-averaged regenerators shown in Fig. 4.17 is able to average the PN of DQPSK signals. In principle , as shown in Fig. 5.1, the first regenerator can average the PN of neighboring

bits whose phase difference is $\pi/2$, but leave those with differential phase of $\pi/4$ or $3\pi/4$ alone. Then, by adding phase shift of $\pi/4$ in the second DI, the second regenerator can averaged the PN of unchanged bits. However, the key issue would be choosing proper amplitude-preserving amplitude regenerators, which can only generate negligible PN.
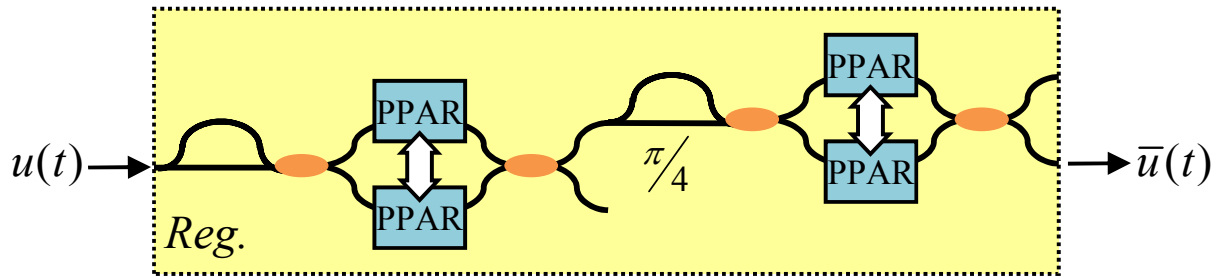

Figure 5.1: Cascading PN-averaged regenerators

Appendix A

Error probabilities of the DPSK format with nonzero threshold

According to Eqs. (3.32) and (3.39), the inner integration of Eq. (3.36) is,

$$\int_0^{x_2+h} p_{X_1}(x_1)\,\mathrm{d}x_1 = 1 - Q_2\left(\sqrt{\lambda_1}, \sqrt{x_2+h}\right),\tag{A.1}$$

and therefore, Eq. (3.36) becomes,

$$p_e^{\mathrm{in}} = 1 - \frac{1}{4}\int_0^\infty x e^{-\frac{x}{2}} Q_2\left(\sqrt{\lambda_1}, \sqrt{x+h}\right).\tag{A.2}$$

It is easier to integrate Eq. (A.2) by representing it as an inverse Laplace transform. Before doing that, some useful relations are listed below:

$$I_m\left(2\sqrt{ab}\right) = \frac{1}{2\pi j}\left(\frac{b}{a}\right)^{\frac{m}{2}}\int_{\epsilon-j\infty}^{\epsilon+j\infty}\frac{1}{p^{m+1}}e^{ap+\frac{b}{p}}\,\mathrm{d}p,\tag{A.3}$$

$$I_m\left(2\sqrt{ab}\right) = \frac{1}{2\pi j}\left(\frac{a}{b}\right)^{\frac{m}{2}}\int_{\epsilon-j\infty}^{\epsilon+j\infty}p^{m-1}e^{ap+\frac{b}{p}}\,\mathrm{d}p,\tag{A.4}$$

$$Q_1\left(\sqrt{2a}, \sqrt{2b}\right) = \int_b^\infty e^{-(a+x)}I_0\left(2\sqrt{ax}\right)\,\mathrm{d}x\tag{A.5}$$

$$= \frac{1}{2\pi j}e^{-(a+b)}\int_{\epsilon-j\infty}^{\epsilon+j\infty}\frac{1}{p-1}e^{ap+\frac{b}{p}}\,\mathrm{d}p,$$

$$Q_2\left(\sqrt{2a}, \sqrt{2b}\right) = \int_b^\infty e^{-(a+x)}\sqrt{\frac{x}{a}}I_1\left(2\sqrt{ax}\right)\,\mathrm{d}x\tag{A.6}$$

$$= \frac{1}{2\pi j}e^{-(a+b)}\int_{\epsilon-j\infty}^{\epsilon+j\infty}\frac{p}{p-1}e^{ap+\frac{b}{p}}\,\mathrm{d}p.$$

Inserting Eq. (A.6) into Eq. (A.2), $1 - p_e^{\mathrm{in}}$ can be represented as,

$$1 - p_e^{\mathrm{in}} = \frac{1}{8\pi j}e^{-\frac{\lambda_1+h}{2}}\int_{\epsilon-j\infty}^{\epsilon+j\infty}\frac{p}{p-1}e^{\frac{\lambda_1}{2}p+\frac{h}{2p}}\left[\int_0^\infty x e^{-x+\frac{x}{2p}}\,\mathrm{d}x\right]\mathrm{d}p$$

$$= \frac{1}{2\pi j}e^{-\frac{\lambda_1+h}{2}}\int_{\epsilon-j\infty}^{\epsilon+j\infty}\frac{p^3}{(p-1)(2p-1)^2}e^{\frac{\lambda_1}{2}p+\frac{h}{2p}}\,\mathrm{d}p,\tag{A.7}$$

110

where the orders of integrations are interchanged. Furthermore, $p^3/(p-1)/(2p-1)^2$ can be taken apart as,

$$\frac{p^3}{(p-1)(2p-1)^2} = \frac{1}{4} + \frac{1}{p-1} - \frac{1}{2p-1} - \frac{1}{4(2p-1)^2} . \tag{A.8}$$

Using Eqs. (A.4) and (A.5), the first and second parts of Eq. (A.8) in Eq. (A.7) follow,

$$\frac{e^{-\frac{\lambda_1+h}{2}}}{2\pi j} \int_{\epsilon-j\infty}^{\epsilon+j\infty} \left(\frac{1}{4} + \frac{1}{p-1}\right) e^{\frac{\lambda_1}{2}p+\frac{h}{2p}} \, dp = \frac{e^{-\frac{\lambda_1+h}{2}}}{4} \sqrt{\frac{h}{\lambda_1}} I_1\left(\sqrt{\lambda_1 h}\right) + Q_1\left(\sqrt{\lambda_1}, \sqrt{h}\right) . \tag{A.9}$$

Making $2p = s$ and using Eqs. (A.5) and (A.3), the third and fourth parts follow,

$$\frac{e^{-\frac{\lambda_1+h}{2}}}{4\pi j} \int_{\epsilon'-j\infty}^{\epsilon'+j\infty} \frac{1}{s-1} e^{\frac{\lambda_1}{4}s+\frac{h}{s}} \, ds = \frac{e^{-\frac{\lambda_1}{4}+\frac{h}{2}}}{4} Q_1\left(\sqrt{\frac{\lambda_1}{2}}, \sqrt{2h}\right) , \tag{A.10}$$

$$\frac{e^{-\frac{\lambda_1+h}{2}}}{16\pi j} \int_{\epsilon'-j\infty}^{\epsilon'+j\infty} \frac{1}{(s-1)^2} e^{\frac{\lambda_1}{4}s+\frac{h}{s}} \, ds = \frac{e^{-\frac{\lambda_1+h}{2}}}{16\pi j} \int_{\epsilon'-j\infty}^{\epsilon'+j\infty} \left(\sum_{m=1}^{\infty} \frac{m}{s^{m+1}}\right) e^{\frac{\lambda_1}{4}s+\frac{h}{s}} \, ds$$

$$= \frac{e^{-\frac{\lambda_1+h}{2}}}{8} \sum_{m=1}^{\infty} m \left(\frac{\lambda_1}{4h}\right)^{\frac{m}{2}} I_m\left(\sqrt{\lambda_1 h}\right) , \tag{A.11}$$

where $1/(s-1)^2$ is expanded as a power series of $1/s$. As a result, the error probability is,

$$p_e^{\text{in}} = 1 - Q_1\left(\sqrt{\lambda_1}, \sqrt{h}\right) + \frac{1}{2} e^{-\frac{\lambda_1}{4}+\frac{h}{2}} Q_1\left(\sqrt{\frac{\lambda_1}{2}}, \sqrt{2h}\right)$$

$$- \frac{1}{4} e^{-\frac{\lambda_1}{2}-\frac{h}{2}} \sqrt{\frac{h}{\lambda_1}} I_1\left(\sqrt{\lambda_1 h}\right) + \frac{1}{8} e^{-\frac{\lambda_1}{2}-\frac{h}{2}} \sum_{m=1}^{\infty} m \left(\frac{\lambda_1}{4h}\right)^{\frac{m}{2}} I_m\left(\sqrt{\lambda_1 h}\right) . \tag{A.12}$$

On the other hand, the inner integration of Eq. (3.37) is,

$$\int_{x_4+h}^{\infty} p_{x_3}(x_3) \, dx_3 = Q_2\left(\sqrt{\lambda_3}, \sqrt{x_4+h}\right) . \tag{A.13}$$

Accordingly, the error probability follows,

$$p_e^{\text{out}} = \frac{1}{2} \int_0^{\infty} \sqrt{\frac{x}{\lambda_4}} e^{-\frac{\lambda_4+x}{2}} I_1\left(\sqrt{\lambda_4 x}\right) Q_2\left(\sqrt{\lambda_3}, \sqrt{x+h}\right) , \tag{A.14}$$

which is equal to Eq. (3.41). Similar to Eqs. (A.7) and (A.8), p_e^{out} can be rewritten as,

$$p_e^{\text{out}} = \frac{1}{2\pi j} e^{-\frac{\lambda_3+\lambda_4+2h}{4}} \int_{\epsilon'-j\infty}^{\epsilon'+j\infty} \left(\frac{1}{8} - \frac{1}{2s} - \frac{1}{8s^2} + \frac{1}{s-1} \right) e^{\frac{\lambda_3}{4}s + \frac{\lambda_4}{4s} + \frac{h}{s+1}} \, ds \,. \qquad \text{(A.15)}$$

Using the power series expansion for the terms relative to $\exp(h/(s+1))$,

$$\frac{e^{\frac{h}{s+1}}}{s^m} = \sum_{n=0}^{\infty} \mathbf{a}_n \frac{1}{s^{m+n}} \,,$$

$$\frac{e^{\frac{h}{s+1}}}{s-1} = \sum_{n=1}^{\infty} \mathbf{b}_n \frac{1}{s^n} \,,$$

where

$$\mathbf{a}_0 = 1 \,,$$

$$\mathbf{a}_n = \sum_{l=1}^{n} \frac{(-1)^{n-l}}{l!} \binom{n-1}{n-l} h^l \,, \qquad n \geq 1$$

$$\mathbf{b}_n = 1 + \frac{(-1)^n + 1}{2} h \,, \qquad 0 < n \leq 2$$

$$\mathbf{b}_n = 1 + \frac{(-1)^n + 1}{2} h + \sum_{l=2}^{n-1} \left[\sum_{m=l}^{n-1} \frac{(-1)^{m-l}}{l!} \binom{m-1}{l-1} \right] h^l \,, \qquad n \geq 3$$

and using Eqs. (A.3) and (A.4), the error probability becomes,

$$p_e^{\text{out}} = e^{-\frac{\lambda_3+\lambda_4+2h}{4}} \left[\frac{1}{8} \sqrt{\frac{\lambda_4}{\lambda_3}} I_1\left(\frac{\sqrt{\lambda_3 \lambda_4}}{2} \right) + \frac{1}{2} I_0\left(\frac{\sqrt{\lambda_3 \lambda_4}}{2} \right) \right.$$

$$\left. + \sum_{n=2}^{\infty} \left(\mathbf{b}_n + \frac{\mathbf{a}_n - 4\mathbf{a}_{n-1} - \mathbf{a}_{n-2}}{8} \right) \left(\frac{\lambda_3}{\lambda_4} \right)^{\frac{n-1}{2}} I_{n-1}\left(\frac{\sqrt{\lambda_3 \lambda_4}}{2} \right) \right] \,. \qquad \text{(A.16)}$$

Appendix B

Differential correlative phase noise

Assume $v = (A_0 + n_x) + n_y$ and $\tilde{v} = (A_0 + n_x) + \tilde{n}_y$, where n_x, n_y and $\tilde{n}_y$ are iid complex

Gaussian noises whose variances are $2\sigma_x^2$, $2\sigma_y^2$ and $2\sigma_y^2$. By defining $A_0 + n_x = r_0 \exp(j\phi)$,

$v = r \exp(j\varphi)$ and $\tilde{v} = \tilde{r} \exp(j\tilde{\varphi})$, the pdf of $\psi = \varphi - \phi$ (or $\tilde{\psi} = \tilde{\varphi} - \phi$) with given r_0 and

ϕ is,

$$p_\Psi(\psi|r_0, \phi) = \frac{e^{-\frac{\rho_y}{2}}}{4} \sqrt{\frac{\rho_y}{\pi}} \sum_{m=-\infty}^{\infty} \Pi_m(\rho_y) e^{-jm\psi} , \tag{B.1}$$

where $\rho_y = r_0^2/(2\sigma_y^2)$. Since $\Delta\varphi = \varphi - \tilde{\varphi}$ equals $\psi - \tilde{\psi}$, the pdf of $\Delta\varphi$ is,

$$p_{\Delta\Psi}(\Delta\psi|r_0, \phi) = \frac{\rho_y e^{-\rho_y}}{8} \sum_{m=-\infty}^{\infty} \Pi_m^2(\rho_y) e^{-jm\psi} , \tag{B.2}$$

Then, the pdf of $\Delta\psi$ without r_0 and ϕ is,

$$\begin{aligned} p_{\Delta\Psi}(\Delta\psi) &= \int_0^\infty \int_{-\pi}^\pi p_{\Delta\Psi}(\Delta\psi|r_0, \phi) \cdot p_{R_0, \Phi}(r_0, \phi) \, d\phi \, dr_0 \\ &= \int_0^\infty p_{\Delta\Psi}(\Delta\psi|r_0, \phi) \left[\int_{-\pi}^\pi p_{R_0, \Phi}(r_0, \phi) \, d\phi \right] dr_0 , \end{aligned} \tag{B.3}$$

because $p_{\Delta\Psi}(\Delta\psi|r_0, \phi)$ is independent of ϕ. Actually, the brackets in Eq. (B.3) is the

well-know Rice-distribution,

$$\int_{-\pi}^\pi p_{R_0, \Phi}(r_0, \phi) \, d\phi = \frac{r_0}{\sigma_x^2} \exp\left(-\frac{r_0^2 + A_0^2}{2\sigma_x^2}\right) I_0\left(\frac{r_0 A_0}{\sigma_x^2}\right) . \tag{B.4}$$

By inserting Eqs. (B.2) and (B.4), Eq. (B.3) can be represented as,

$$p_{\Delta\Psi}(\Delta\psi) = \frac{\xi e^{-\rho_x}}{8} \sum_{m=-\infty}^{\infty} H_m(\xi, \rho_x) \, e^{-jm\Delta\psi} , \tag{B.5}$$

where $\xi = \sigma_y^2/\sigma_x^2$, $\rho_x = A_0^2/(2\sigma_x^2)$ and the definition of $H_m(\xi, \rho_x)$ is Eq. (4.32).

Publication List

1. W. Astar, C.-C. Wei, Y.-J. Chen, J. Chen, and G. M. Carter, "Polarization-insensitive, 40 Gb/s wavelength and RZ-OOK-to-RZ-BPSK modulation format conversion by XPM in a highly nonlinear PCF," *Opt. Express*, vol. 16, pp. 12039-12049, Aug. 2008.

2. C. C. Wei, J. Chen and Y. J. Chen, "Evaluating the performance improvement of differential phase-shift keying signals by amplitude regeneration and phase-noise suppression," *Opt. Lett.*, vol. 33, pp. 1090-1092, May 2008.

3. C. C. Wei and J. Chen, "Convergence of phase fluctuation induced by intrachannel four-wave mixing in differential phase-shift keying transmission systems via phase fluctuation averaging," *Opt. Lett.*, vol. 32, pp. 1217-1219, May 2007.

4. Y. C. Lu, C. C. Wei, J. Chen, K. M. Feng, P. C. Yeh, T. Y. Huang, C. C. Chang, C. Tsao, and S. Chi, "Effects of filter andwidth and driving voltage on optical duobinary transmission systems," *Optical Fiber Technology*, vol. 13, pp. 231-235, Mar. 2007.

5. M.-F. Huang, J. Chen, K.-M. Feng, T.-Y. Lin, C.-Y. Lai, C.-C. Wei, S. Chi, Z. Zhu, Y. J. Chen, Y.-C. Huang, and S.-J. Chang, "Add/drop applications in fiber ring networks based on a reconfigurable optical add/drop multiplexer in a re-circulating loop," *Opt. Comm.*, vol. 267, pp. 113-117, Nov. 2006.

6. C. C. Wei and J. Chen, "Convergence of phase noise in DPSK transmission systems by novel phase noise averagers," *Optics Express*, vol. 14, pp. 9584-9593, Oct. 2006.

7. M.-F. Huang, K.-M. Feng, J. Chen, T.-Y. Lin, C.-C. Wei, and S. Chi, "Wavelength-interleaving bidirectional transmission system using unidirectional amplification in a 5100 km recirculating loop," *IEEE Photon. Technol. Lett.*, vol. 18, pp. 1326-1328, June 2006.

8. M.-F. Huang, J. Chen, K.-M. Feng, C.-C. Wei, C.-Y. Lai, T.-Y. Lin, and S. Chi, "210-km bidirectional transmission system with a novel four-port interleaver to facilitate unidirectional amplification," *IEEE Photon. Technol. Lett.*, vol. 18, pp. 172-174, Jan. 2006.

9. Y.-C. Lu, J. Chen, K.-M. Feng, P.-Chi Y., T.-Y. Huang, W.-R. Peng, M.-F. Huang, and C.-C. Wei, "Improved SPM tolerance and cost-effective phase-modulation duobinary transmission over 230-km standard single-mode fiber using a single Mach-Zehnder modulator," *IEEE Photon. Technol. Lett.*, vol. 17, no. 12, pp. 2754-2756, Dec. 2005.

10. C. C. Wei, and J. Chen, "Study of differential cross-polarization modulation in a semiconductor optical amplifier," *Opt. Express*, vol. 13, pp. 8442-8451, Oct. 2005.

11. C. C. Wei, M. F. Huang, and J. Chen, "Enhancing the frequency response of cross-polarization wavelength conversion," *IEEE Photon. Technol. Lett.*, vol. 17, pp. 1683-1685, Aug. 2005.

12. K.-M. Feng, M.-F. Huang, C.-C. Wei, C.-Y. Lai, T.-Y. Lin, J. Chen, S. Chi, "Metro add-drop network applications of cascaded dispersion-compensated interleaver pairs using a recirculating loop," *IEEE Photon. Technol. Lett.*, vol. 17, pp. 1349-1351, June 2005.

Bibliography

[1] I. P. Kaminow, *Optical fiber telecommunications IV* (Academic Press, 2002), Chap. 1.

[2] T. L. Friedman, *The world is flat* (Farrar Straus & Giroux, 2005).

[3] ACTS programme report, http://cordis.europa.eu/acts/home.html

[4] K. Vlachos, N. Pleros, C. Bintjas, G. Theophilopoulos, and H. Avramopoulos, "Ultrafast time-domain technology and its application in all-optical signal processing," *J. Lightwave Technol.*, vol. 21, pp. 1857-1868, Sept. 2003.

[5] K. E. Stubkjaer, "Semiconductor optical amplifier-based all-optical gates for high-speed optical processing," *IEEE J. Sel. Topics Quantum Electron.*, vol. 6, pp. 1428-1435, Nov.-Dec. 2000.

[6] B.-E. Olsson and D. J. Blumenthal, "All-optical demultiplexing using fiber cross-phase modulation (XPM) and optical filtering," *IEEE Photon. Technol. Lett.*, vol. 13, pp. 875-877, Aug. 2001.

[7] R. Salem, A. S. Lenihan, G. M. Carter, and T. E. Murphy, "Techniques for polarization-independent cross-phase modulation in nonlinear birefringent fibers," *IEEE J. Sel. Topics Quantum Electron.*, vol. 14, pp. 540-550, May/June 2008.

[8] T. Durhuus, B. Mikkelsen, C. Joergensen, S. L. Danielsen, and K. E. Stubkjaer, "All-optical wavelength conversion by semiconductor optical amplifiers", *J. Lightwave Technol.*, vol. 14, pp. 942-954, June 1996.

[9] Y. Liu, M. T. Hill, E. Tangdiongga, H. de Waardt, N. Galabretta, G. D. Khoe, and H. J. S. Dorren, "Wavelength conversion using nonlinear polarization rotation in a single semiconductor optical amplifier", *IEEE Photon. Technol. Lett.*, vol. 15, pp. 90-92, Jan. 2003.

[10] M. Zhao, J. D. Merlier, G. Morthier, and R. Baets, "All-optical 2R regeneration based on polarization rotation in a linear optical amplifier," *IEEE Photon. Technol. Lett.*, vol. 15, pp. 305-307, Feb. 2003.

[11] S. Diez, C. Schmidt, R. Ludwig, H. G. Weber, K. Obermann, S. Kindt, I. Koltchanov, and K. Petermann, "Four-wave mixing in semiconductor optical amplifiers for frequency conversion and fast optical switching", *IEEE J. Sel. Topics Quantum Electron.*, vol. 3, pp. 1131-1145, Oct. 1997.

[12] K. Mishina, A. Maruta, S. Mitani, T. Miyahara, K. Ishida, K. Shimizu, T. Hatta, K. Motoshima, and K.-i. Kitayama, "NRZ-OOK-to-RZ-BPSK modulation-format

conversion using SOA-MZI wavelength converter," *J. Lightwave Technol.*, vol. 24, pp. 3751-3758, Oct. 2006.

[13] W. Astar and G. M. Carter, "10 Gbit/s RZ-OOK to RZ-BPSK format conversion using SOA and synchronous pulse carver," *Electronics Lett.*, vol. 44, pp. 369-370, Feb. 2008.

[14] K. Mishina, S. Kitagawa, and A. Maruta, "All-optical modulation format conversion from on-off-keying to multiple-level phase-shift-keying based on nonlinearity in optical fiber," *Opt. Express*, vol. 15, pp. 8444-8453, June 2007.

[15] G. P. V. Mamyshev, "All-optical data regeneration based on self-phase modulation effect," *Proc. ECOC*, 1998, pp. 475-476.

[16] E. Ciaramella and S. Trillo, "All-optical signal reshaping via four-wave mixing in optical fibers," *IEEE Photon. Technol. Lett.*, vol. 12, pp. 849-851, July 2000.

[17] G. Raybon, Y. Su, J. Leuthold, R.-J. Essiambre, T. Her, C. Joergenson, P. Steinvurzel, and K. D. K. Feder, "40 Gb/s pseudo-linear transmission over one million kilometers," *Proc. OFC and Exhibit*, 2002, pp. FD10-1 - FD10-3.

[18] K. Croussore, I. Kim, C. Kim, Y. Han, and G. Li, "Phase-and-amplitude regeneration of differential phase-shift keyed signals using a phase-sensitive amplifier," *Opt. Express*, vol. 14, pp. 2085-2094, Mar. 2006.

[19] A. G. Striegler, M. Meissner, K. Cvecek, K. Sponsel, G. Leuchs, and B. Schmauss, "NOLM-based RZ-DPSK signal regeneration," *IEEE Photonics Technol. Lett.*, vol. 17, pp. 639-641, Mar. 2005.

[20] M. Matsumoto, "Performance improvement of phase-shift-keying signal transmission by means of optical limiters using four-wave mixing in fibers," *J. Lightwave Technol.*, vol. 23, pp. 2696-2701, Sep. 2005.

[21] C. A. Brackett, A. S. Acampora, J. Sweitzer, G. Tangonan, M. T. Smith, W. Lennon, K.-C. Wang, and R. H. Hobbs, "A scalable multiwavelength multihop optical network: a proposal for research on all-optical networks," *J. Lightwave Technol.*, vol. 11, pp. 736-753, May/June 1993.

[22] M. Koga, Y. Hamazumi, A. Watanabe, S. Okamoto, H. Obara, K.-I. Sato, M. Okuno, and S. Suzuki, " Design and performance of an optical path cross-connect system based on wavelength path concept," *J. Lightwave Technol.*, vol. 14, pp. 1106-1119, June 1996.

[23] P. J. Winzer and R.-J. Essiambre, "Advanced modulation formats for high-capacity optical transport networks," *J. Lightwave Technol.*, vol. 24, pp. 4711-4728, Dec. 2006.

[24] W. Astar, A. S. Lenihan, and G. M. Carter, "Performance of DBPSK in a 5 10 Gb/s mixed modulation format Raman/EDFA WDM system," *IEEE Photon. Technol. Lett.*, vol. 17, pp. 2766-2768, Dec. 2005.

[25] P. Ohlen and E. Berglind, "BER caused by jitter and amplitude noise in limiting optoelectronic repeaters with excess bandwidth," *IEE Proc.-Optoelectron.*, vol. 145, pp. 147-150, June 1998.

[26] B. Mikkelsen, K. S. Jepsen, M. Vaa, H. N. Poulsen, K. E. Stubkjaer, R. Hess, M. Duelk, W. Vogt, E. Gamper, E. Gini, P. A. Besse, H. Melchior, S. Bouchoule, and F. Devaux, "All-optical wavelength converter scheme for high speed RZ signal formats", *Electron. Lett.*, vol. 33, pp. 2137-2139, Oct. 1997.

[27] S. Nakamura, Y. Ueno, and K. Tajima, "168-Gb/s all-optical wavelength conversion with a Symmetric-Mach-Zehnder-type switch," *IEEE Photon. Technol. Lett.*, vol. 13, pp. 1091-1093, Oct. 2001.

[28] S. Nakamura, and K. Tajima, "Bit-rate-transparent non-return-to-zero all-optical wavelength conversion at up to 42 Gb/s by operating Symmetric-Mach-Zehnder switch with new scheme," *OFC'04*, paper FD3.

[29] A. Gnauck, "40-Gb/s RZ-differential phase shift keyed transmission," *OFC'03*, paper ThE1.

[30] A. S. Lenihan and G. M. Carter, "Polarization-insensitive wavelength conversion at 40 Gb/s using birefringent nonlinear fiber," *CLEO'07* , paper CThAA2.

[31] J. K. Rhee, D. Chowdhury, K. S. Cheng, and U. Gliese, "DPSK 3210 Gb/s transmission modeling on 590 km terrestrial system," *IEEE Photonics Technol. Lett.*, vol. 12, pp. 1627-1629, Dec. 2000.

[32] A. H. Gnauck, X. Liu, X. Wei, D. M. Gill, and E. C. Burrows, "Comparison of modulation formats for 42.7-Gb/s single-channel transmission through 1980 km of SSMF," *IEEE Photonics Technol. Lett.*, vol. 16, pp. 909-911, Mar. 2004.

[33] J. P. Gordon and L. F. Mollenauer, "Phase noise in photonic communication systems using linear amplifiers," *Opt. Lett.*, vol. 15, pp. 1351-1353, Dec. 1990.

[34] C. J. McKinstrie, C. Xie, and C. Xu, "Effects of cross-phase modulation on phase jitter in soliton systems with constant dispersion," *Opt. Lett.*, vol. 28, pp. 604-606, Apr. 2003.

[35] V. S. Grigoryan, M. Shin, P. Devgan, J. Lasri, and P. Kumar, "SOA-based regenerative amplification of phase-noise-degraded DPSK signals: dynamic analysis and demonstration," *J. Lightwave Technol.*, vol. 24, pp. 135-142, Jan. 2006.

[36] E. S. Awad, P. S. Cho, and J. Goldhar, "All-optical phase and amplitude regeneration of return-to-zero differential phase shift keying data," *OFC'07*, paper JThA53.

[37] P. Johannisson, G. Adolfsson, and M. Karlsson, "Suppression of phase error in differential phase-shift keying data by amplitude regeneration," *Opt. Lett.*, vol. 31, pp. 1385-1387, May 2006.

[38] G. P. Agrawal, and N. A. Olsson, "Self-phase modulation and spectral broadening of optical pulses in semiconductor laser amplifiers," *IEEE J. Quantum Electron.*, vol. 25, pp. 2297-2306, Nov. 1989.

[39] H. J. S. Dorren, D. Lenstra, Y. Liu, M. T. Hill, and G.-D. Khoe, "Nonlinear polarization rotation in semiconductor optical amplifiers: theory and application to all-optical flip-flop memories," *IEEE J. Quantum Electron.*, vol. 39, pp. 141-148, Jan. 2003.

[40] M. G. Davis and R. F. O'Dowd, "A transfer matrix method based large-signal dynamic model for multi-electrode DFB lasers," *IEEE J. Quantum Electron.*, vol. 30, pp. 2458-2466, Nov. 1994.

[41] H. Lee, H. Yoon, Y. Kim, and J. Jeong, "Theoretical study of frequency chirping and extinction ratio of wavelength-converted optical signals by XGM and XPM using SOA's," *IEEE J. Quantum Electron.*, vol. 35, pp. 1213-1219, Aug. 1999.

[42] D. Marcenac and A. Mecozzi, "Switches and frequency converters based on cross-gain modulation in semiconductor optical amplifiers," *IEEE Photonics Tech. Lett.*, vol. 9, pp. 749-751, June 1997.

[43] G. Lenz, B. J. Eggleton, C. R. Giles, C. K. Madsen, and R. E. Slusher, "Dispersive properties of optical filters for WDM systems," *IEEE J. Quantum Electron.*, vol. 34, pp. 1390-1402, Aug. 1998.

[44] D. Goldring, Z. Zalevsky, and D. Mendelovic, "Enlargement of the information capacity in optical fibre channels using polarization coding," *J. Opt. A: Pure Appl. Opt.*, vol. 6, pp. 52-58, Mar. 2004.

[45] G. P. Agrawal, *Nonlinear Fiber Optics* (Academic Press, San Diego, CA, 2001), Chap. 7.

[46] W. Astar, A. S. Lenihan, and G. M. Carter, "Theoretical analysis of polarisation-insensitive wavelength conversion by four-wave mixing in photonic crystal fibre," *Electronics Lett.*, vol. 43, pp. 1419-1421, Dec. 2007.

[47] A. H. Gnauck and P. J. Winzer, "Optical phase-shift-keyed transmission," *J. Lightwave Technol.*, vol. 23, pp. 115-130, Jan. 2005.

[48] K.-P. Ho, *Phase-Modulated Optical Communication System* (Springer, 2005), Chap. 3.

[49] J. G. Proakis, *Digital Communications* (McGraw Hill, New York, 2000), Chap. 5.

[50] P. C. Jain, "Error probabilities in binary angle modulation," *IEEE Trans. Inf. Theory*, vol. 20, pp. 36-42, Jan. 1974.

[51] C. J. MaKinstrie, S. Radic, and C. Xie, "Reduction of soliton phase jitter by in-line phase conjugation," *Opt. Lett.*, vol. 28, pp. 1519-1521, Sep. 2003

[52] S. L. Jansen, D. van den Borne, G. D. Khoe, H. de Waardt, C. C. Monsalve, S. Spalter and P. M. Krummrich, "Reduction of nonlinear phase noise by mid-link spectral inversion in a DPSK based transmission system," *OFC'05*, paper OTh05.

[53] X. Liu, X. Wei, R. E. Slusher, and C. J. McKinstrie, "Improving transmission performance in differential phase-shift-keyed systems by use of lumped nonlinear phase-shift compensation," *Opt. Lett.*, vol. 27, pp. 1616-1618, Sep. 2002.

[54] C. Xu and X. Liu, "Post-nonlinearity compensation with data-driven phase modulators in phase-shift keying transmission," *Opt. Lett.*, vol. 27, pp. 1619-1621, Sep. 2002.

[55] S. A. Derevyanko and S. K. Turitsyn, "Reduction of the phase jitter in differential phase-shift-keying soliton transmission systems by in-line Butterworth filters," *Opt. Lett.*, vol. 29, pp. 35-37, Jan. 2004.

[56] D. Boivin, M. Hanna, P.-A. Lacourt, and J.-P. Goedgebuer, "Reduction of phase jitter in dispersion-managed systems by in-line filtering," *Opt. Lett.* , vol. 29, pp. 688-690, Apr. 2004.

[57] I. Kang, C. Dorrer, L. Zhang, M. Rasras, L. Buhl, A. Bhardwaj, S. Cabot, M. Dinu, X. Liu, M. Cappuzzo, L. Gomez, A. Wong-Foy, Y. F. Chen, S. Patel, D. T. Neilson, J. Jaques, and C. R. Giles, "Regenerative all optical wavelength conversion of 40-Gb/s DPSK signals using a semiconductor optical amplifier Mach-Zehnder interferometer," *ECOC'05*, paper Th 4.3.3.

[58] M. Matsumoto and H. Sakaguchi, "DPSK signal regeneration using a fiber-based amplitude regenerator," *Opt. Express*, vol. 15, pp. 11169-11175, July 2008.

[59] F. Zhang, C.-A. Bunge, and K. Petermann, "Analysis of nonlinear phase noise in single-channel return-to-zero differential phase-shift keying transmission systems," *Opt. Lett.*, vol. 31, pp. 1038-1040, Apr. 2006.

[60] X. Liu, C. Xu, and X. Wei, "Nonlinear phase noise in pulse-overlapped transmission based on return-to-zero differential-phase-shift-keying," *ECOC'02*, paper 9.6.5.

[61] X. Wei and X. Liu, "Analysis of intrachannel four-wave mixing in differential phase-shift keying transmission with large dispersion," *Opt. Lett.*, vol. 28, pp. 2300-2302, Dec. 2003.

[62] K.-P. Ho, "Error probability of DPSK signals with intrachannel four-wave mixing in highly dispersive transmission systems," *IEEE Photon. Technol. Lett.*, vol. 17, pp. 789-791, Apr. 2005.

[63] M. Matsumoto, "Regeneration of RZ-DPSK signals by fiber-based all-optical regenerators," *IEEE Photon. Technol. Lett.*, vol. 17, pp. 1055-1057, May 2005.

[64] P. S. Cho, G. Harston, C. J. Kerr, A. S. Grennblatt, A. Kaplan, Y. Achiam, G. Levy-Yurista, M. Margalit, Y. Gross, and J. B. Khurgin, "Investigation of 2-b/s/Hz 40-Gb/s DWDM transmission over 4100 km SMF-28 fiber using RZ-DQPSK and polarization multimplexing," *IEEE Photon. Technol. Lett.*, vol. 16, pp. 656-658, Feb. 2004.

[65] M. Galili, B. Huettl, C. Schmidt-Langhorst, A. Gual i Coca, R. Ludwig, and C. Schubert, " 320 Gbit/s DQPSK all-optical wavelength conversion using four-wave mixing," *OFC'07*, paper OTuI3.

[66] G.-W. Lu, K. S. Abedin, and T. Miyazaki, "All-optical RZ-DPSK WDM to RZ-DQPSK phase multiplexing using four-wave mixing in highly nonlinear fiber," *IEEE Photon. Technol. Lett.*, vol. 19, pp. 1699-1701, Nov. 2007.

[67] X. Huang, L. Zhang, M. Zhang, and P. Ye, "Impact of nonlinear phase noise on direct-detection DQPSK WDM systems," *IEEE Photon. Technol. Lett.*, vol. 17, pp. 1423-1425, July 2005.